Title of Thesis

Mixture Formation Measurement of Transient Hydrogen Jet in Constant-Volume Vessel Using Spark Induced Breakdown Spectroscopy (SIBS)

March 2015

Md Tasyrif bin Abdul Rahman

Graduate School of
Natural Science and Technology
(Doctor's Course)

OKAYAMA
UNIVERSITY

OKAYAMA UNIVERSITY

OKAYAMA UNIVERSITY, JAPAN

Mixture Formation Measurement of Transient Hydrogen Jet in Constant-Volume Vessel Using Spark Induced Breakdown Spectroscopy (SIBS)

by

Md Tasyrif bin Abdul Rahman

A dissertation submitted to the Graduate School of Natural Science and Technology in partial fulfillment of the requirements for the degree of

DOCTOR OF ENGINEERING

Major: Mechanical Engineering

Under the supervision of

Professor Dr. Eiji Tomita

Co-supervised by

Professor Dr. Shinichiro Yanase

Professor Dr. Akihiko Horibe

Graduate School of Natural Science and Technology

Okayama University, Japan

To whom it may concern:

This is to certify that the work entitled "Mixture Formation Measurement of Transient Hydrogen Jet in Constant-Volume Vessel Using Spark Induced Breakdown Spectroscopy (SIBS)" is carried out by Md Tasyrif bin Abdul Rahman in the Division of Industrial Innovation Sciences at Okayama University under my supervision.

Signature & seal of Supervisor

Professor Dr. Eiji Tomita

Division of Industrial Innovation Sciences,

Graduate School of Natural Science and Technology,

Okayama University

JAPAN

Official Seal

Professor Dr. Toshiro Noritsugu

Dean of Graduate School of Natural Science

and Technology,

Okayama University

JAPAN.

ABSTRACT

Currently, the transport sector is largely dependent on fossil fuels, which leads to global problem such as emission of pollutants, greenhouse effect, ozone layer depletion etc. The carbon dioxide that is released to the earth's atmosphere will still be there in hundred years' time. The answer to these problems is to replace and improve current technologies with alternative fuels that have comparable or better performance and will not emit the carbon dioxide. Many researchers and engineers agree that one of the solutions to these global problems is to replace the existing fossil fuel system with the clean hydrogen energy system. It is being explored as a fuel for passenger vehicles. Hydrogen was well known as very efficient and clean fuel. Hydrogen can be used in fuel cells or burned in internal combustion engine (ICEs). The use of hydrogen in combustion will produce no greenhouse gases, no ozone layer depleting chemicals, and reduce the environment pollution, but several significant challenges must be overcome before it can be widely used.

Hydrogen is being studied and promoted by many researchers as one of the fuels of the future. Hydrogen is a potentially emissions-free alternative fuel that can be produced from diverse domestic energy sources. It has been investigated as a fuel for internal combustion engines because of its potential for high engine efficiency and greenhouse gas reduction, and shows promise as an alternative fuel for direct-injection spark-ignition (DISI) engines. One of the main advantages of using hydrogen as a fuel in a DISI engine is its wide flammability range, which can provide smooth engine operation with a very lean mixture and low NO_X emissions. Moreover, it can be injected directly into the spark plug because of its high volumetric efficiency and potential for avoiding pre-ignition and backfiring. However, the use of hydrogen in a direct-injection environment presents challenges under high engine loads, including knock, pre-ignition, and backfire. These issues prevent reliable operation and limit the maximum output of engine power. To cope with hydrogen engine problems of this kind, some researchers have studied the internal mixing of hydrogen. Optimization of the spark timing and pressure is an important aspect of the development of hydrogen DISI engines, and can suppress backfiring and knocking, especially at higher engine loads. To overcome this problem, a better understanding of the spark discharge and spark ignition during transient hydrogen jet is necessary. Therefore, it is very important to study an effect of local equivalence ratio and behavior of spark discharge in SI engine.

In this work, spark-induced breakdown spectroscopy (SIBS) was employed to investigate the mixing process of a hydrogen jet in a constant-volume vessel. Effect of ambient pressure on fuel concentration measurement of direct-injection hydrogen jet SIBS in a constant-volume vessel was investigated. The tests were conducted with hydrogen injection in different ambient pressure of nitrogen, and the local fuel concentration of the hydrogen jet was measured at several locations, using a SIBS sensor. A high-speed camera was used to visualize spark discharge fluctuations, and hydrogen jet concentration measurements were conducted simultaneously. The image of hydrogen jet development at the nozzle exit in a constant-volume vessel was taken by high speed camera to study the effects of fuel injection pressure and ambient density on the overall jet characteristic at nozzle tip. The direct visualization of hydrogen jet gives the useful information where the jet tip pushes out the quiescent nitrogen, and then the vortex structure is formed by the interaction between the jet and the ambient nitrogen. Hydrogen jet injection at different ambient pressure may affect the momentum injected into the cylinder, the mixture of turbulence, and the amount of fuel-air mixture. This method was used to select the appropriate measurement points of hydrogen concentration based on the probability of where the spectrum could be obtained with SIBS.

Spectrally resolved atomic emissions from the plasma generated by the spark plug were examined to determine the local equivalence ratio. The light emissions of wavelength for nitrogen (501nm) and hydrogen (656nm) from spark discharge were observed with SIBS sensor. Spectrally resolved emission of plasma was detected simultaneously by spectrometer. The possibility of determining the hydrogen/nitrogen ratio in the spark gap with spectroscopy was investigated. When determine the emission intensity ratio between two elements and pure emission of a particular element, it is necessary to find the exact peak intensity for each element. When calculating the element concentrations in integrated peak intensities, the background processing method is very important to ensure accurate quantification of emission spectrum measurements. In this research, the original signal was smoothed using a moving average filter and the background were then subtracted using the background subtraction method. Comparison of the intensity peaks of atomic emissions from hydrogen and nitrogen allows the local hydrogen concentration in a measured volume to be determined, and hence also the local equivalence ratio. Spectrum calibration using hydrogen/nitrogen mixture and experiment using hydrogen injection were executed under the ambient pressure conditions from 0.5 to 1.5 MPa. The results showed increasing trends in background as well as intensity peaks of hydrogen and nitrogen when the ambient pressure increased. The increased ambient

nitrogen density inside the chamber influenced the spatial structure of the hydrogen jet and slowed down the spray penetration and then the local equivalence ratio at spark location was changed. However, hydrogen jet during the injection period generally followed the similar way of quasi-steady state then after-injection unsteady state occurred after the injection finished in all set ambient conditions.

Acknowledgment

Contents

List of figures

IX

List of tables

1　Introduction

1.1　Research background

Hydrogen is being studied and promoted by many researchers as one of the fuels of the future [1–3]. It has been investigated as a fuel for internal combustion engines (ICEs) because of its potential for high engine efficiency and greenhouse gas reduction [4–7], and shows promise as an alternative fuel for direct-injection spark-ignition (DISI) engines. One of the main advantages of using hydrogen as a fuel in a DISI engine is its wide flammability range, which can provide smooth engine operation with a very lean mixture and low NO_X emissions [8]. Moreover, it can be injected directly into the spark plug because of its high volumetric efficiency and potential for avoiding pre-ignition and backfiring [9,10]. However, the use of hydrogen in a direct-injection environment presents challenges under high engine loads, including knock, pre-ignition, and backfire [11]. These issues prevent reliable operation and limit the maximum output of engine power. To cope with hydrogen engine problems of this kind, some researchers have studied the internal mixing of hydrogen [12].

Ordinarily, internal mixing of hydrogen is achieved by feeding the hydrogen at high pressure. This technique can eliminate many combustion abnormalities and is very effective for avoiding backfire and knock, especially under high engine loads. Researchers at Argonne National Laboratory have intensively focused on applying advanced direct-injection and mixture-formation techniques in single-cylinder engines [13,14]. In particular, they have developed an injector that successfully performs late injection and delivers higher mass-flow rates during injection, which can extend the operating range to higher engine loads and speeds to achieve maximum efficiency. Koyanagi et al. [15] demonstrated that using higher injection pressures in a hydrogen DISI engine results in more stringent conditions for spark placement. They observed that hydrogen diffusion in the radial direction was diminished near the spark gap point as the injection pressure increased, resulting in hydrogen concentrations that approached the upper flammability limit more rapidly. More jet penetration was also observed as the injection pressure increased. Takagi et al. [16] proposed the plume ignition combustion concept (PCC) for hydrogen DISI engines. This concept, in which a rich mixture plume is ignited in the midst of or just after hydrogen injection, enables NOx emissions to be reduced under high engine loads. Roy et al. [17] studied jet structure in addition to other physical processes resulting from hydrogen gas injection. They observed that the jet penetration rate

increased with increasing injection pressure, and decreased with increasing ambient pressure. They also observed that the combustion characteristics of hydrogen jets can be controlled by varying the fuel-injection timing. Fuel-injection timing relative to ignition timing is an important parameter for controlling the combustion characteristics in direct-injection hydrogen combustion. In summary, the mixing characteristics of DI hydrogen engines have attracted considerable research interest, especially in regard to the local fuel concentration or fuel/air ratio.

Quantitative measurements of cycle-to-cycle variations in the fuel/air mixture near the point of ignition are relatively rare for real-world hydrogen DISI engines. A variety of techniques have previously been used to measure the local fuel concentration or fuel/air ratio in SI engines, including infrared (IR) absorption [18–20], planar laser-induced fluorescence (PLIF)[21–23], Raman scattering [24,25], and laser-induced breakdown spectroscopy (LIBS) [26–29]. However, these techniques involve some drawbacks. It is difficult to measure the hydrogen fuel/air ratio via IR absorption, because absorption bands are lacking at visible and infrared wavelengths. Application of PLIF and LIBS techniques is not practical, because major engine changes are required. Spark-induced breakdown spectroscopy (SIBS) is a suitable technique that can directly measure the fuel concentration inside a combustion chamber using a conventional spark plug. The electrical spark can be generated between two electrodes that ablate a sample material, which is vaporized, atomized, and excited. The emission characteristics can be determined from the elemental composition of the sample. This technique has been applied not only to fuel concentration measurement, but also to the measurement of metals in aerosols and soils. Since 1993, SIBS has been under development as a monitoring technique for metals in airborne particulate materials. Hunter at al. [30] applied an SIBS technique to soil analysis involving the detection of Pb, Cr, Ba, Hg, and Cd. For each metal surveyed, the detection limits were sufficient to identify which samples require no treatment prior to disposal, and which should be subjected to verification in the laboratory. SIBS has been applied to the monitoring of airborne heavy metals, and enables lead and chromium to be detected at both low and high concentrations [31]. LIBS and SIBS procedures for detecting mercury in soils have been compared to determine the detection ranges of both techniques [32]. The results demonstrate that SIBS is more suitable for measuring lower concentrations. In this context, the interest has been in developing SIBS techniques as low-cost alternatives to LIBS for the analysis of heavy metals in soils. Fansler et al. [33] conducted measurements of local fuel concentration in internal combustion engines,

2

using spark-emission spectroscopy. The results demonstrate that for stratified operation with fixed fuel-injection timing, a spark timing later than optimum leads to incomplete combustion in many cycles, due to fuel/air ratios that are too lean for good ignition and rapid flame development. In previous research, we examined the spectrally resolved emission spectra of plasma generated by a spark plug, using the SIBS technique to clarify its potential for measuring the local fuel concentration in a premixed mixture [34]. We developed a spark-plug sensor using a 200-µm UV-grade quartz fiber, which proved practically applicable for investigating a laminar premixed flame in a CH4/air mixture. We further improved this sensor by increasing the core diameter of the UV-grade quartz fiber to 600 µm to enhance its light-collecting capability. This modified spark-plug sensor was used to measure the local fuel–air concentration in the spark gap at the time of ignition under stratified-charge conditions [35]. The results indicate that the SIBS technique allows the local fuel distribution around a spark plug to be measured. The SIBS sensor can directly measure the equivalence ratio of the mixture near the spark plug at the time of spark discharge. However, the capability of the spark-plug sensor should be enhanced to improve the accuracy of the data it provides. We made further improvements by increasing the spark-plug gap to 1.5 mm, which increases the stability of spark-discharge initiation [36,37]. An optical UV-grade quartz fiber with a core diameter of 1000 µm (fiber diameter 1250 µm) was used to further increase the light-collecting capability. The influence of the hydrogen-injection conditions on the mixture distribution in a constant-volume vessel was determined by measuring the instantaneous local equivalence ratio, using the SIBS technique.

1.2 Objectives

The objective of this study is to determine the influence of hydrogen injection conditions on the mixture distribution in a constant volume chamber by measuring the instantaneous local equivalence ratio using the spark-induced breakdown spectroscopy (SIBS) technique. In the present work, we measured the hydrogen concentration at different locations to investigate the mixing process of a direct-injection hydrogen jet in a constant-volume vessel. The measurement of the local equivalence ratio was carried out in a hydrogen jet injection with specific injection period transferred to the constant volume chamber. Mixture formation and the setting of the equivalence ratio were carried out by injecting hydrogen into pure nitrogen without combustion. The atomic emission intensity during the breakdown and arc phases of spark discharge was obtained using the fiber-optic spark-plug sensor.

Spark discharge fluctuations were visualized using a high-speed camera, and hydrogen jet concentration measurements were conducted simultaneously. Direct visualization of the spark discharge provided useful information about the influence of spark discharge characteristics relative to the spark timing. The spark discharge visualization revealed that arc discharge occurs between the central and ground electrodes, whereas most of the glow discharge occurs outside the spark plug gap. It also revealed that most of the accumulated spectrum appears during arc discharge. Additionally, the spark gap plays an important role in terms of the ability to collect emission spectra between the central and ground electrodes.

Spectrally resolved emission spectra of plasma generated by the spark plug sensor were detected simultaneously by spectrometer. In this study the ratio of hydrogen-nitrogen concentration is determined from the spectral peak ratio of IH/IN. Instantaneous local equivalence ratios were obtained from the atomic emission intensity ratios of nitrogen at 501 nm and hydrogen at 656 nm. The local equivalence ratio of hydrogen/nitrogen mixture was carried out using spark-induced breakdown spectroscopy. The emission intensity of Hydrogen and nitrogen spectrum under several equivalence ratio conditions was measured. The correlation between the hydrogen/nitrogen ratio and atomic emission was determined, and the post-processing procedure was calibrated. The equivalence ratio of the hydrogen/nitrogen mixture was varied from 0.3 to 5.0. A systematic increase in the slope (the sensitivity) of the curves was observed with increasing ambient pressure. As the equivalence ratio increased, the emission intensity of H and N was increased. Comparing the intensity peaks of atomic emissions from hydrogen and nitrogen gives local hydrogen concentration in the measured volume.

The measurements of equivalence ratio of hydrogen jet injection were studied mainly using four injection timing modes. The Experimental was conducted with different ambient pressure at 0.5 MPa, 1.0 MPa and 1.5 MPa to investigate the influence of the ambient pressure. Measurements were taken at different locations in a direct-injection hydrogen jet to investigate the mixing process. The spatial structure of the hydrogen jet and its arrival time in the spark plug gap both affect the hydrogen/nitrogen mixing when the spark is discharged. The ratio of hydrogen/nitrogen concentration was able to be determined from the spectral peak ratio of H_α/N(I) at atomic emission from nitrogen at 501nm and hydrogen at 656nm.The measurement results demonstrate the local variation in the equivalence ratio throughout the jet and along its axis. The spectra results showed an increasing trend in background as well as

intensity peak when the ambient pressure increased. As the ambient pressure increased, the ambient nitrogen densities inside the chamber increased thus it influenced the spatial structure of the hydrogen jet and slowed down the spray penetration. This resulted the local variation of equivalence ratio throughout the jet and along its axis.

The results show the hydrogen concentration near the spark plug was constant although the global equivalence ratio and ignition modes are difference. The result presented here shows that SIBS method has a potential for measurements of hydrogen concentration in constant volume chamber.

1.3 Thesis outline

This thesis is divided into 6 chapters.

Chapter 1 describes a previous work and gives motivation for the work performed in this thesis. The background discuss about the current fossil fuels, which leads to global problem such as emission of pollutants, greenhouse effect, ozone layer depletion etc. The answer to these problems is to replace and improve the current technologies with hydrogen fuels that have good performance and will not emit the carbon dioxide. However, the use of hydrogen in a direct-injection environment presents challenges and must be overcome before it can be widely used. The objective of this study is to determine the influence of hydrogen injection conditions on the mixture distribution in a constant-volume vessel by measuring the instantaneous local equivalence ratio using the spark-induced breakdown spectroscopy (SIBS) technique.

Chapter 2 discussed about the hydrogen properties and the benefit when it use in combustion. The techniques to measure equivalence ratio was describe as many technique such as Linear Raman scattering, Ion current, Laser-Induced fluorescent (LIF), Planar laser induced fluorescent (PLIF), Laser-induced breakdown spectroscopy and Spark-induced breakdown spectroscopy (SIBS). The techniques proposed by other researchers require changing in the engine combustion chamber design for optical access from outside and difficult to be applied to concentration measurements for practical SI engines. The main purpose of this study is to measure the fuel concentration near the spark plug. Therefore, the use of SIBS technique (developed SIBS sensor) for measuring the hydrogen jet concentration

was proposed as a suitable technique that can directly measure the fuel concentration inside of the engine cylinder with only changing the spark plug.

Chapter 3 discussed about the apparatus and the methodology used in this study to measure the local fuel concentration of the hydrogen jet at different ambient pressures of nitrogen. A constant-volume vessel equipped with a SIBS sensor was used, and a swirl-type direct-injection (DI) injector with a single orifice was installed at the top of the vessel. The local fuel concentration of the hydrogen jet was measured at several locations, using a SIBS sensor. The SIBS sensor, which was developed using a commercially available spark plug with an optical fiber installed at the centre. A spectrometer was used to analyse the light obtained from the optical fiber. A high-speed camera was used to visualize spark discharge fluctuations, and hydrogen jet concentration measurements were conducted simultaneously. Four types of filters are discussed: 1) moving average, 2) binomial, 3) Gaussian, and 4) windowed (Hamming method). The quantity test experiment was discussed whereas the results of injection amount versus hydrogen injection duration, the relation between equivalence ratio and hydrogen injection duration can be calculated

Chapter 4 describes about the calibration technique with the spark-induced breakdown spectroscopy (SIBS) sensor to obtain optimum results. The correlation between the hydrogen/nitrogen mixing ratio and atomic emission, and the post-processing procedure was discussed. Spectral calibration was carried out with a hydrogen/nitrogen mixture at pressures of 0.5, 1.0 and 1.5 MPa and at room temperature. The spectra were determined for a range of the equivalence ratios from 0.3 to 5.0. Two clear emission peaks were observed in the wavelength range 450–700 nm; the peak at 656 nm corresponds to H_α while that at 501 nm to N(I). The intensity of the H_α peak increases as a function of the ambient pressure ,P_{amb}. Various methods of data smoothing and filtering were discussed in order to remove noise from a contaminated signal to help reveal important signal features and components. Moving average filters with two different numbers of points were applied to the emission spectral data. The atomic spectral lines were integrated and the background area was subtracted using the method originally reported by Shirley and later improved by Proctor and Sherwood to eliminate the effects of elastic scattering. The results show an increase in the background radiation, as well as of the peaks corresponding to hydrogen and nitrogen atomic emission lines, as the ambient pressure increased. An empirical formula for deriving the equivalence ratio for ambient pressure using the SIBS sensor was obtained.

Chapter 5 focuses on the hydrogen jet concentration measurement. The characteristic of the spark images was discussed. The injection of hydrogen with different ambient pressures visualized with a high-speed video camera was conducted to study the distribution pattern of hydrogen jet and to select the appropriate measurement points for the hydrogen concentration for optimal locations to carry out SIBS measurements. A high-speed camera was used to visualize spark discharge fluctuations. Direct visualization of the spark discharge provided useful information about the influence of spark discharge characteristics related to the spark timing. The images show that the spark discharge began as an arc discharge, followed by glow discharge. Arc and glow discharge must always be preceded by a breakdown phase. The spark-plug sensor was capable of collecting the emission spectra between the central and ground electrodes. Local equivalence ratios for different spark timings were discussed and based on the results, the mixing process can be classified into three states, (i) initial unsteady state (HI at P_{amb}=1.0 and 1.5 MPa), (ii) quasi-steady state (HI at P_{amb}=0.5 MPa, CI and TI at P_{amb}= 0.5, 1.0, 1.5 MPa) and (iii) after-injection unsteady state (ATI in all conditions).

Chapter 6 describes the conclusion arrived in this research work.

2 Hydrogen for fuel and application

2.1 Hydrogen fuel

Hydrogen has unique fuel properties relative to typical gasoline and other popular fuels. A hydrogen fuel could be an infinite supply potential. It can be generated from non-fossil energy source and upon combustion it produces water which is goes back to the earth. From an environmental point of view, it is consider as clean fuel. As far as engine operation is concerned, a hydrogen fuelled engine will not emit any unburnt hydrocarbons, CO, sulfur dioxide, smokes etc.

2.1.1 General properties of hydrogen as fuel

While judging the suitability of hydrogen as an engine fuel, it is very important to compare its various physical and chemical properties with other conventional engine fuels. Table 2-1 and Table 2-2 shows the chemical and combustion properties of various fuel compared with hydrogen [1,38,39].

Table 2-1 Physical and chemical properties of various fuels

Properties	Gasoline	Hydrogen	Ammonia	Methanol	Ethanol
Molecular Weight	91.4	2.02	17.03	32.04	46.07
Heat of combustion (net) MJ kg^{-1}	43.4	120.1	18.6	20.1	26.9
Stoichiometric mixture Mas air/Mass fuel	14.5	34.3	6.1	65	9.0
Maximum laminar flame speed ms^{-1}	0.37	2.91	0.010	0.52	-
Adiabatic flame temp., °C	2637	2756	2484	2576	2594
Octane number					
Research	91-100	130^{+}	130	110	106
Motor	82-94			87	89

Table 2-2 Combustion properties of hydrogen, methane and gasoline

Properties	Gasoline	Hydrogen	Ammonia
Limits of flammability in air, vol%	4.0-75.0	5.3-15.0	1.0-7.6
Stoichiometric composition in air, vol%	29.53	9.48	1.76
Minimum energy for ignition in air, mJ	0.02	0.29	0.24
Auto ignition temperature	858	813	501-744
Flame temperature in air, K	2318	2148	2470
Burning velocity in NTP air, cm s^{-1}	265-325	37-45	37-43
Quenching gap in NTP air, cm	0.064	0.203	0.2
Percentage of thermal energy radiated from flame to surrounding, %	17-25	23-33	30-42
Diffusivity in air, cm^2 s^{-1}	0.63	0.2	0.08
Normalized flame Emissivity 2000 K, 1 atm	1.00	1.7	1.7
Limits of flammability (equivalence ratio)	0.1-7.1	0.53-1.7	0.7-3.8

2.1.1.1 Limits of flammability

The limits of flammability are one of the most important properties of a fuel. The limits of flammability are measure of the range of fuel/air ratios over which an engine can operate. Hydrogen has a wide range of flammability (4-75% by volume– stoichiometric: 66% by volume) in comparison with other fuels. The advantages of this are that hydrogen can run on a lean mixture. Generally, fuel economy is improved and the combustion reaction is more complete when engine is run on slightly lean mixtures. However, too lean operation can significantly reduce the power output of an engine due to a reduction in the volumetric heating value of the fuel-air mixture. Hydrogen engine can be run on ultra-lean mixtures or mixture considerably leaner than those used in gasoline engines. In terms of equivalence ratio, hydrogen is theoretically can be operated at equivalence ratio of 0.1.

9

2.1.1.2   Minimum ignition energy

The minimum energy of hydrogen required for ignition is about an order of magnitude less than that required for gasoline. This enables hydrogen engines can run well on lean mixtures. Unfortunately, since very little energy is necessary to ignite hydrogen due to the wide limits of flammable of hydrogen, a problem such as premature ignition and flashback occurs easily. The minimum ignition energy as a function of equivalence ratio is shown in Figure 2-1 for hydrogen-air and methane-air mixture.
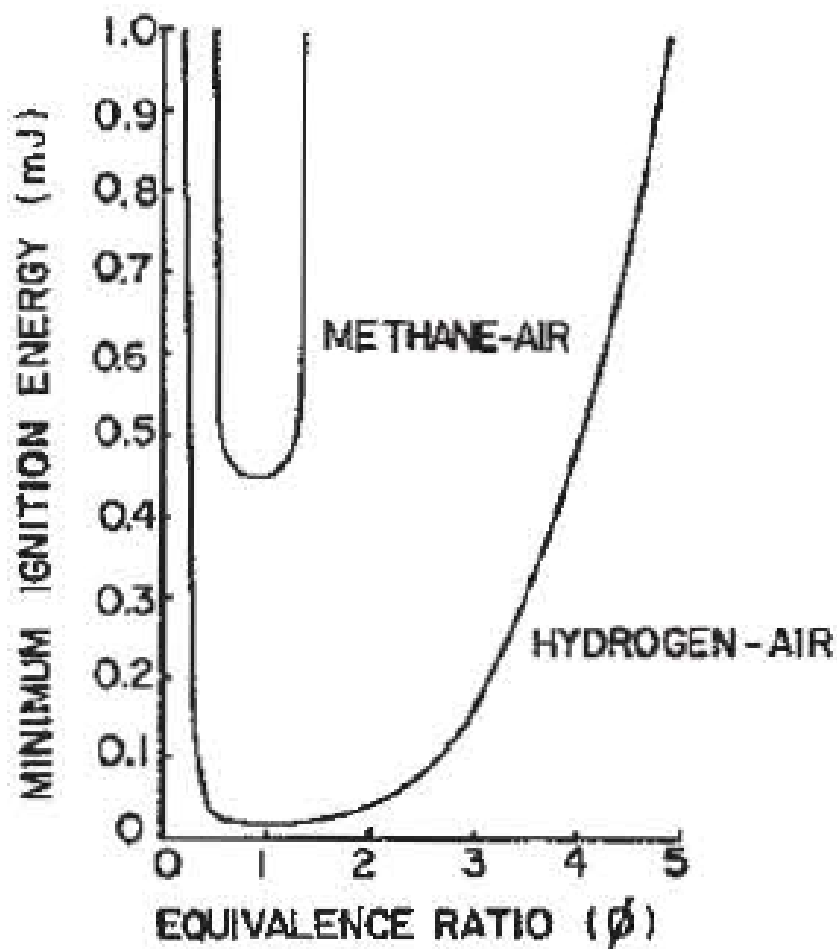
Figure 2-1 Minimum ignition energy as a function of equivalence ratio for hydrogen-air and methane-air mixtures [40]

2.1.1.3   Quenching gap

In the combustion chamber, the combustion flame is typically extinguished a certain distance from the cylinder wall due to heat losses. For hydrogen, the quenching distance is

10

less than that of gasoline. Thus, it is more difficult to quench a hydrogen flame than a gasoline flame. The smaller quenching distance can increase the tendency for backfire since the flame from hydrogen/air mixture can more readily get past a nearly closed intake valve than the flame from a hydrocarbon/air mixture.

2.1.1.4 *Self-ignition temperature*

The self-ignition temperature is the temperature that a combustible mixture must reach before it will be ignited without external source energy. For hydrogen, the self-ignition temperature is relatively high. This is important implications when the charge is compressed. The self-ignition temperature is an important factor in determining what compression ratios can be used by engine. The high self-ignition temperature of hydrogen allows larger compression ratios to be used in a hydrogen engine without increasing the final combustion temperature beyond the self-ignition temperature and causing premature ignition. On the other word, hydrogen is difficult to ignite in a compression ignition or diesel configuration, because the temperature needed for this type of ignition are relatively high.

2.1.1.5 *Flame speed*

The flame speed of hydrogen is nearly an order of magnitude higher than that of gasoline. For stoichiometric mixtures, hydrogen engine can more closely approach the thermodynamically ideal engine cycle. However, at leaner mixtures, the flame velocity decreases significantly.

2.1.1.6 *Diffusivity*

Compared to other hydrocarbon fuel-air mixtures, it is highest for hydrogen because of its fast chemical kinetics and high diffusivity. The high diffusivity is advantages for hydrogen. Hydrogen gas is highly diffusive and highly buoyant; it rapidly mixes with the ambient air upon release. The diffusion velocity is proportional to the diffusion coefficient and varies with temperature according to T^n with n in the range of 1.72-1.8. Diffusion in multi-component mixtures is usually described by the Stefan-Maxwell equation. Corresponding diffusion rates of hydrogen in air are larger by about a factor of 4 compared to those of air in air. The rising velocity under the influence of (positively) buoyant forces cannot be determined directly, since they are dependent on the density difference between hydrogen and air as well as on drag and friction forces. Also shape and size of the rising gas

volume as well as atmospheric turbulence have an influence on the final velocity of the rising gas. The positive buoyancy of hydrogen is a favorable safety effect in unconfined areas, but it can cause a hazardous situation in (partially) confined spaces, where the hydrogen can accumulate, e.g., underneath a roof. Both diffusion and buoyancy determine the rate at which the gas mixes with the ambient air. The rapid mixing of hydrogen with the air is a safety concern, since it leads very soon to flammable mixtures, which on the other hand for the same reason also will quickly dilute to the non-flammable range. Therefore it is estimated that in a typical unconfined hydrogen explosion, only a fraction of the gas mixture cloud is involved releasing in fact not more than a few per cent of the theoretically available energy.

2.1.1.7 Density

The density of hydrogen is extremely low. The low in density can creates a problem as below:

1. Large volume of storage is necessary to store enough hydrogen to give a vehicle an adequate driving distance.
2. The energy density of hydrogen air charge, and hence the power output reduced.

2.1.1.8 Thermal efficiency

Thermal efficiency of a hydrogen engine is typically greater than gasoline engine. In hydrogen engines, larger compression ratios than those use in gasoline engines can be used since the self-ignition temperature of hydrogen is high. This mean the temperature of the burnt gases can be lowered resulting in higher specific heat ratios. The combined effect of larger compression ratios and larger specific heat ratios increases the thermal efficiency for hydrogen fueled engines [41].

2.1.1.9 Emission

The most important advantages of hydrogen as fuel is they emit fewer pollutants than other fossil fuels. In principle, hydrogen exhausts are water and some nitrogen oxides (NOx). There are almost nothing or very low emission of unburned hydrocarbons, carbon monoxide (CO), carbon dioxide (CO2), oxide of sulfur (SOx), and smoke from hydrogen fueled engine. If a hydrogen engine burns excess oil, hydrocarbon and CO emission can become significant but still less than the emission produce from a gasoline engine [42].

2.1.1.10 Power output

Power output is one of important parameter when evaluating the performance of an engine. Power output is derived by converting the chemical energy of the fuel into mechanical energy. Figure 2-2 shows a comparison of the heat output of hydrogen and gasoline engine for various conditions. A stoichiometric mixture of gasoline and air and gaseous hydrogen and air pre-mixed externally occupy ~2% and 30% of the cylinder volume. The energy of the hydrogen mixture is only 85% that of the gasoline mixture, resulting in about 15% reduction in power. The loss of power using an external mixed hydrogen/air mixture can be conceptualized in terms of engine displacement. For example, a 2.3 liter gasoline engine has a power output comparable to a larger 2.7 liter hydrogen engine at stoichiometric conditions or 6 liter hydrogen engine operating at an equivalence ratio of 0.4. The power output of a hydrogen engine can be improved using more advanced fuel injection techniques as shown in Figure 1. If liquid hydrogen us premixed rather than gaseous hydrogen, the amount of hydrogen that can be induced into the combustion cylinder can be increased by approximately one-third and the power output increased about 37%. The output can be further increased by directly injecting hydrogen into the cylinder under high pressure. Using this technique, the maximum amount of both air and hydrogen are introduced into the combustion chamber resulting in a 20% increase in power compared to a gasoline engine using a carburetor and 42% increase in power compared to a pre-mixed gaseous hydrogen mixture [38].

Fuel	17cc	300cc	405cc	420cc
Air	983cc	700cc	965cc	1000cc
Energy	840cal	710cal	970cal	1010cal
(%)	(100)	(85)	(115)	(120)

(a) Gasoline engine   (b) Gas Hydrogen pre-mixed   (c) Liquid Hydrogen pre-mixed   (d) High Pressure hydrogen injection
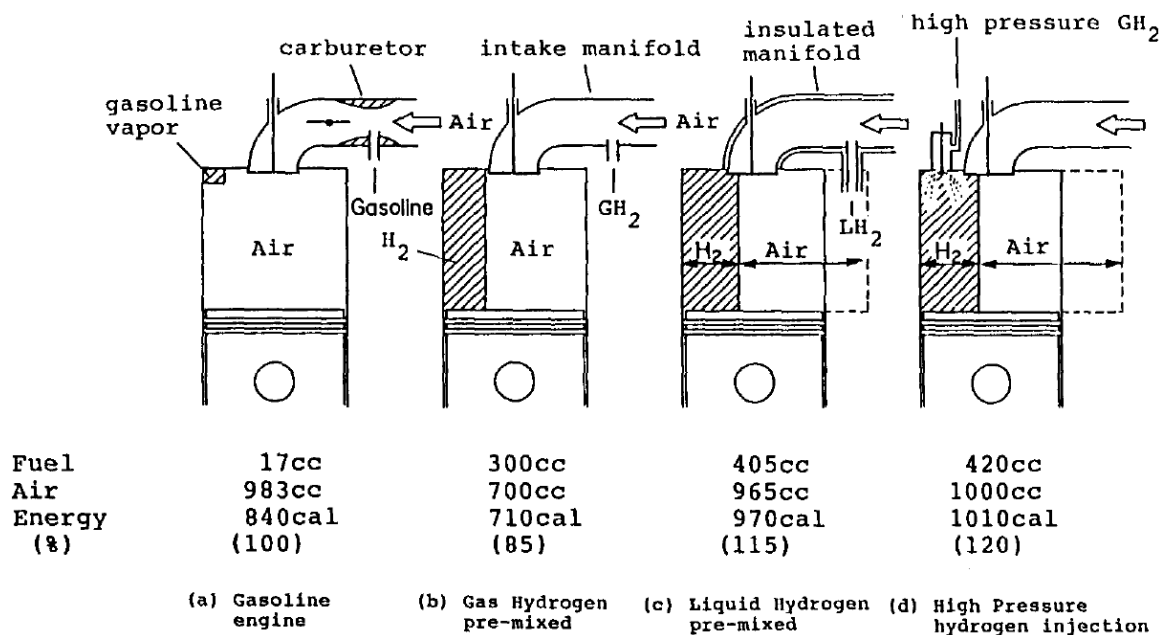
Figure 2-2 Comparison of maximum calorific value (output) of a fuel-air mixture in a 1000cc displacement volume engine [43]

13

2.2 Flow and jet

2.2.1 Overview of Flow

2.2.1.1 Steady flow

A steady flow is one in which the conditions (velocity, pressure and cross-section) may differ from point to point but do not change with time. Mathematically speaking for steady flows,

$$\frac{\partial P}{\partial t} = 0 \tag{1}$$

where P represents a fluid property. However, the properties may vary from point to point. Which means that they could be a function of space (i.e., $T = T(x, y, z)$, $p = p(x, y, z)$ and $\rho = \rho(x, y, z)$). In the study of fluid mechanics it is often to assume that the flow is steady to simplify the analysis but yet give a realistic representation of the real flow field. On the other hand, most flows encountered in real world applications are unsteady flows.

It should be noted, steady flow does not mean the velocity and accelerations are constant. Flow in a curved pipe or through a nozzle may be steady, but the velocity or acceleration are not constant. This is a common misconception based in part on particle dynamics for rigid bodies.

2.2.1.2 Unsteady/non-steady flow

If at any point in the fluid, the conditions change with time, this fluid flow will be said unsteady flow.

$$\frac{\partial P}{\partial t} \neq 0 \tag{2}$$

Here P represents a fluid property. The fluid properties are function of time (i.e., $T = T(x, y, z, t)$, $p = p(x, y, z, t)$ and $\rho = \rho(x, y, z, t)$). Unsteady flows can be further divided into periodic flow, nonperiodic flow and random flow. For periodic flow, the property change is repeated in a predictable manner whereas the fluid motion and properties are difficult to predict in random flow as in turbulent flow.

2.2.1.3   Laminar flow

Laminar flow is an ordered flow of a liquid or gas, in which the fluid moves in layers parallel to the direction of flow. Laminar flow is observed in very viscous fluids. It also occurs when the velocity of flow is sufficiently low and during the slow flow of a liquid around small objects. Specifically, laminar flow occurs in narrow (capillary) tubes, in the lubricant layer in bearings, and in the thin boundary layer that forms near the surface of a body over which a fluid is flowing. If the velocity of flow of a given fluid is increased, the laminar flow, at a certain instant, may undergo a transition to a disordered turbulent flow. As this occurs, the resistance to the motion of the fluid is changed drastically. The mode of flow of a fluid depends on the Reynolds number Re. If the value of Re is smaller than a certain critical value Ren, then laminar flow occurs. If Re > Recr, then the flow can become turbulent. The value of Recr depends on the type of flow being considered. For instance, for flow through circular tubes, Recr ≈ 2,200 (if it is assumed that the characteristic velocity is the velocity averaged across the cross section of the tube and that the characteristic dimension is that of the tube's diameter). Consequently, at Recr < 2,200, the flow of the fluid in the tube will be laminar. The output of liquid from a tube during laminar flow is determined by the Poiseuille law.

2.2.1.4   Turbulent flow

Turbulent is a type of liquid or gas flow in which the liquid or gas elements move in a random or unsteady manner along complex trajectories. Such motion results in strong mixing between the layers of the moving liquid or gas. The turbulent flows that have been studied in the greatest detail include the following: flows in pipes, in channels, and in boundary layers around bodies immersed in a liquid or gas flow; free turbulent flows, or jets; the wakes behind bodies moving relative to a liquid or gas; and mixing zones between flows of differing velocity that are not separated by any solid walls. Turbulent flows differ from the corresponding laminar flows in that the turbulent flows have a complex internal structure, a different distribution of the averaged velocity over a cross section of the flow, and different overall characteristics, that is, a different dependence on the Reynolds number Re of the flow rate, the resistance coefficient, and the average mean velocity over a cross section or the maximum velocity. The averaged velocity profile of a turbulent flow in a pipe or channel differs from the parabolic profile of the corresponding laminar flow in that the former is

characterized by a faster increase in velocity at the walls and a smaller curvature in the central part of the flow.

2.2.2 Overview of jets

Jets is a type of fluid flow either a liquid or gas that passes through a fluid with properties, such as velocity, temperature, or density, different from those of the jet. The jet flow is an extremely common phenomenon that exists in many forms, from the stream ejected through the exhaust nozzle of injector to the ambient atmosphere. Commonly, it was studied by examining the changes in the velocity, density, temperature, and concentration of the component fluids both in the jet and in the ambient fluid. Jet flows are classified according to the main characteristics of interest for simplifying various problems. An important category of jet flow consists of jets issuing from a nozzle or orifice in the wall of a container. Most of the jets are classified as round, rectangular, plane, etc., depending on the cross-sectional shape of the orifice or nozzle. If the streamlines of a jet are parallel at the nozzle exit, the jet is said to exhibit axial flow.

2.2.2.1 *Steady jets*

Jets are canonical flows that have been widely studied by many researchers, especially steady jets. In a direct-injection engine, the fuel will be injected by injector and the fuel jets then will propagates across the combustion chamber. Understanding the physics of the gas jet is necessary to understand the behavior of the fuel jet injected into an engine cylinder. Although the main concern with automotive injection is the transient behaviour, steady jets can provide a basis for understanding the structure and scaling of the transient jet. The behaviours of steady state jets are discussed in this section.

2.2.2.2 *Structure of steady jets*

The basic structure of a steady jet includes a potential core that has not felt the effects of viscosity and, therefore, has a velocity equal to that at the nozzle exit. Next, the flow goes through a transitional development region, and then finally becomes fully developed. Figure 2-3 diagrams the regions of a steady circular jet.
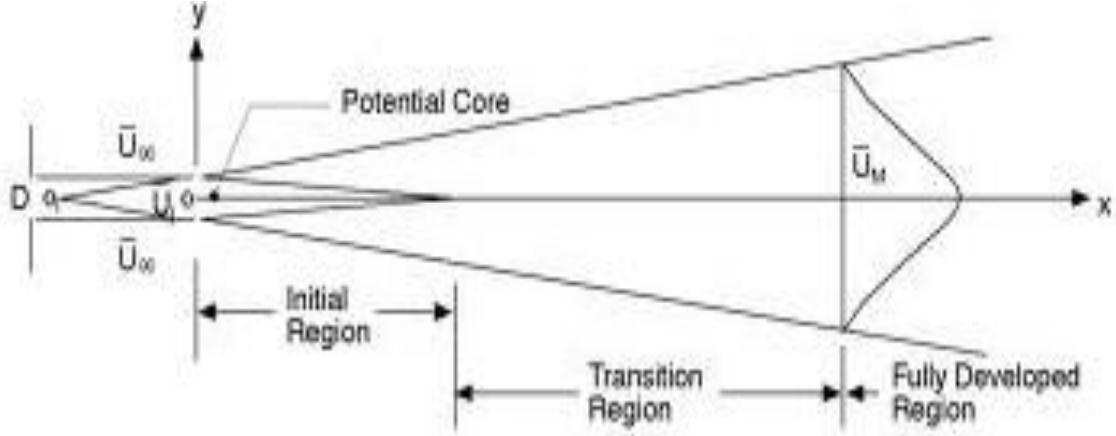
Figure 2-3 Definition sketch of circular turbulent jets [44]

In the fully developed region the flow becomes self-similar and the radial velocity profile, U(r,z), normalized by the centreline velocity, UCL, is only a function of the nondimensional distance, $\eta = 2r/dn$, where r is the radial position and dn is the diameter of the nozzle exit. These relations are represented in equations (1) and (2).

$$\frac{U(r,z)}{U_{CL}} = f(\eta) \qquad (3)$$

And

$$\frac{U_{CL}}{U_n} = \frac{k_d}{z/d_n} \qquad (4)$$

where z is the distance from the exit, un is the flow velocity at the nozzle exit, and kd is a constant. As seen in equation (2), the centreline velocity scales with the inverse of distance from the exit plane.

2.2.2.3 Transient jets

The structure and properties of incompressible transient jets or impulsively started jets have been studied for a wide range of applications. Turner described the structure of plumes when studying atmospheric mixing in buoyant plumes. A plume was described as consisting of a spherical cap, called a spherical head vortex, which is supplied with additional buoyancy

and momentum from a plume below. It was shown that the plume displays self-similarity characteristics throughout its evolution. Figure 2-4 illustrates this initial description of a jet or plume. The jet consists of a spherical vortex flow interacting with a steady-state jet. The vortex of radius R_v moves away from the nozzle at a bulk velocity that decays with the distance z from the nozzle. The size of the vortex grows continuously due to the entrainment of mass from the steady-state jet which pushes it from behind. The jet behind the vortex is considered to be in a steady state, which is confirmed by the work of Kuo and Bracco [45].
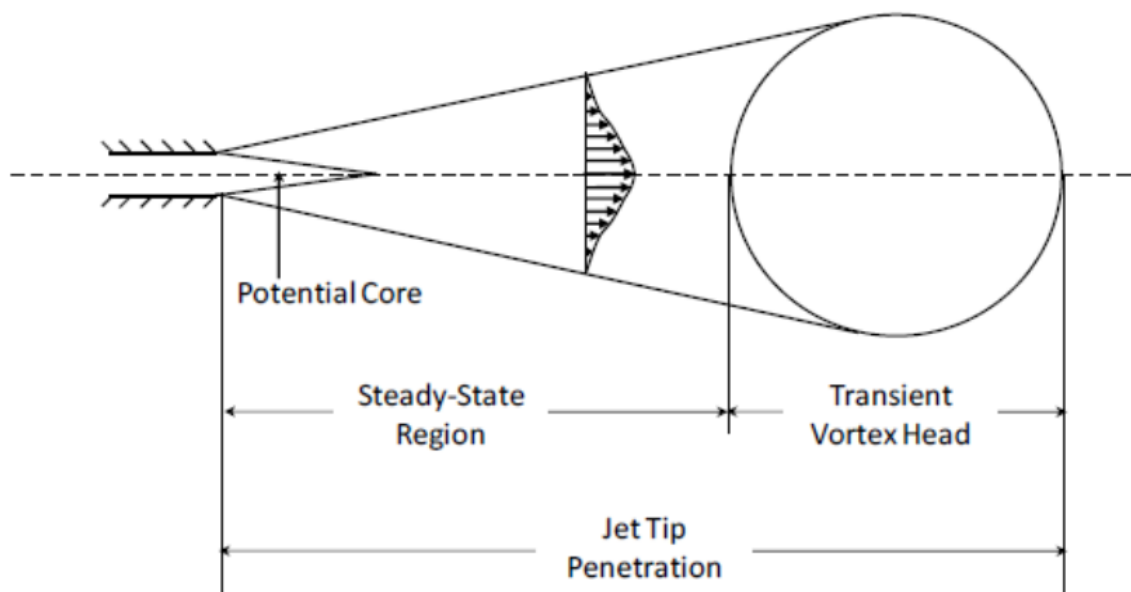
Figure 2-4 Turbulent transient jet model [46]

Turner's plume was used as the basic structure of a transient starting jet by many researchers. Abramovich and Solan [47] used this model to develop analytical expressions for the velocity of the spherical vortex in the near and far fields of a liquid jet under laminar conditions with low Reynolds number. It was observed that the velocity of the spherical vortex varies proportional to the distance similar to the axial velocity of a steady state jet only with differing constants. The velocity of the spherical vortex was found to be approximately half that of a fluid element in a steady jet. It showed that the half width and maximum axial velocity show similarity characteristics, both making the jet appear to start from a virtual

origin different from the geometric origin. The virtual origin was found to be proportional to the exit diameter and the square root of the Reynolds number.

2.2.2.4 *Incompressible transient jets*

The compressibility effects in a flow can be neglected if the maximum Mach number is below 0.3. Incompressible jets have been studied extensively in the past [47][48]. As one fluid is injected into another fluid with uniform pressure field, a mixing layer is formed between the two fluids. Mass from the surrounding fluid is entrained in the injected fluid. Experimental investigations by Ricou and Spalding [48] concluded that, the rate of entrainment is proportional to the distance from the nozzle and to the mass injection rate for incompressible air jets issued from the round nozzle into stagnant air. A steady-state jet can be divided into three regions [49]. In the initial region the velocity in the potential core of the jet remains constant and is equal to the initial velocity. The end of the initial region is marked by the disappearance of the potential core because of the thickening of jet boundary layer. The transition region may be defined as the region in which the jet viscosity distribution becomes fully developed. In the fully developed region, the velocity profile is self-similar.

2.2.2.5 *Compressible transient jets*

When the pressure ratio between the outlet and inlet of an orifice or nozzle is sufficiently dropped to cause the pressure at the exit to be higher than the ambient surroundings, the complex flow that results is termed an under expanded jet. At the nozzle exit the flow is choked and expands upon leaving the nozzle. A complex pattern of expansion waves result at the outer rim of the exit as shown in Figure 2-5. The expansion waves reflect from the free boundary of the jet and become compression shocks that form a barrel shaped structure that is terminated by a normal shock also called the Mach disk. The Mach disk forms if the nozzle exit to chamber pressure ratio is above 2.1 [50]. Flow immediately after the Mach disk is subsonic, but these barrel shock structures can be repeated several times diminishing in strength due to viscous effects. For moderately under expanded flows with a nozzle to chamber pressure ratio below 2.1, a Mach disk does not form and instead the barrel shock is able to intersect at the flow axis [50].

2.2.3 Reynolds and Mach number

Jets are a fluid flow in which a stream of one fluid mixes with a surrounding medium, at rest or in motion. Such flows occur in a wide variety of situations, and the geometries, sizes, and flow conditions cover a large range. Jet flows vary greatly, depending on the values of two numbers which is Reynolds and Mach number.

2.2.3.1 Reynolds number

A central role in determining the state of fluid motion is played by the Reynolds number. In general, a given flow undergoes a succession of instabilities with increasing Reynolds number and, at some point, turbulence appears more or less abruptly. It has long been thought that the origin of turbulence can be understood by sequentially examining the instabilities. This sequence depends on the particular flow and, in many circumstances, is sensitive to a number of details. The flow regime depends on three physical parameters describing the flow conditions. The first parameter is a length scale of the flow field. If the length scale is sufficiently large, a flow disturbance may increase and the flow may be turbulent. Second parameter is a velocity scale such as spatial average of the velocity; for a large enough velocity the flow may be turbulent. The third parameter is the kinematic viscosity; for a small enough viscosity the flow may be turbulent. The three parameters can be combined into a single parameter which was named Reynolds number. This Reynolds number defined as

$$\text{Re} = \frac{\rho V L}{\mu} \tag{5}$$

where ρ is the density, V is a characteristic velocity (for example, the jet exit velocity), L is a characteristic length (for example, the jet diameter), and μ is the viscosity. Fluid flows are laminar for Reynolds Numbers up to 2000. Beyond a Reynolds Number of 4000, the flow is completely turbulent. Between 2000 and 4000, the flow is in transition between laminar and turbulent, and it is possible to find sub regions of both flow types within a given flow field.

2.2.3.2 Mach number

Jets are described as liquid, gas, or plasma flows, depending on the material properties of the fluid. In a jet composed of compressible gases, the ratio of the exhaust velocity V of the

gas to the propagation velocity a of sound waves is important. This ratio is called the Mach number $M = V/a$. The Mach number is an index that used to define the following flow regimes:

(1) Subsonic, where M is less than 1 everywhere throughout the flow

(2) Supersonic, where M is greater than 1 everywhere throughout the flow

(3) Transonic, where the flow is composed of mixed regions of locally subsonic and supersonic flows, all with local Mach numbers near 1, typically between 0.8 and 1.2

(4) Hypersonic, where (by arbitrary definition) M is 5 or greater.

The most important physical aspect of Mach number is in the completely different ways that disturbances propagate in subsonic flow compared to that in a supersonic flow. Shock waves are a ubiquitous aspect of supersonic flows. Shock waves is a region characteristic of the supersonic flow of a gas. In this region, the velocity of the gas abruptly decreases, and a corresponding increase occurs in the pressure, temperature, density, and entropy. The thickness of a shock wave in the direction normal to its surface is the distance over which the change in the gas parameters occurs. The thickness of a shock wave in the direction normal to its surface is the distance over which the change in the gas parameters occurs. This thickness is small—of the order of the mean free path of the molecules—and is therefore neglected in most problems of gas dynamics. When a fluid flows through a jet nozzle, it chokes with relatively small pressure difference and accelerates to supersonic velocities. If the fluid pressure at the nozzle exit is still higher than that of the ambient free space, then the fluid jet assumes the configuration illustrated in Figure 2-5 and is called a supersonic underexpanded free jet. The jet is expanded radially at the nozzle exit and the jet boundary also forms an expanded shape. The expansion waves originating at the nozzle exit corner are reflected at the jet boundary as compression waves, which coalesce to form the so-called barrel shock. The barrel shock is oblique to the flow and the flow behind it is still supersonic. The flow that passes through the barrel shock is again compressed by the reflected shock shown in Figure 2-5 and separated from the flow behind the Mach disk by the slip line. Along the jet axis, the pressure continuously decreases to values below the ambient pressure value. The pressure is increased to the ambient pressure value by passing through the Mach disk.
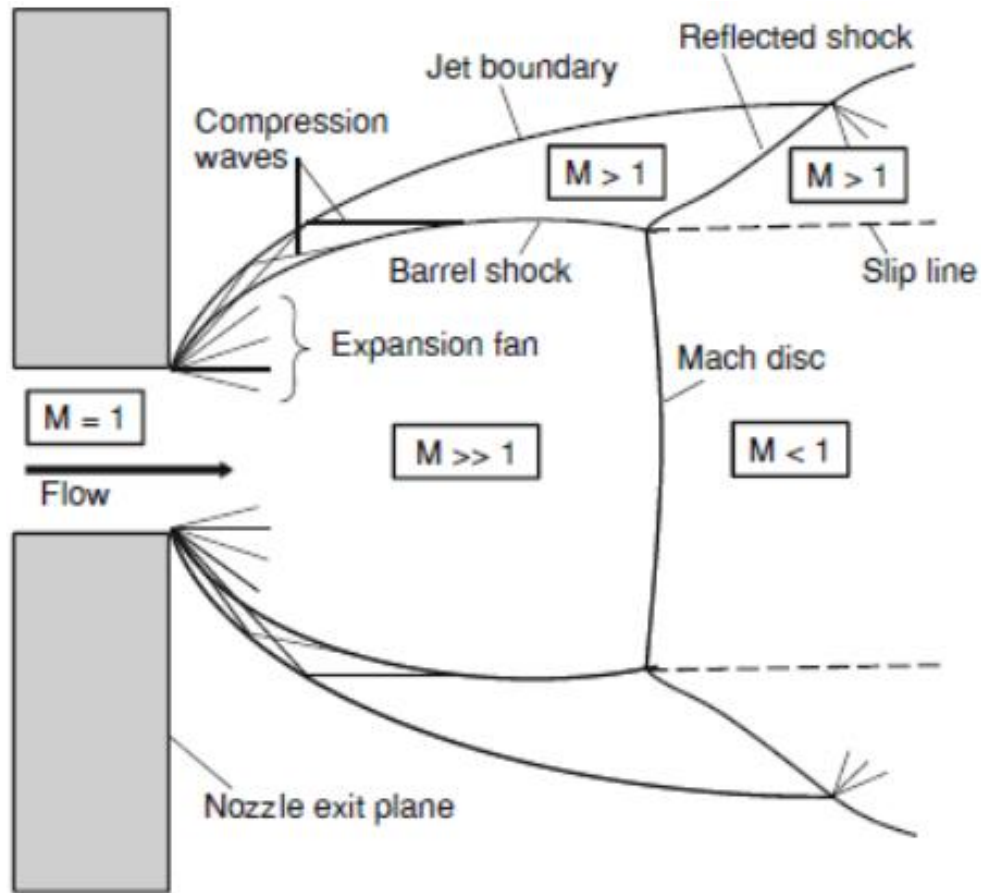
Figure 2-5 Schematic of under expanded jet[51]

2.3 Hydrogen mixture formation

Hydrogen induction techniques play a very dominant and sensitive role in determining the performance characteristics of the hydrogen fuelled internal combustion engine (H_2ICE). Hydrogen fuel delivery system can be broken down into two main types including the port injection and the direct injection

2.3.1 External mixing system and backfire

The lean limit of hydrogen for combustion is 0.135, while it is 0.7 for gasoline. Therefore, that precise control of the air to fuel mixing ratio by means of a carburettor is not required and an external mixing system of very simple construction as indicated in Figure 2-6

is widely used. With this system the theoretical output power is as low as 85% of that of gasoline engine and virtually backfire takes place at around 50% of the level of gasoline engine and places a limit on the output power. Backfire can be define as a phenomenon where pre-ignition advances at every cycle and finally it occurs before the intake valve is close results the flame spreads to the hydrogen mixed with air in the intake manifold through the gap of the valve and causing the explosion. Pre-ignition is a problem much more serious in hydrogen engines then in other internal combustion engines because of the lower ignition energy, the wider range of flammability and the smaller quenching distance of hydrogen. The appearance of backfire is difficult to predict. Generally, backfire arises at high thermal loads. A problem with external mixture formation not directly related to combustion is that it causes an inherently low volumetric efficiency. The low density of hydrogen causes the intake hydrogen to consume 30% of the aspirated air volume. This causes a reduction in the maximum mean effective pressure and energy density inside the engine, reducing power output. The only option is to increase the intake pressure, but pre- ignition limits the possible amount of boosting [52]. Several studies have investigated the cause or causes of pre-ignition in hydrogen engines. The precise causes are not known with certainty, but the following are put forward:

1. Hot spots like spark plugs, exhaust valves, carbon deposit
2. Residual gas
3. Pyrolysis of oil
4. Back flow of burning gases during intake process (crevices)
5. Catalytic effects

Possible adaptations to prevent backfire are:

1. The use of cold-rated spark plugs, in order to have low surface temperatures on the tip. A waste spark ignition system has to be avoided. Using an ignition coil with grounding will avoid residual voltage on the spark plug.
2. The use of cooled exhaust valves (e.g. sodium cooled exhaust valves)
3. A cooling system designed to provide uniform coolant flow rates.
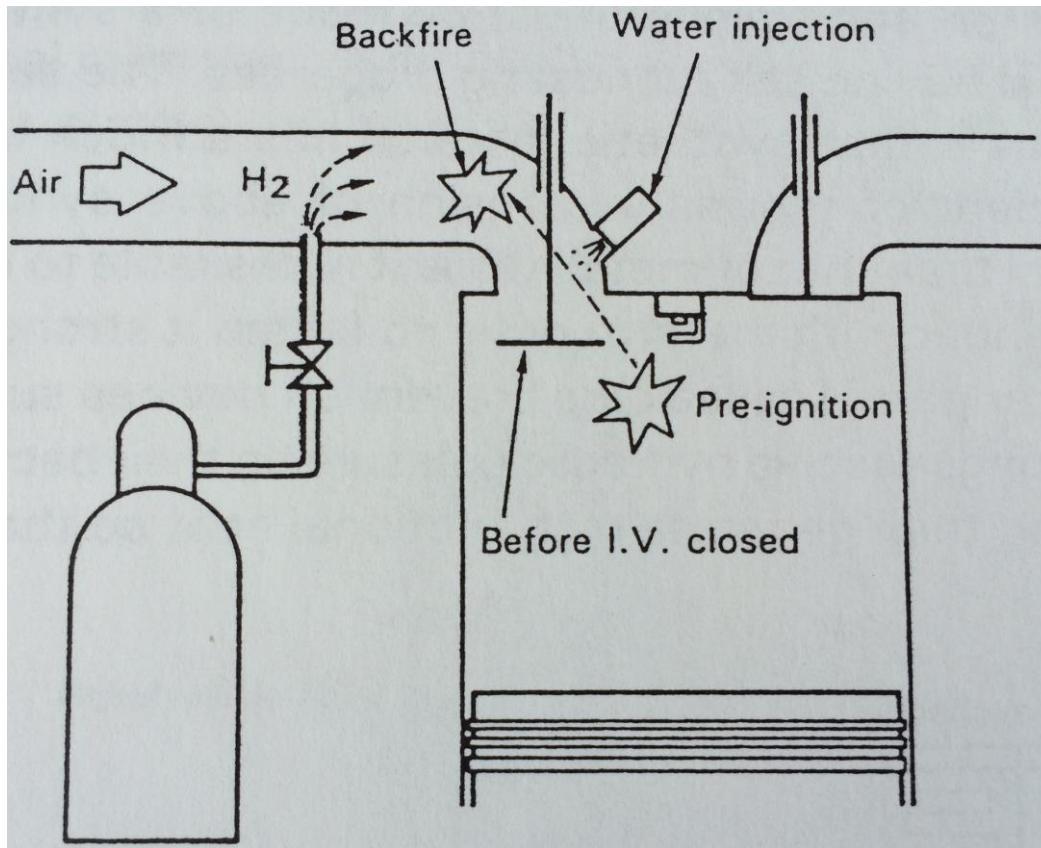
Figure 2-6 External mixing H_2 engine with backfire [38]

2.3.2   Internal Mixture Formation

There are major challenges of hydrogen in direct injection conditions which is abnormal burning such as knock, pre-ignition and backfire that occurs at higher engine loads. The problem prevents a reliable operation and restricts the engine power. A significantly higher burning velocity leads to lower the thermal efficiency compared with other gaseous fuels because of an increase in heat loss due to the knock-like explosive combustion [5,53–55]. To overcome such problems with hydrogen engines, internal mixing of hydrogen has been examined by some researchers [12,56,57] and many researchers was conducted study on the effect of hydrogen jet at many condition [15,17,58–70]. Generally, internal mixing of hydrogen is achieved by high-pressure injection systems. This technique is very effective to prevent the backfire and knock especially under the high engine loads. Internal mixture formation, or direct injection, can eliminate many of the combustion abnormality. The achievement of best combustion can be achieved by controlling the timing of injection.

Injecting the hydrogen after the intake valve has closed effectively eliminates the possibility of backfire. As to injection timing there will be two choices as describe below:

1. Low pressure injection: Hydrogen is injected upon closing of the intake valve for rather a long period at a low pressure of around 1 MPa.
2. High pressure injection: Fuel is injected when the piston is around TDC for a short period at a pressure higher than 8 MPa, as in the case of diesel engine.

Also, the hot residual gases are more easily mixed with cool air with direct injection, reducing pre-ignition. At a stoichiometric ratio, 30% more air can be delivered to the cylinder when hydrogen is injected after the intake valve is closed, resulting in much higher energy density capabilities and a better volumetric efficiency [52]. Parameters such as start of injection and injection duration also play an important role in performance and emissions and can be optimized with direct injection.

To promote proper mixing and to supply sufficient amounts of hydrogen to the cylinder, high pressure gas injectors are required. Wallner et al. studied the effect of the injector location and nozzle design on the efficiency and emissions of a direct-injection hydrogen engine. Researchers at Argonne National Laboratory has been carrying out intensive research on advance direct injection and mixture formation concepts in single cylinder engine[13,14,71,72]. Their tested new injector technologies allow performing late injection (thus reducing the losses for compression work) and delivering higher mass flow rates during injection, and then extending the operation range to higher engine load and speed, where the maximum efficiency can be achieved. Koyanagi et al. [15] have shown that using higher injection pressures in a hydrogen DISI engine results in more stringent conditions for spark placement. Hydrogen diffusion in the radial direction was diminished near the spark gap point with increasing injection pressure, resulting in hydrogen concentrations approaching the upper flammability limit more rapidly. Higher jet penetration also was observed with increasing injection pressures. Roy et al. [17] was study the structure of the jet in addition to other physical processes resulting from hydrogen gas injection. The results show that the jet penetration rate increased with increasing injection pressure, and decreased with increasing ambient pressure. They also observed that the combustion characteristics of the hydrogen jets can be controlled by varying the fuel injection timing. The fuel injection timing relative to ignition timing is an important parameter to control the combustion characteristics in

hydrogen direction-injection combustion. In conclusion, the mixing characteristic of DI hydrogen engine in order to optimize the efficiency is a subject of ongoing interest.

2.4 DISI engine

For over a century in the history of internal combustion engines, two concepts of engine have played a dominant role during the process of development and production. The spark ignition or gasoline engine shows the good feature of high specific power and large speed range due to its good level of air utilization while the compression ignition or diesel engine, offers better thermal efficiency from the use of a higher compression ratio, and the absence of throttling. Combining the positive aspects of these two engine types has always been a goal of engine research and development in the automobile industry, and the Direct Injection Spark Ignition (DISI) engine is seen as one of the most promising ways to achieve the aim. The concept of DISI engines has gained an interest in recent years as a way of reducing fuel consumption and emissions under the current strict legislations, due to the improvements in fuel injection technology as well as advances in the understanding of the processes involved in mixture preparation and stratified charge combustion.

2.4.1 Fundamental and benefit of DISI engine

The demand for a perceptible lowering of specific fuel consumption in the SI engine led to the development of combustion processes with internal mixture formation, i.e. with direct injection into the combustion chamber. The primary advantage that direct injection offers as opposed to conventional SI procedures with external mixture formation is the possibility to carry out a qualitative load regulation at part load instead of quantitative load regulation with the throttle valve. An engine can thereby take in air almost without throttling losses in the charge changing process. Because of the lean global air ratio ($\phi > 1$) necessary for this combustion process a so-called charge stratification must be realized in the combustion chamber, which secures that sufficient rich and thus ignitable mixture is in the region of the spark plug at ignition timing. Figure 2-7 shows the homogeneous (early injection) and the stratified-charge modes. In the wall-guided procedure, the mixture cloud resulting from the injection jet is led to the spark plug across a corresponding deformation in the piston. In the air-guided process, this task is taken over by a tumble (an air swirl around a horizontal axis) directed toward the injection spray. This tumble must be generated across the

geometry of the intake ports during the inflow process into the combustion chamber. Finally in the spray-
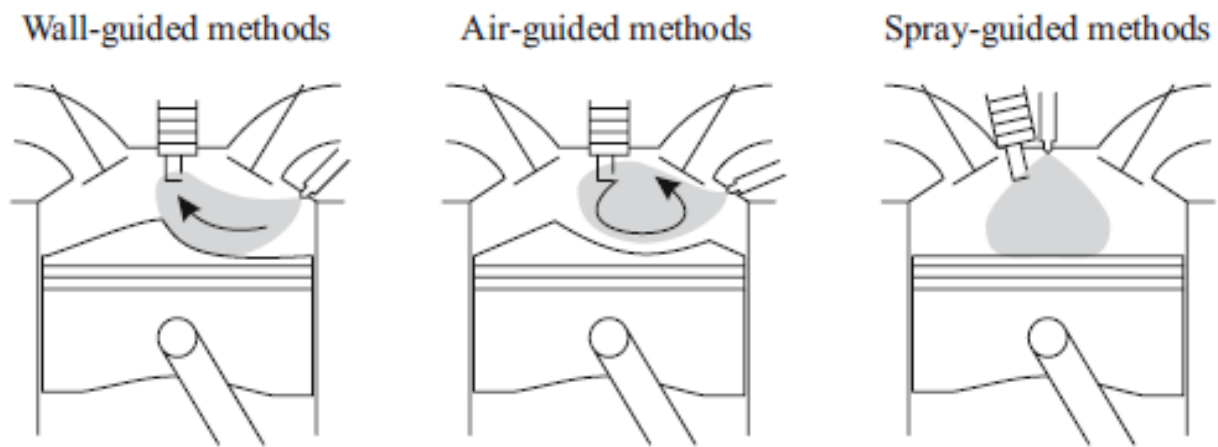
Figure 2-7 Combustion process in direct injection spark ignition engines

guided method, the intake valve and the spark plug are located very close to each other and control of mixture formation and thus the obtainment of an ignitable mixture at the spark plug can result exclusively across the injection spray itself. It is obvious that this procedure represents the greatest challenge since flow condition in the combustion chamber varies significantly with engine speed and load. On the other hand, spray-guided injection offers the most potential in reference both to the lowering of fuel consumption and raw emissions and to the extension of the charge stratification area in the engine map.
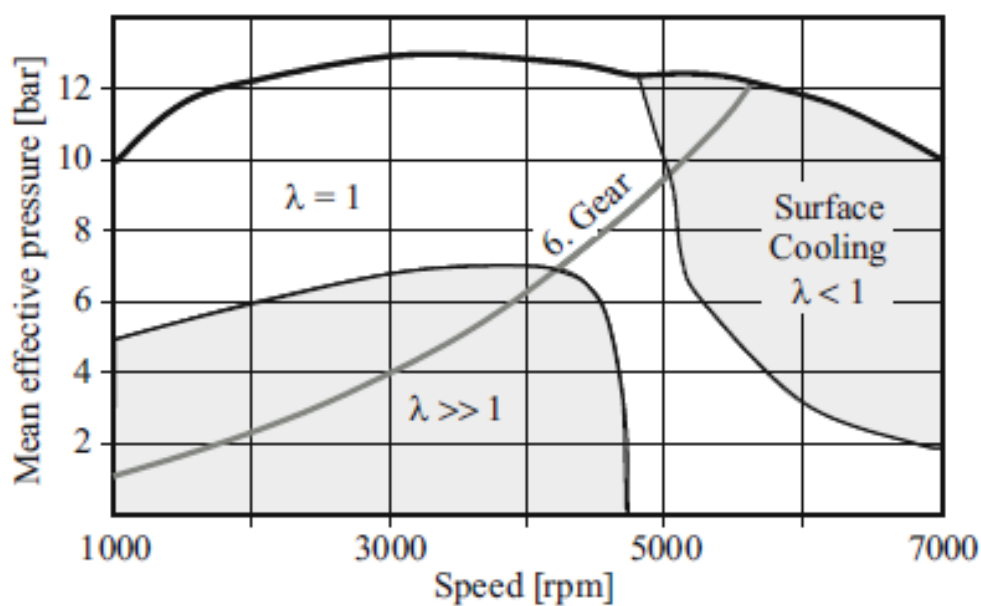
Figure 2-8 Modes of operation in the characteristic map of a DISI engine

27

Figure 2-8 shows the extension of the charge stratification area for a spray-guided combustion process. As follows from this, a direct injection spark ignition (DISI) engine cannot be operated in the entire speed/load map in stratified charge mode. At higher load and the large fuel quantity to be injected associated with it, the mixture cloud would be too rich and thus result in unacceptably high particulate emissions. On the other hand, at higher engine speeds, the absolute available time for mixture formation is too short to secure a sufficient mixture quality. Besides the higher efficiency, the DISI engine can be operated at higher compression ratios since the danger of knocking decreases as a result of the direct ignition (evaporation with heat absorption) of the fuel injected directly into the combustion chamber. Also resulting from the internal cooling is a greater filling and thus an approximately 3-5 % higher full load torque as opposed to an engine with multi point injection, since the latter already uses a part of the injection effect through the intake valve.

2.5   Techniques to measure fuel concentration

Knowledge of the fuel concentration, fuel number density or fuel–air ratio is important for all types of DISI engines including hydrogen DISI engine. Generally, DISI engines are operated un-throttled in ultra-lean conditions by stratifying the charge and providing a fuel-rich mixture around the spark plug [73,74]. The spray-guided system generates a stratified fuel concentration near the spark plug in a DISI engine due to the direct injection of fuel toward the point [75,76]. The mixture equivalence ratio near the spark plug at the time of spark discharge are important for successful of ignition in lean-burn SI engines. The fuel concentration around the spark plug together with the fluid motion strongly influence the duration of combustion initiation. This causes cycle-to-cycle variation, which can become large in lean-burn engines [77]. Some researcher [5,78–80]performed study Effect of compression ratio, equivalence ratio and engine speed on the performance and emission characteristics of a spark ignition engine using hydrogen as fuel. Their report found that compression ratio and equivalence ratio have a significant effect on both performance and emission characteristics of the engine and have to be carefully designed to achieve the best engine performance characteristics. The flow field in the combustion chamber and the fuel concentration around the spark plugs should be optimized. The fuel concentration or fuel/air ratio around the spark plug in direct-injection spark ignition engines are particularly important for better understanding of its contribution on combustion and emissions.

28

A variety of techniques have been used previously to measure local fuel concentration or the fuel air ratio in SI engines, including infrared (IR) absorption, relationship between the ion current and air/fuel (A/F) ratio. Laser diagnostic methods has also been developed, including Raman scattering, Rayleigh scattering, laser-induced fluorescence (LIF) or Planar laser induced fluorescence (PLIF) methods and Laser-induced breakdown spectroscopy (LIBS).

2.5.1 Linear Raman scattering

Raman spectroscopy is a spectroscopic technique based on inelastic scattering of monochromatic light, usually from a laser source. Inelastic scattering means that the frequency of photons in monochromatic light changes upon interaction with a sample. Photons of the laser light are absorbed by the sample and then reemitted. Frequency of the reemitted photons is shifted up or down in comparison with original monochromatic frequency, which is called the Raman Effect. This shift provides information about vibrational, rotational and other low frequency transitions in molecules. A Raman photon is emitted if a molecule then undergoes a transition to a higher vibrational energy state than its original state (Stokes-Raman) to a lower energy vibrational state (Anti-Stokes Raman). Figure 2-9 shows the difference in energy or wavelength of a scattered light from a material is characteristic for a particular bond in its molecular structure. The various energy shifts associated with different molecular vibrations leads to a Raman spectrum which is unique for each molecule and provides a precise spectral fingerprint. Raman spectroscopy can be used to study solid, liquid and gaseous samples. In recent years, several papers have been published in which Raman scattering was used for the investigation of mixture formation processes, exhaust gas recirculation, and cold start phenomena of conventional [81] or propane fired spark ignition engines [24,82]. When applying Raman scattering for the investigation of engines with direct fuel injection, the occurrence of droplets is an additional source of disturbance, because the elastically scattered light from fuel droplets can generate signal intensities which are up to 20 orders of magnitude larger than the Raman signals. Linear Raman scattering has been used for the investigation of the mixture formation inside an optically accessible gasoline direct injection spark ignition engine [25]. The concentrations of O2, N2, H2O, and isooctane have been measured simultaneously and cycle resolved along a line of nearly 1 cm at three different locations inside the combustion chamber. By means of polarization-resolved detection optics, it was possible to separate the highly polarized Raman signals from

unpolarized contributions from light emissions by stray light from surfaces, background luminescence, or laser-induced fluorescence. However, this measurement technique provides very small signal intensities, so its careful adaptation to the particularity of the test object is very important for successful utilization.
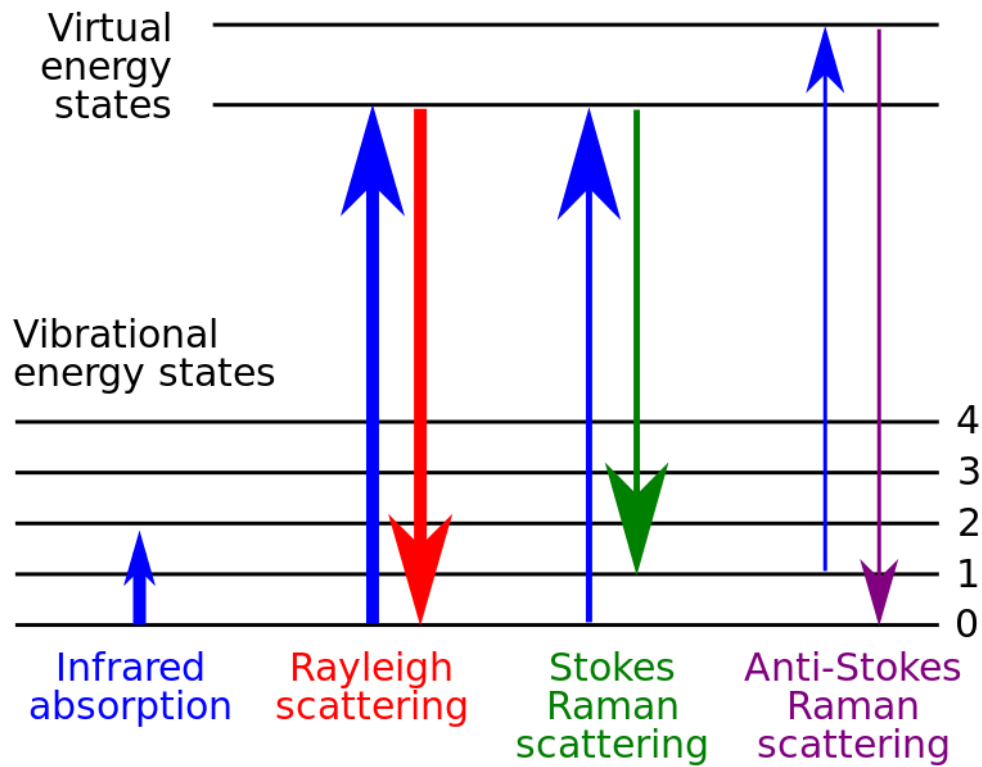
Figure 2-9 Energy-level diagram showing the states involved in Raman signal. The line thickness is roughly proportional to the signal strength from the different transitions.

2.5.2 Ion current and air/fuel (A/F) ratio

Several papers have reported a relationship between the ion current and air/fuel (A/F) ratio [83–85]. Although it is easy to detect the ion current using a spark plug, the measurement accuracy is poor because unaccounted disturbances such as fuel deposits, fuel additives, and air humidity that affect the ion current. Fuel concentrations have been measured in situ using infrared absorption [18–20,86–92]. In particular, 3.392 lm He–Ne lasers have been used to obtain fuel concentrations for combustion diagnostics. Some of the authors developed an infrared (IR) optical spark plug sensor with a double-pass measurement

length[87,91]. The measurement accuracy was confirmed by measuring the concentration of a homogeneous methane–air mixture in a compression–expansion engine. The spark plug sensor was also applied to a practical spark-ignition (SI) reciprocating engine using isooctane as fuel, and the fuel concentration measured using the sensor agreed with the pre-set concentrations under firing conditions. Figure 2-10 shows the optical sensor installed in a spark plug. This sensor was constructed by modifying a commercial instrumented spark plug. Consequently, it was possible to measure the fuel concentration near the spark plug under firing conditions by replacing a standard spark plug with this spark-plug sensor. A 3.392-lm He–Ne laser (8 mW) and an IR detector (MCT: Mercury Cadmium Tellurium; HdCdTe) were used for this sensor system. This technique can also be used to measure the gasoline concentration. Since the molar absorption coefficient of gasoline is required for such measurements, the pressure and temperature dependence of this coefficient have been investigated. Kawahara et al.[20,87] applied a 3.392 μm infrared absorption technique to quantify the instantaneous gasoline concentration near the spark plug by developed an in situ laser infrared absorption method using a spark plug sensor and a 3.392 μm He–Ne laser as the light source. The results show that during the compression stroke, the characteristics of the mixture formation near the spark plug differed according to the injection timing. They also was among the first to investigate the possibility of obtaining fuel concentration measurements near the spark plug in a test engine[92]. Subsequently, Tomita et al. used an optical sensor with a pair of sapphire rods, the tips of which were cut at an angle of $\pi/4$ radians, to pass laser light through the combustion chamber of a practical engine and discussed some of the factors that affected measurement accuracy[19,89]. Laser infrared absorption technique indicates higher measurement uncertainty even in lean mixture conditions. However, the mixture is ignited near the spray plume or the vapour mixture around the spray in a spray-guided DISI engine, so it is important to measure the equivalence ratio at the spark point. It is very difficult to measure the fuel/air ratio inside an engine cylinder, even using the absorption technique, due to the lack of absorption bands at visible and infrared wavelengths.
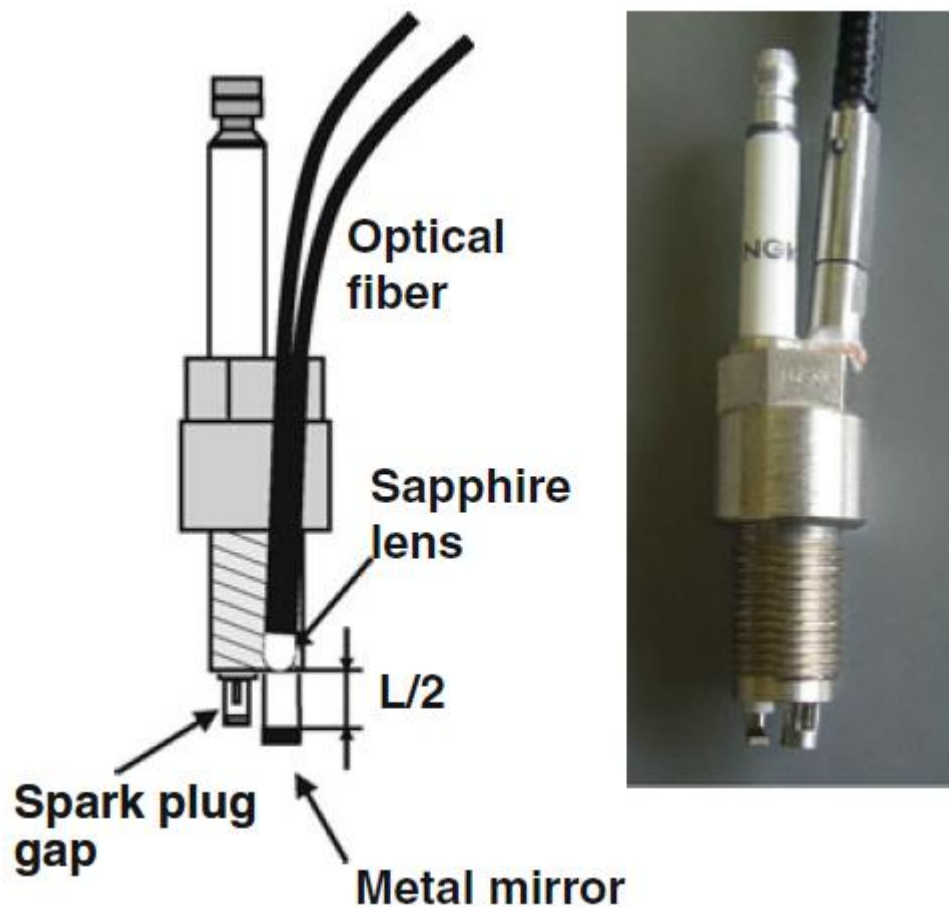
Figure 2-10 Schematic diagram and photograph of an IR spark-plug sensor [20]

2.5.3 Laser-induced fluorescence (LIF) and Planar laser induced fluorescence (PLIF)

Laser diagnostics are widely used in fundamental combustion science, research, and development to investigate transient phenomena without influencing the system under study by inserting probes and surfaces. LIF technique is frequently used for remote detection of concentration and temperature. LIF technique measurements have been widely used because the LIF signal is strong and provides two-dimensional fuel concentration data at specific time. Some researchers was study the method for identifying fuel/tracer mixtures suitable for LIF measurements of in-cylinder equivalence ratios[76,93–99]. Volker et al.[76,94] reported in his

paper potentially adverse effects that added tracers might have on mixture formation, combustion, and the faithful representation of the base fuel and describes alternative techniques to tracer-based measurements that allow studies of fuel/air mixing processes in practical devices. His results shown that quantitative equivalence ratio maps are shown for the fuel injection event within a single cycle in a spark-ignition direct-injected engine, showing the ability of the technique to not only reveal static fuel concentration maps, but also the motion of the fuel cloud along with very steep gradients. Spray velocities determined from the moving fuel cloud are in agreement with previous particle image velocimetry measurements. Tomita et al. [21]applied the PLIF method in order to study the fuel concentration distribution in the transient hydrogen jet. The results from the study show that each transient hydrogen jet had different configurations and concentrations distribution. Kaiser et al. [23] performed an optical study of mixture preparation in a hydrogen-fueled engine using PLIF technique. Their report shows the increasing of injection pressure related with nozzle design. Figure 2-11 shows the simplified PLIF experimental facility. In particular, LIF measurements have been widely used because the LIF signal is relatively strong and provides two-dimensional fuel concentration information at a specified time. However, these optical methods require changes in the engine combustion chamber design because of the need for optical windows. Therefore, these methods are difficult to apply to commercial engines.

Figure 2-11 simplified PLIF experimental facility

33

2.5.4 Laser-induced breakdown spectroscopy (LIBS)

Laser-induced breakdown spectroscopy (LIBS) (or laser-induced plasma spectroscopy, LIPS) has advanced dramatically due to the availability of online real-time information on a surrogate material with no sample preparation[100]. Many researchers was conduct t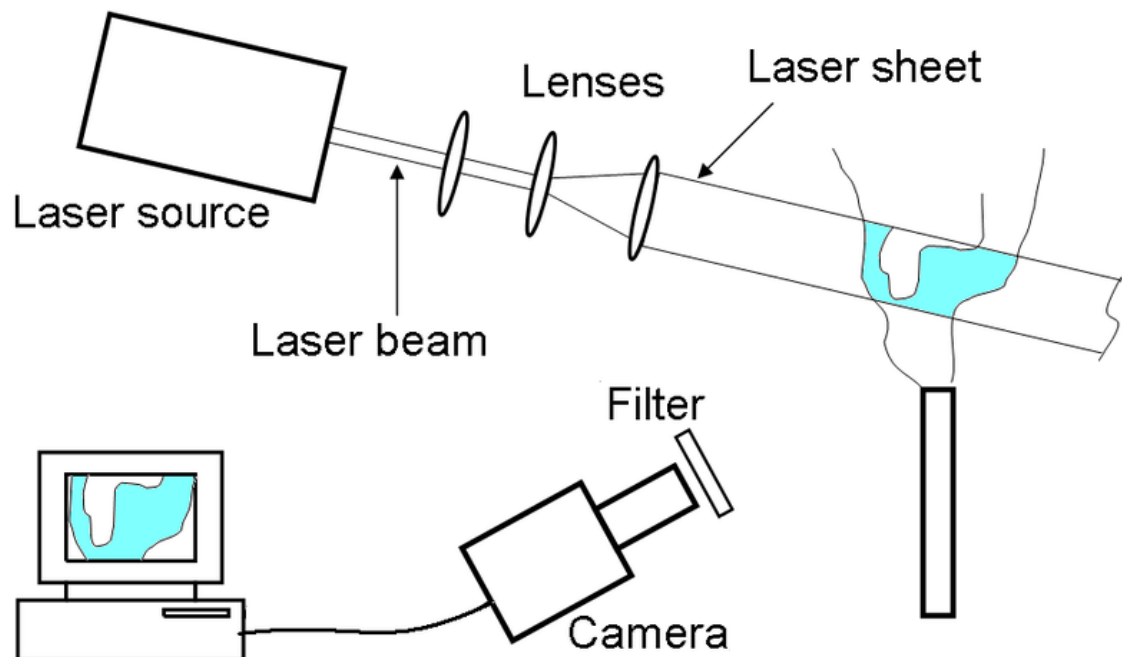he study by using LIBS technique[26–28,100–110]. LIBS of gases are possible using high power laser pulses. When a short-pulse laser is focused into air or other gases, the laser beam creates localized plasma. The collection and spectral analysis of the plasma emissions allows the qualitative identification of atomic species. Figure 2-12 shows the Schematic diagram of experimental apparatus for Laser Induced Breakdown Spectroscopy (LIBS). Kawahara et al.[109] was conducted measurement the equivalence ratio using LIBS and discussed the accuracy of spatially, temporally, and spectrally resolved measurements. Tran et al. [26] have investigated the use of laserinduced gas breakdown for measuring the fuel-to-air ratio of CH4–air mixtures. He examined the response of the radiation intensity ratio of the Hα-lines at 656.3 nm and the OI triplet near 777.5 nm as a function of the equivalence ratio and the laser energy. They found that LIBS has a potential for in situ and non-intrusive measurements of the fuel-to-air ratio of a combustible environment for the equivalence ratio from 0.1 to 5.0, the radiation intensity ratio of the Hα-lines to the OI triplet increased linearly with the equivalence ratio. Phuoc et al.[27] used a laser induced spark to measure the ignition and fuel-to-air ratio of CH4-air and H2-air combustible mixtures simultinously using the measured spectral peak ratio Hα (656 nm)/O (777 nm). Ferioli et al. [103,106] performed study using LIBS technique on engine exhaust gas to illustrate the ability of LIBS technique to measure the equivalence ratio of SI engine using the ratio of C/O and C/N atomic peaks derived from the spectra measurement. Shudo et al.[28] applied LIBS technique as a method to measure the hydrogen concentration distribution in the direct injection stratified charge. Measurement of instantaneous local equivalence ratio by the method clears the characteristics of mixture formation in hydrogen direct injection stratified charge. Sturm and Noll [105]have examined the averaged LIBS emission of various C, H, O, and N, ratios in mixtures of air, CO2, N2, and C3H8 to determine the calibration curves for various elements, and elemental ratios as a function of mixture composition. They applied doublepulse laser breakdown of 8-ns pulse width and 250-ns interpulse separation generated at 10 Hz repetition rate by polarization coupling of orthogonally polarized output beams, to increase the plasma signal. They concluded that, the plasma emission signals increased as a result of irradiation with closely spaced double laser pulses. Windom et al.[110] investigated double-pulse LIBS effects of an

orthogonal configuration on the atomic emission response for purely gaseous of nitrogen and oxygen, analyzing the spectral emission lines of them. They observed that, measurements for the gaseous system resulted in no notable improvements with double-pulse configuration as compared to the single-pulse LIBS. The rather poor response of double-pulse LIBS for analysis of strictly gas-phase species provides additional insight into the physics of the plasma–analyte interaction, and further supports the concept of preferential analyte depletion within the expanding plasma for pure gas-phase analysis, compared with liquid and solid responses. Although the LIBS technique has a potential in engine measurements, it is difficult to apply a LIBS method to equivalence ratio measurements around a spark plug due to the difficulty with laser access in a practical SI engine. Spark plugs must be used in spark-ignition engines to initiate flame ignition.
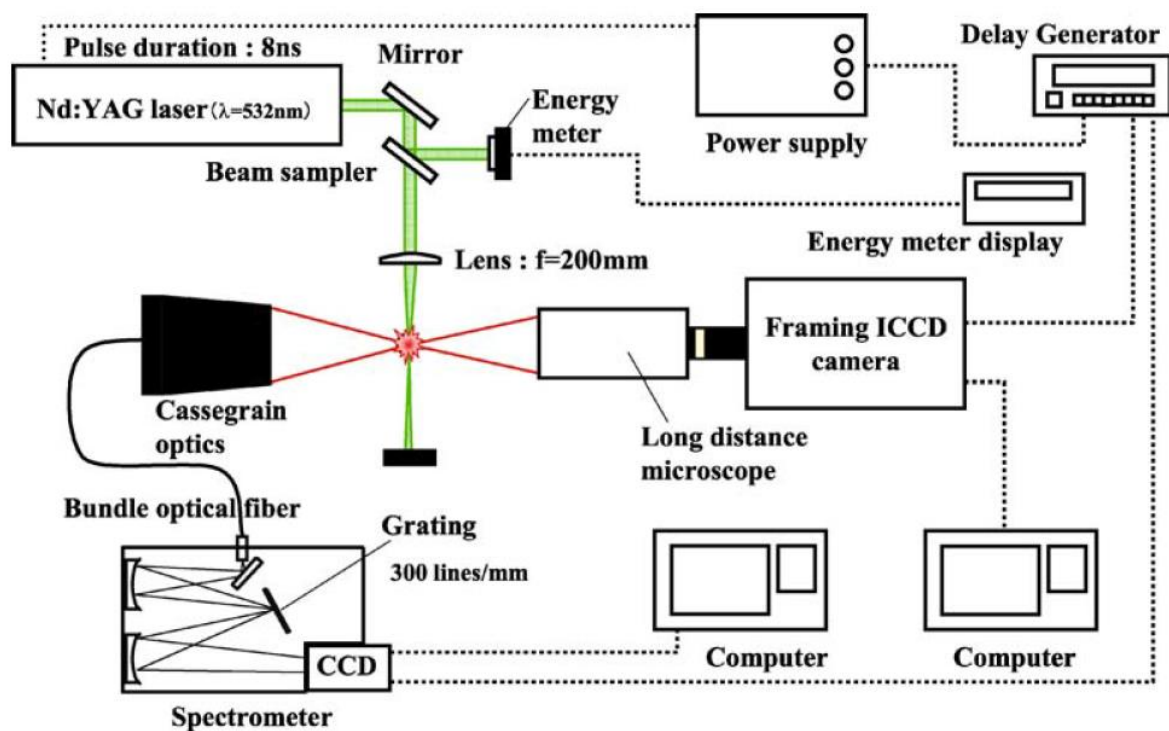

Figure 2-12 Schematic diagram of experimental apparatus for Laser Induced Breakdown Spectroscopy (LIBS) [109]

2.5.5 Spark induced break down spectroscopic (SIBS)

Quantitative measurements of cycle-to-cycle variations in the mixture strength around the ignition site are comparatively rare for practical hydrogen SI engine. Merer et al. [111] observed the light emissions from a spark discharge by inserting a fiber optic cable through the centre electrode of a spark plug, to investigate the possibility of determining the fuel-air ratio in the spark gap at ignition with spectroscopy. He observed the total broadband light emission from the spark and the light emission centred at 385 nm from the cyanogen radical (chemical formula CN) for varied f and residual gas concentrations. Fansler et al. [33] conducted measurement of local fuel concentration in internal combustion engines using spark-emission spectroscopy. The results show that for stratified operation with fixed fuel-injection timing, a spark timing that is later than optimum leads to incomplete combustion in many cycles due to fuel-air ratios that are too lean for good ignition and rapid flame development. Letty et al. [101] analyzed emission spectra from electrical and laser sparks in flowing methane–air mixtures of various compositions and discussed the differences and similarities between the electrical and laser sparks in the context of their emission. The emission spectra from the laser spark were characterized by a weak continuum, onto which several strong atomic lines and some molecular bands were superimposed, in contrast to the spectra of electrical spark where a strong continuum, few atomic lines and several strong molecular bands were evident, making thus the laser spark spectroscopy a more accurate technique to measure hydrocarbon concentration. Kawahara et al. [34] was investigated the spectrally resolved emission spectra of plasma generated by a spark plug using spark-induced breakdown spectroscopy (SIBS) technique for its potential to measure local fuel concentrations in a premixed mixture. In their work they noted that their newly developed spark-plug sensor had the applicability and feasibility to investigate laminar premixed flame in a CH4/air mixture. It shows that the Spark-induced breakdown spectroscopy (SIBS) can directly measure the mixture of equivalence ratio near the spark plug at the time of spark discharge. SIBS techniques is a best technique that can directly measure the fuel concentration inside a combustion chamber due to the usage of conventional spark plug. Figure 2-13 shows the conventional spark plug used as a SIBS sensor. The spark-plug sensor was developed from a commercial spark plug used in mass-produced real-world SI engines. The electrical spark which generated between two electrodes ablated a sample material, which is vaporized, atomized, and excited. The emission characteristics can be determined from the elemental composition of the sample. Figure 2-14 shows the light collecting area of optical

fiber and the emission intensity results. The UV-grade quartz fiber optic was inserted in the spark plug to collect the light emission produced from spark discharge. For current research, the development was made on the spark plug sensor by using the spark plug gap to 1.5 mm to increase the stability of spark-discharge initiation, and optical UV-grade quartz fiber with a core diameter of 1000 μm (fiber diameter 1250 μm) was used to increase the light-collecting capability of the device.

Ground electrode

Figure 2-13 Photograph of conventional spark plug use as SIBS sensor
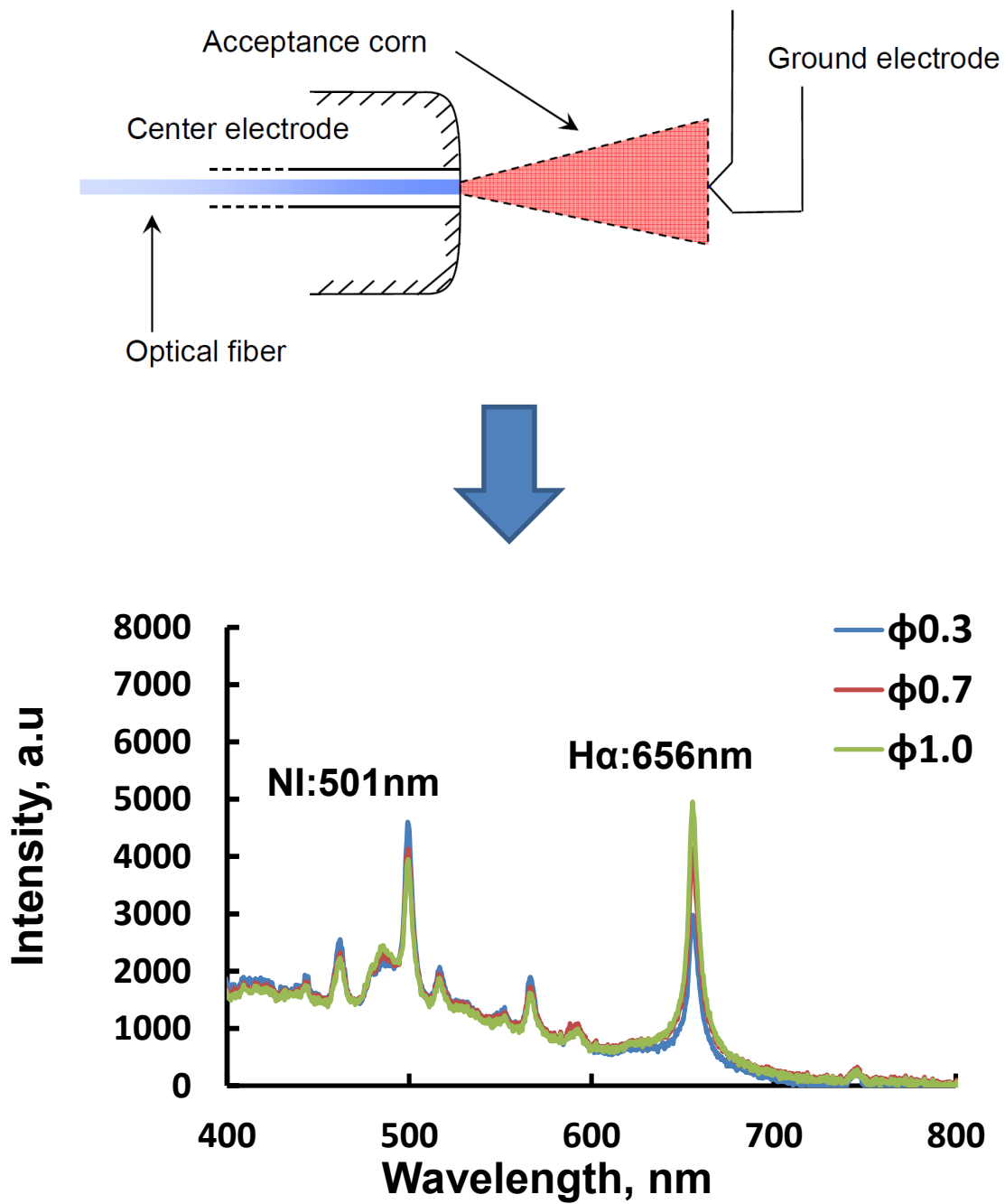
Figure 2-14 Diagram of light collecting area of optical fiber and the emission intensity results

2.6 Summary

Chapter 2 discussed about the hydrogen properties and the benefit when it use in combustion. The basic flow was discussed in order to understand the concept of fluid during combustion process. The techniques to measure equivalence ratio was describe as many technique such as Linear Raman scattering, Ion current, Laser-Induced fluorescent (LIF), Planar laser induced fluorescent (PLIF), Laser-induced breakdown spectroscopy and Spark-induced breakdown spectroscopy (SIBS) was used to study the fuel concentration. The techniques proposed by other researchers require changing in the engine combustion chamber design for optical access from outside and difficult to be applied to concentration measurements for practical SI engines. The main purpose of this study is to measure the fuel concentration near the spark plug. Therefore, the use of SIBS technique (developed SIBS sensor) for measuring the hydrogen jet concentration was proposed as a suitable technique that can directly measure the fuel concentration inside of the engine cylinder with only changing the spark plug.

3 Apparatus and method of present study

3.1 Constant volume vessel

Figure 3-1 shows the assembly design of constant volume chamber (CVV) with spark plug sensor. The constant volume chamber (CVV) used in the experiment consist of several main parts as below:

1) Body part
2) Chamber head
3) Window collar
4) Optical window
5) Spark plug port
6) Spark plug stopper
7) Spark plug sensor

Figure 3-1 Assembly design of constant volume chamber. 1.Body part; 2.Chamber head; 3.Window collar; 4.Glass window; 5.Spark plug port; 6.Spark plug stopper; 7.Spark plug sensor

3.1.1 Body part

Figure 3-2 shows the body part of constant volume chamber. The constant volume vessel made from stainless steel (SUS303) has a cylindrical shape and a volume of 675cm^3 (diameter: 80mm, Length: 125mm). Many researchers used a cylindrical chamber due to the following advantages:

1) It is possible to achieve total line-of-sight optical access of the entire chamber.

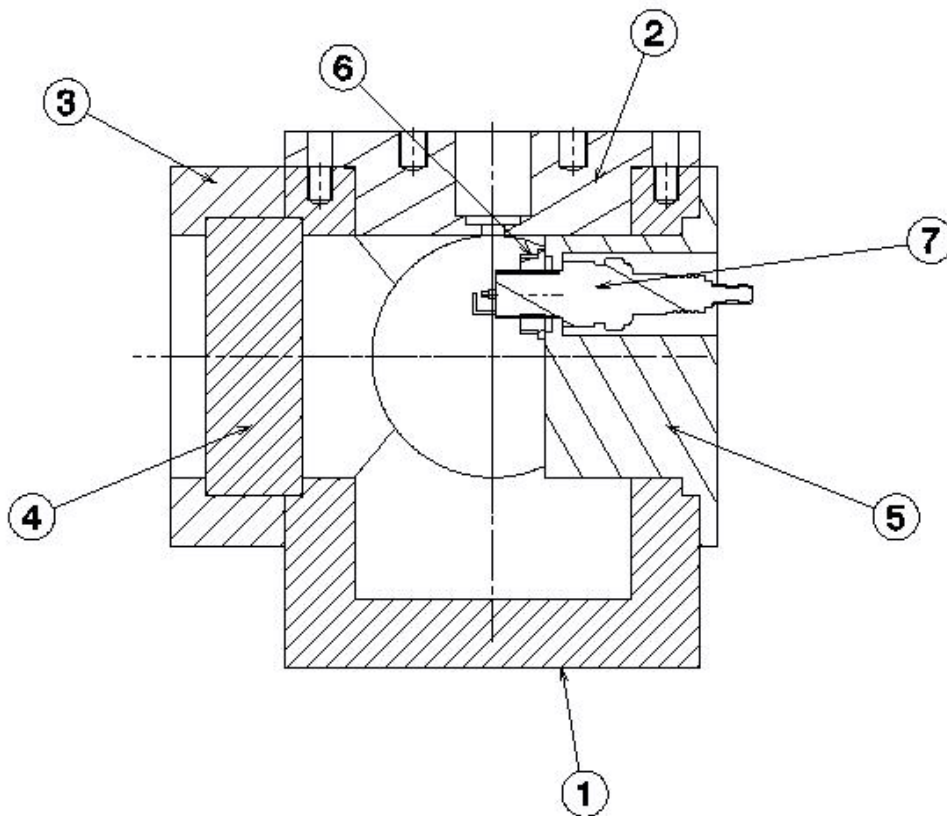2) It is not too far different from the geometry in an engine cylinder.

3) Can use with standard injector nozzles in the following respects.

    a. Both fuel impingement and flame quenching on chamber walls can be easily avoided.

    b. The optical access attainable for a relatively small chamber volume is favorable.

4) Temperature homogeneity is easy to achieve by means of forced turbulence.

3.1.2 Chamber head

Another important part in constant volume chamber is Chamber head. The injector was installed on the top of the chamber so that the direction of the jet was perpendicular downward into the cylinder. The design of chamber head is shown in Figure 3-3 Design of chamber head.

3.1.3 Window collar

When researching fuels and their combustion characteristics, it is of particular benefit to have optical access to the chamber in which the combustion or spray occurs. For this experiment, the three walls of the chamber designed to locate circular quartz windows to allow optical access to the chamber whereas window collar was designed to hold the circular windows to the CVV. The benefit derived from this optical access is a much greater scope for accurate measurement and for knowledge attainment of spark characteristics. The design of circular quartz window and window collar are shown at Figure 3-4 Design of window collar.

3.1.4 Optical window

The design of optical window is shown at Figure 3-5. To obtain optical access to a combustion vessel, a transparent material that satisfies the temperature requirement and has sufficient strength properties to suit the application must be found. The material used for the

current experiment for optical windows was made from silica windows. The tensile strength of silica is about 50 MPa; however, according to General Electric Quartz, it is common practice to use below 6.8 MPa for safety and fatigue reasons.

3.1.5 Spark plug port and stopper

The other side of wall, spark plug port was designed to locate the SIBS sensor. Figure 3-6 shows the design of spark plug port with stopper which is designed by consider the leakage problems that always occurred when the experiment was conducted in high ambient pressure. Here, O-ring with internal diameter 15.8mm and 2.4 of thickness (Model no. P-15 – Kayo Corporation) was used together with spacer to avoid leakage. The details calculation of making the design of spark plug port was shown in Table 3-1 and Figure 3-7.

3.1.6 Spark plug sensor

Figure 3-8 shows a design of spark-plug sensor for measurement of local equivalence ratio of hydrogen jet. The spark-plug sensor developed for this experiment is a commercial spark plug use in practical SI engines. The details about spark plug sensor will be explained in next sub-chapter.
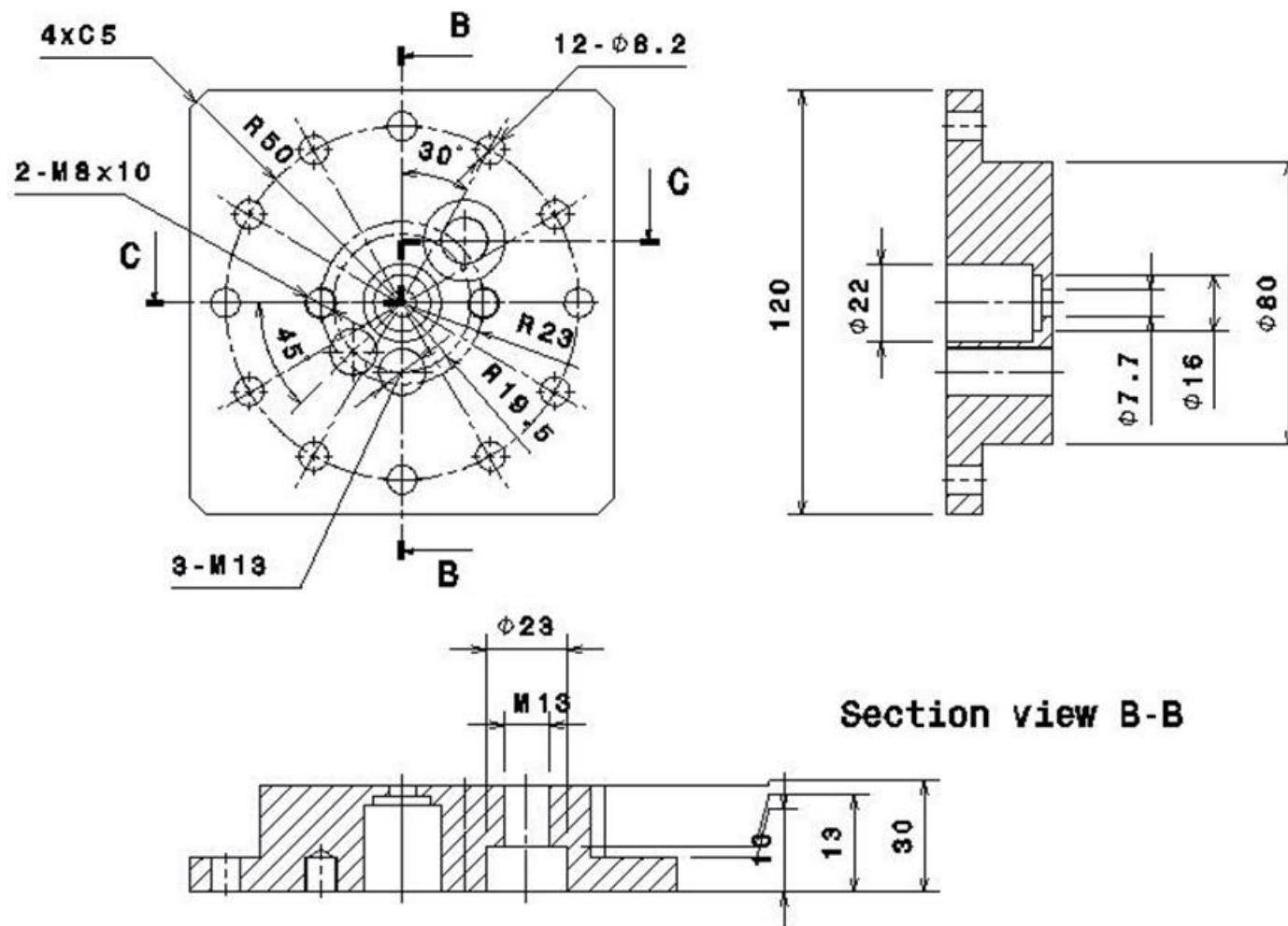
Section view A-A

Figure 3-2 Design of body part of constant volume chamber

43

Figure 3-3 Design of chamber head

44

8x8.2

D

46°

22.5°

R47.5

D

33

23

Φ70

Φ80

Φ110

Section view D-D

Φ110

33

Figure 3-4 Design of window collar

45
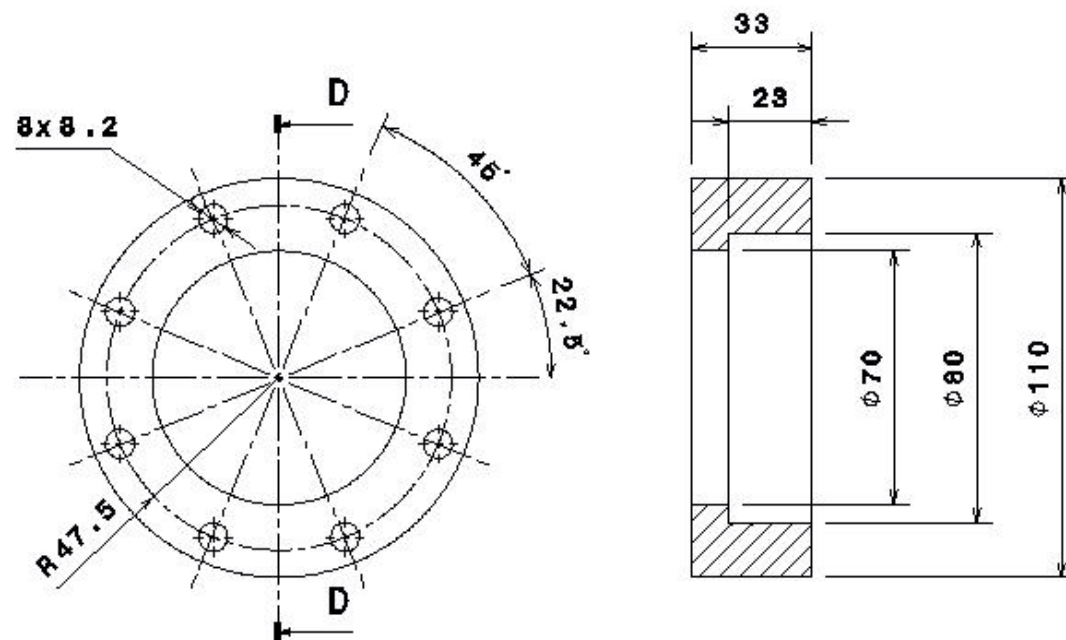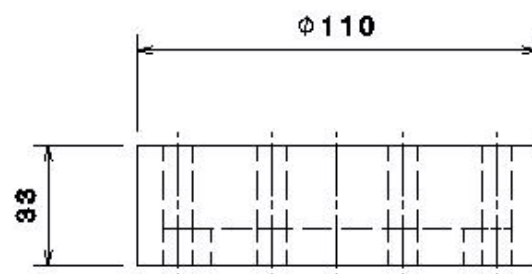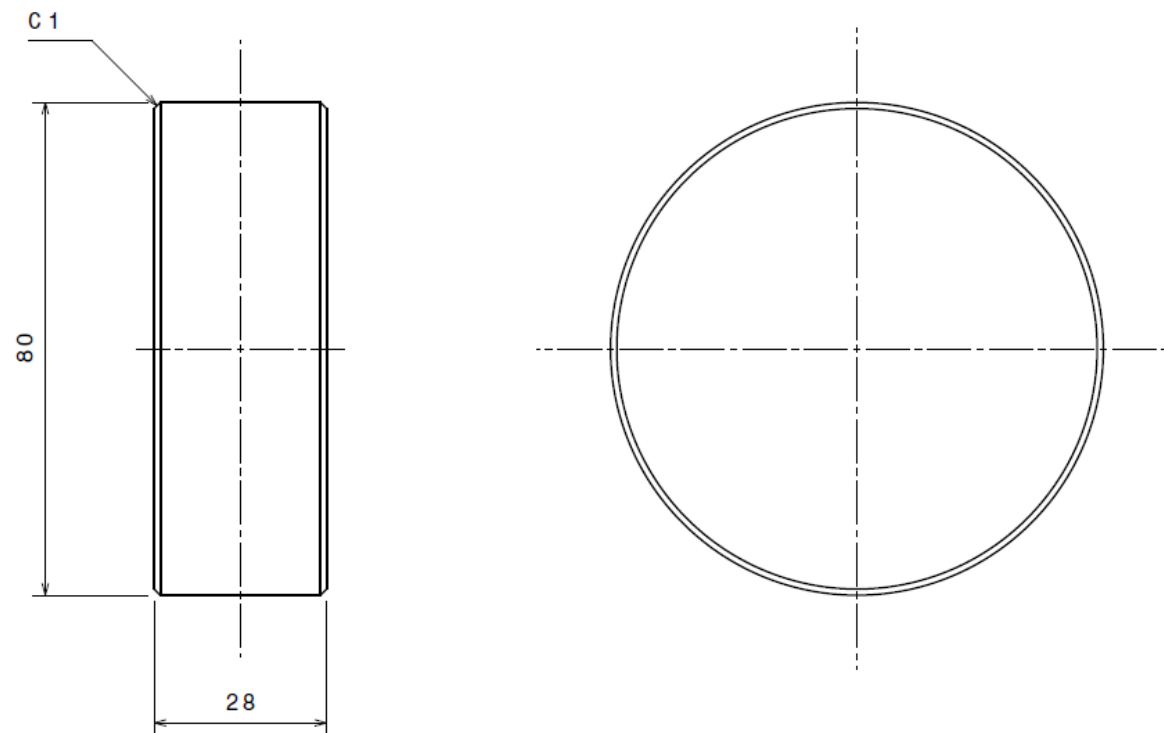
Figure 3-5 Design of optical window
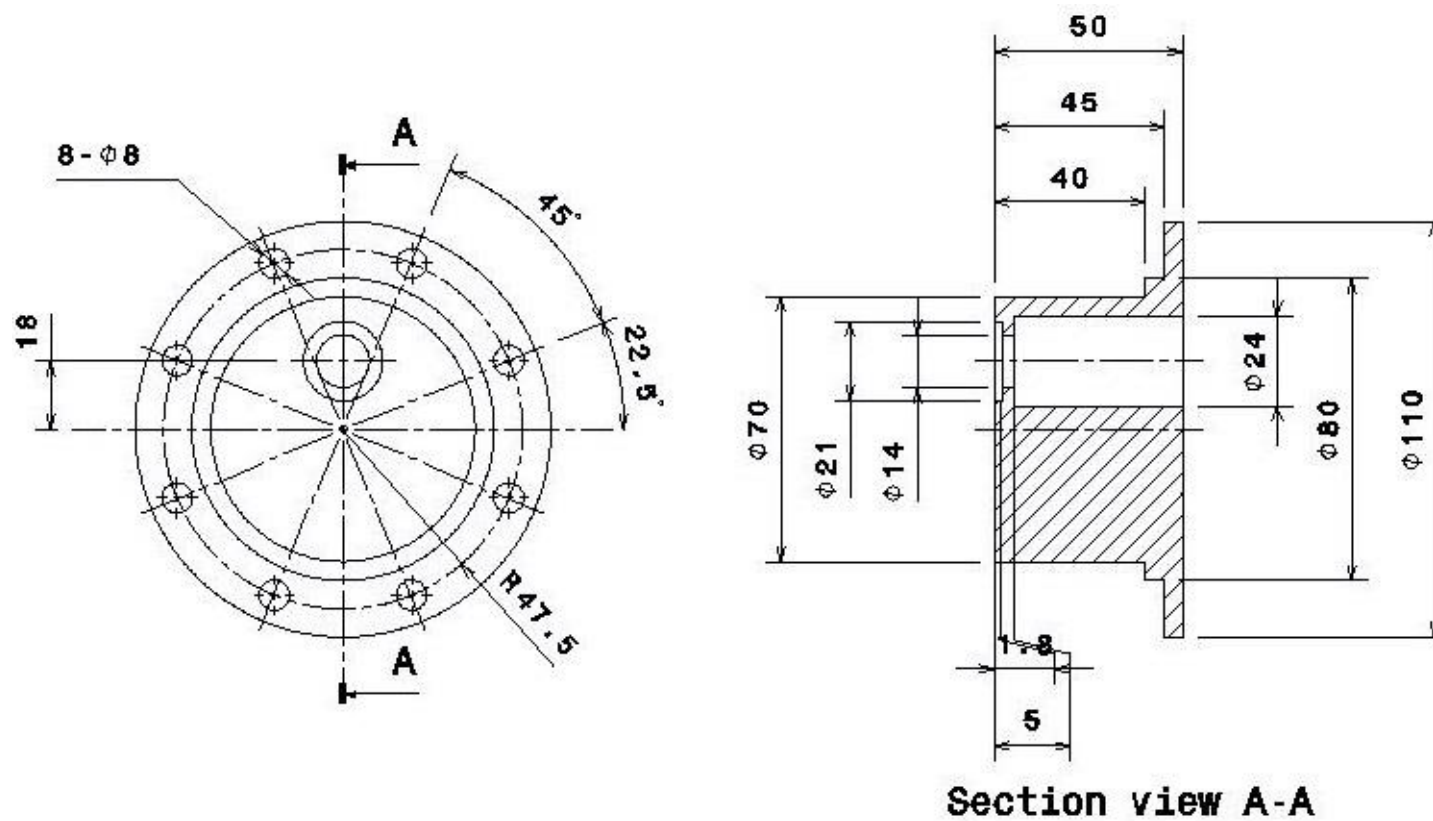
Figure 3-6 Design of spark plug port

47

No.	O-ring part number	Sugested O-ring size (mm)			Design Dimension (mm)			O-ring calculation (%)							
		Cross section	Inner diameter	Outer diameter	Groove inside (d1)	Groove Outside (d2)	Groove Depth (h)	Squeeze *(15%-30%)		Groove Fill *(Max 85%)		Elongation inside *(Max 3%)		Elongation outside *(Max 3%)	
								Min	Max	Min	Max	Min	Max	Min	Max
1	KN15 (for vacuum purpose)	5.0	15.0	25.0	14.0	27.0	4.0	16.84	23.00	66.54	80.13	0.00	0.00	0.00	0.00
2	Custom made O-ring	4.5	14.0	23.0	14.0	26.0	3.5	19.32	25.00	63.60	75.76	0.00	1.60	0.00	0.00
3		4.0	14.5	22.5	14.0	25.0	3.0	21.79	28.05	64.97	78.83	0.00	0.00	0.00	0.00
4		3.5	14.6	21.6	14.0	24.0	2.7	19.12	26.39	60.35	74.83	0.00	0.00	0.00	0.00

Table 3-1 O-ring size with the design calculation

d1 : Groove inside
d2 : Groove outside
h : Groove depth
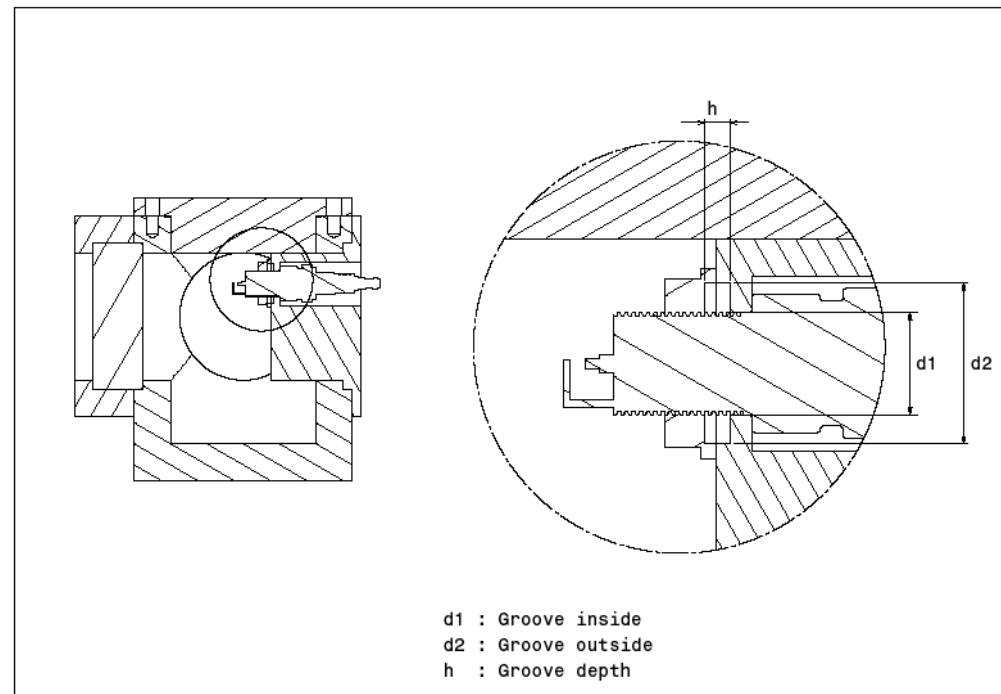
Figure 3-7 Design of groove based on the O-ring size

B

2.4

A

A

1.6

4-M3.0

Section view B-B

B

4

2.3

2.5

8.5
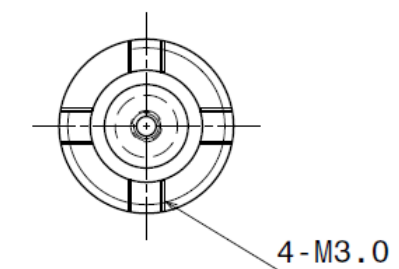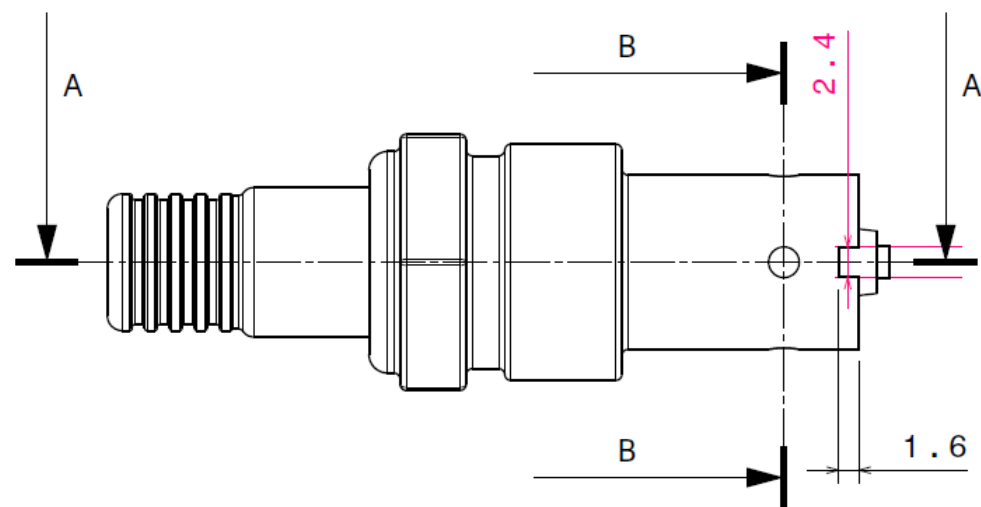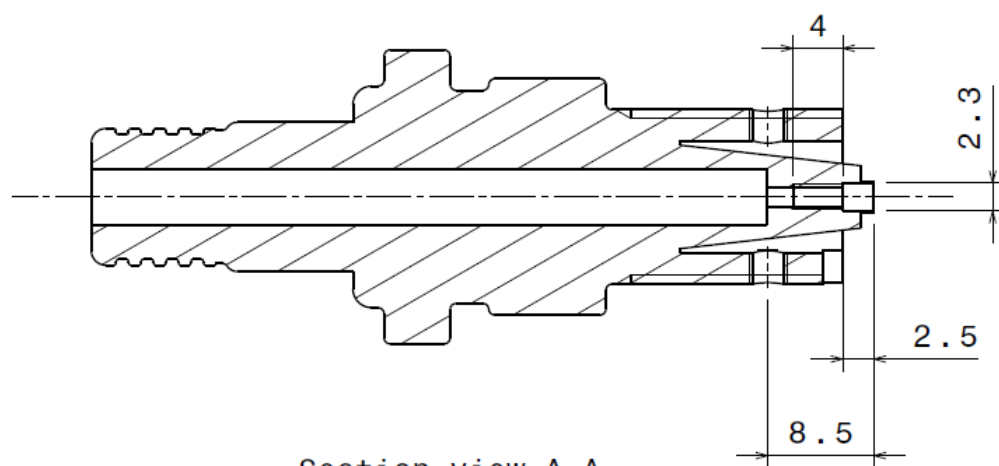
Section view A-A
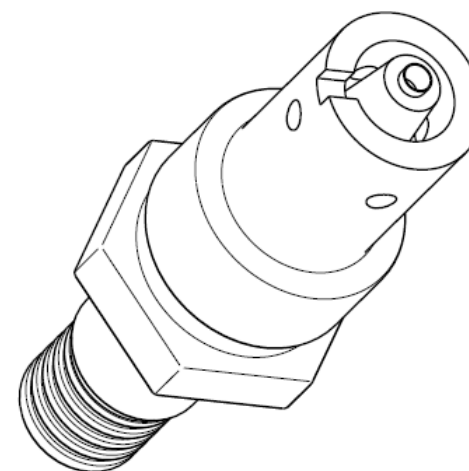
Figure 3-8 Design of spark plug sensor

3.2 Injector

Figure 3-9 shows the injector used in the experiment. The injection was achieved with an electromagnetic fuel injector with a swirl nozzle (nozzle hole diameter: 1 mm). A solenoid-driven gasoline direct injection (GDI) injector used as a fuel injector developed by Mitsubishi Electric Co. Ltd. The fuel injector was a swirl-type DI injector and the H_2 was introduced through a single orifice. The injector had a nominal cone angle of 60° and an orifice diameter of 1.0 mm. The injection signal was controlled by an electric injector driver requiring a high-voltage power source and external trigger input to control the pulse width. The injector with the jet directed toward the spark plug was used to develop the stratified combustion concept.
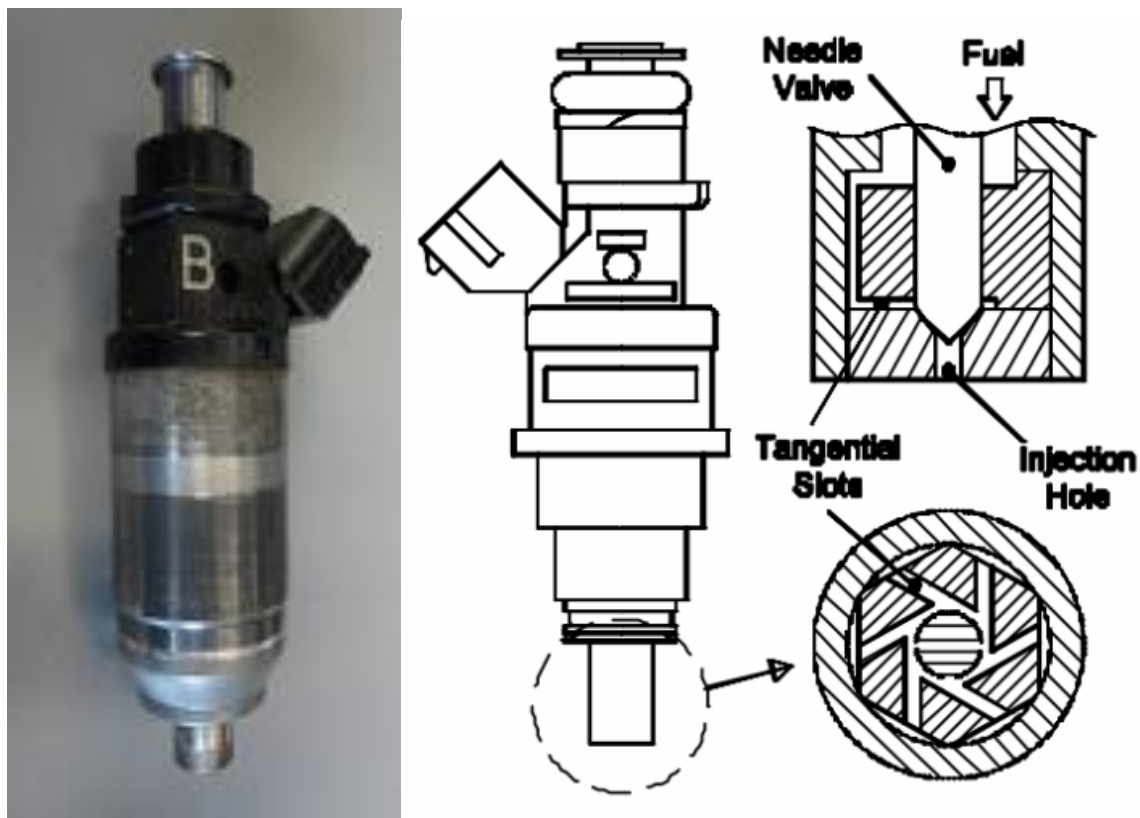
Figure 3-9 Mitsubishi DI injector

3.3 Spark plug sensor

As mentioned earlier, a SIBS technique is a best technique that can directly measure the fuel concentration inside a combustion chamber due to the usage of conventional spark plug. The spark-plug sensor developed for this experiment used a commercial spark plug used in mass-produced real-world SI engines. The electrical spark which generated between two electrodes ablated a sample material, which is vaporized, atomized, and excited. The emission characteristics can be determined from the elemental composition of the sample. Figure 3-10 shows the spark plug sensor with optical fiber for measuring the local equivalence ratio. The developed spark plug sensor was continuous improvement from previous experiment which using a 200-μm UV-grade quartz fiber, which proved practically applicable for investigating a laminar premixed flame in a CH4/air mixture[34]. Then, further improved was made by increasing the core diameter of the UV-grade quartz fiber to 600 μm to enhance its light-collecting capability. [35]. However, the capability of the spark-plug sensor should be enhanced to improve the accuracy of the data it provides. For current research, further development was made on the spark plug sensor by increasing the spark plug gap to 1.5 mm to increase the stability of spark-discharge initiation, and optical UV-grade quartz fiber with a core diameter of 1000 μm (fiber diameter 1250 μm) was used to increase the light-collecting capability of the device. The optical fiber had a numerical aperture (NA) of 0.20, which covered the area around the ground electrode. The spark-charging duration was 10 ms. The ground electrode had a small projection pointing toward the centre electrode to allow stable initiation of spark discharge. This small projection was the starting point of the ionic streamer during the breakdown and arc phases.

Takemoto performed a direct imaging of the discharge using a high-speed video camera. It was confirmed that the plasma emission is entering the light-collecting area of the fiber optics. Figure 3-11 shows time-series images of three different spark discharges with same input voltage 12 V. A fiber-optic spark plug (shown in detail in Figure 3-10) was used for the measurement. These images indicate the cycle-to-cycle fluctuations of spark images. In the first images, the ionic streamer from the ground electrode to the center electrode can be seen. These ionic streamers follow a different path in each discharge. The ground electrode of the spark-plug sensor was modified with a sharp-edged electrode for stable ionic initiation. The center electrode was a commercial electrode, which caused the ionic streamers to fluctuate in each cycle. After the breakdown and arc discharge phases, glow discharge can be

51

seen around the position where the ionic streamer arrives at the center electrode. The emission intensity from the glow discharge is weaker than the ionic streamer during the breakdown and arc phases.
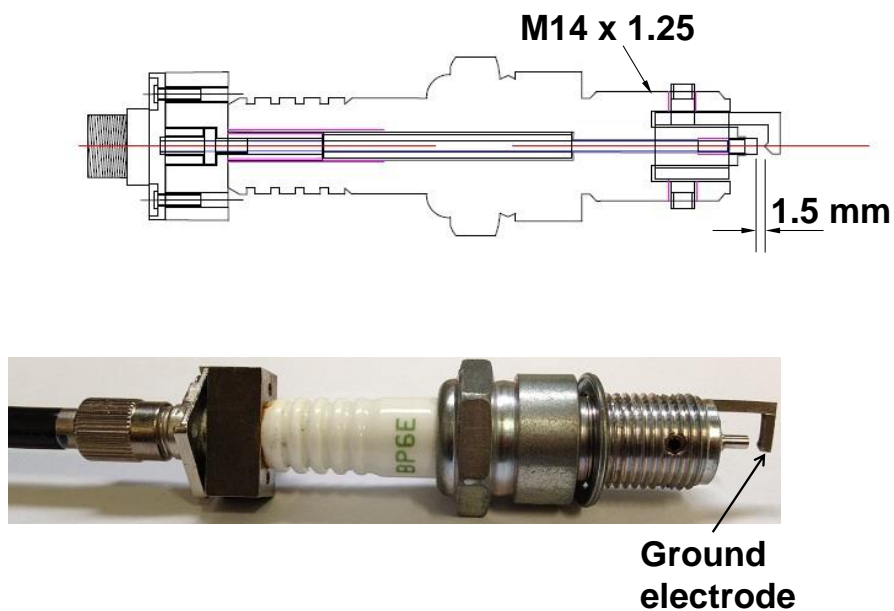
Figure 3-10 Spark plug sensor with optical fiber
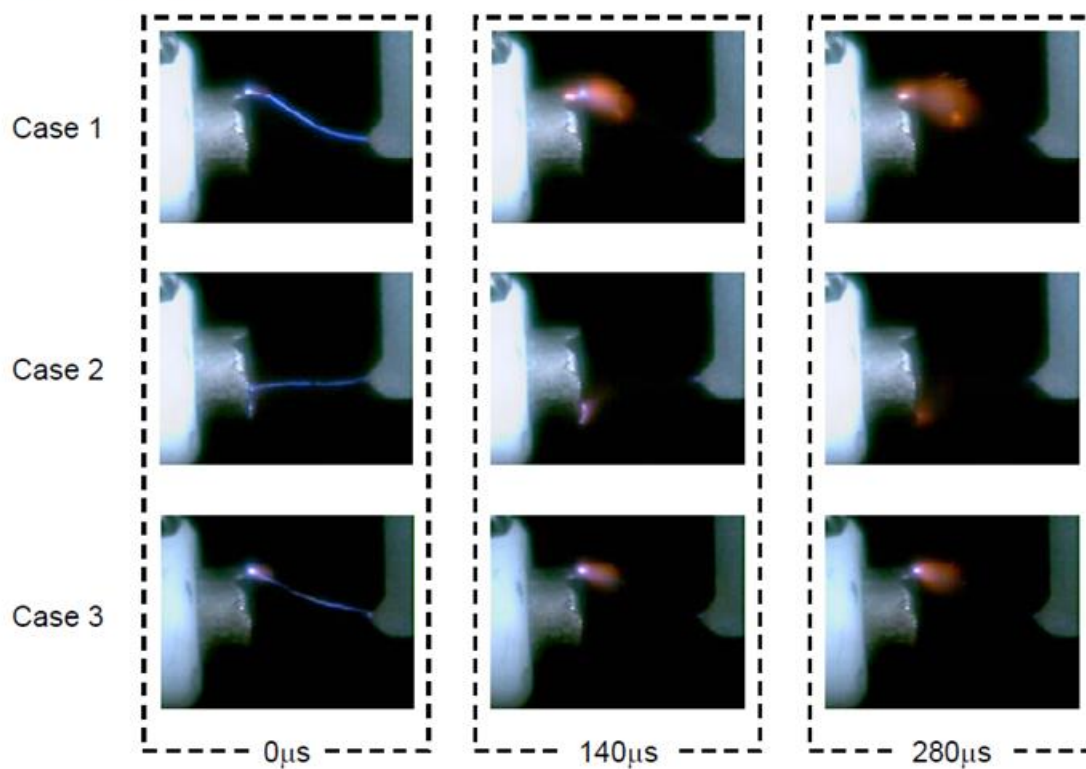
Figure 3-11 Time-series of images of spark discharges [34]

3.4 Optical access

Optical fiber consists of several elements which is core, cladding, coating buffer, strength member and outer jacket. The optic core is the light carrying element at the center. The optical fiber used to collect spectra in this research was SI type fiber which uses pure silica core. A step index is a cylindrical dielectric wave guide specified by its core and cladding refractive indices of n_1 and n_2, and the radius a (refer Figure 3-12). The product name is PV95P (STU1000H) with core size 1000 μm and core diameter 1250 μm. Details specification was shown in Table 3-2. This pure silica core fibers feature high light transmission efficiency and is suitable for a wide range of applications. The optical fiber had a numerical aperture (NA) of 0.20, which covered the area around the ground electrode. Numerical aperture (NA) of fiber optic is the measurement of the acceptance angle of an optical fiber, which is the maximum angle at which the core of the fiber will take in light that will be contained within the core. In fiber optics, numerical aperture was described as below:

$$NA = n_a \sin \theta = \sin \theta = (n_1^2 - n_2^2)^{1/2} \qquad (6)$$

Where; n_1 = refractive index of core,

n_2 = refractive index of cladding

n_a = refractive index of air (1.00).
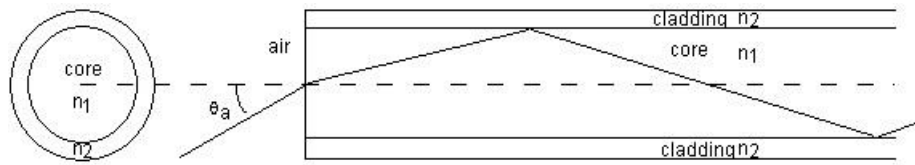
Figure 3-12 Acceptance angle of an optical fiber

Table 3-2 Specification of optical fiber

Type	Size	NA	Core diameter (μm)	Fiber diameter (μm)	Optical transmission loss (dB/km)
SI	STU1000H	0.2	1000	1250	Below 600

3.5 High-Speed camera

Figure 3-13 shows a high-speed CMOS (complimentary metal-oxide semiconductor) video camera (NAC Image Technology, GX8) that used in the experiment. NAC Memrecam GX-8 meets the imaging requirements of the most demanding applications in research and development due to its unrivalled sensitivity, speed and resolution. The NAC Memrecam GX-8 uses the latest CMOS sensor to achieve sensitivity and speeds previously unattainable. NAC Memrecam GX-8 camera system can possibly captures brilliant images at 1280 x 1024 pixels at speeds up to 2,900 fps and frame rates in excess of 600,000 fps at reduced resolutions. The camera was used to visualize the spark discharge in the constant-volume vessel when hydrogen jet was injected from top of the chamber directly to the spark plug sensor. The frame resolution was set to 208×156 pixels, and the frame rate was 60,000 frames per second. The onset of high-speed camera recording was synchronized with the spark system. Figure 3-14 shows the viewable area through the constant volume chamber window. Distance, height, position and stability of the camera are very important when adjusting the position of the camera and spark plug gap to be taken. Signs should be placed to ensure that the position of the camera and constant volume chamber is the same at all times. This is to ensure that the position of the picture to be taken is always the same for each experiment.

Figure 3-13 High-speed CMOS (complimentary metal-oxide semiconductor) video camera
(NAC Image Technology, GX8)
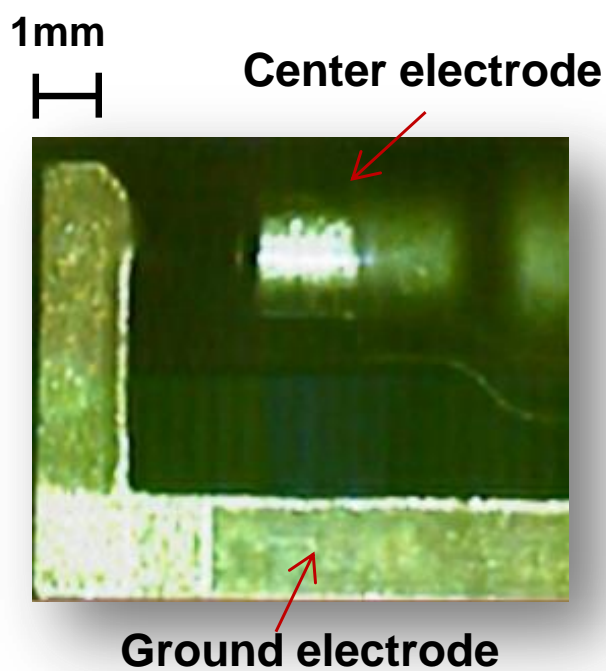
Figure 3-14 Viewable area through the constant volume chamber window

3.6 Spectrometer

A spectrometer is a devise used to measure properties of light over a specific portion of the electromagnetic spectrum. It is typically used in spectroscopic analysis to identify materials. The variable measured is most often the light's intensity but could also, for instance, be the polarization state. The independent variable is usually the wavelength of the light or a unit directly proportional to the photon energy, such as wavenumber or electron volts, which has a reciprocal relationship to wavelength. The output of a spectrophotometer is usually a graph of light intensity versus wavelength. A spectrometer is used in spectroscopy for producing spectral lines and measuring their wavelengths and intensities. There are four main parts of a spectrometer: the light source, subject, detector, and interpreter. Spectrometer is a term that is applied to instruments that operate over a very wide range of wavelengths, from gamma rays and X-rays into the far infrared. If the instrument is designed to measure the spectrum in absolute units rather than relative units, then it is typically called a spectrophotometer. The majority of spectrophotometry is used in spectral regions near the visible spectrum.

In this experiment, Ocean Optics USB2000+ spectrometer was used to measure the SIBS spectra. The spectrometer is shown in Figure 3-15. The spectrometer measured the optical emission spectrum over a range from 250 and 800 nm with a resolution of 0.3 nm and a minimum integration time of 1 ms. The spectrometer converted incoming light into voltage across a charge-coupled device (CCD), wherein each pixel of the CCD represented a pre-calibrated wavelength. Data analysis was performed using the Ocean Optics Spectra Suite software package. The USB 2000 spectrometer is a simple optical instrument based on a diffraction grating and a one-dimensional CCD detector array. The CCD array has 1×2048 pixels so the spectrum reads out as a list of 2048 data numbers.

Figure 3-16 shows a schematic of the USB 2000+ spectrometer from the Ocean Optics web page1. Light from a fiber enters the optical bench through the SMA connector (1). Light from the fiber passes through a slit (2), which acts as the entrance aperture. An optical filter (3) is installed between the slit and the aperture in the SMA connector. This filter blocks light that would be diffracted in the second- and third-orders by the grating. A collimating mirror (4) matches to the 0.22 numerical aperture (F/2.3) of the optical fiber. Light reflects from this mirror, as a collimated beam, toward the grating. The grating (5) is installed on a rotating

platform that selects wavelength range. After assembly, the grating platform is fixed to eliminate mechanical shifts or drift. A mirror (6) focuses the first-order spectra on the detector plane. A cylindrical lens (7) is fixed to the detector to focus the light from the tall slit onto the shorter detector element (14 μm × 200 μm pixels), increasing light-collection efficiency. A 2048-element Sony ILX511 linear CCD array detector (8) pixel responds to the wavelength of light that strikes it.

The linear CCD detector corresponds to the range of wavelengths on a hand held spectrophotometer. Each pixel on the CCD represents a specific wavelength of light, and the more photons absorbed, the more electrical signal generated. Therefore, the electrical signal output by the CCD at each pixel is proportional to the light intensity at each corresponding wavelength.

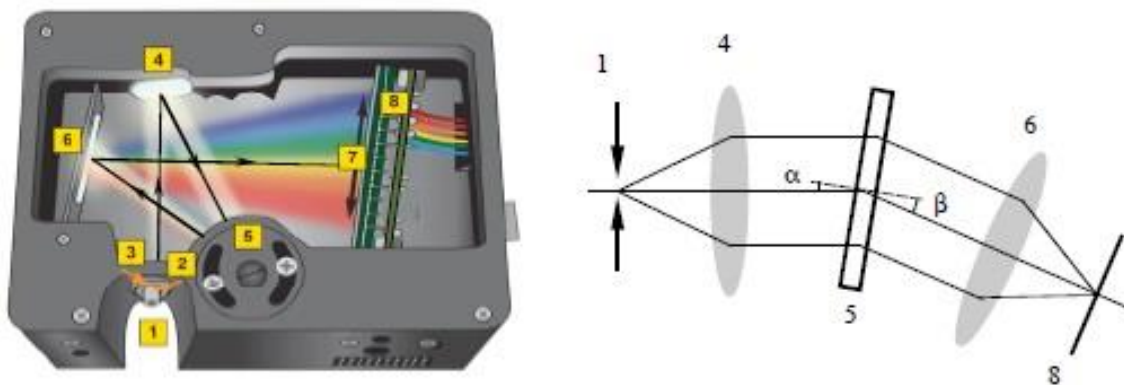Figure 3-15 The Ocean Optics USB2000+ spectrometer

Figure 3-16 Interior of USB 2000+ spectrometer

3.7 Spark discharge

Generally In spark-ignition (SI) engines, the electrical discharge produced between the spark plug electrodes by the ignition system starts the combustion process close to the end of the compression stroke. The high-temperature plasma kernel created by the spark develops into a self-sustaining and propagating flame front-a thin reaction sheet where the exothermic combustion chemical reactions occur. The function of the ignition system is to initiate this flame propagation process, in a repeatable manner cyc1e-by-cycle, over the full load and speed range of the engine at the appropriate point in the engine cycle. A spark can arc from one electrode to another when a sufficiently high voltage is applied. Ignition systems commonly used to provide this spark are: battery ignition systems where the high voltage is obtained with an ignition coil (coil ignition systems); battery systems where the spark energy is stored in a capacitor and transferred as a high-voltage pulse to the spark plug by means of a special transformer (capacitive-discharge ignition systems); and magneto ignition systems where the magneto-a rotating magnet or armature--generates the current used to produce a high-voltage pulse.

3.7.1 The stages of spark discharge

The ignition process is an important key to the operation of internal combustion engines. As a SI engines require external combustion, this is accomplished by discharging electrical energy through a spark gap. Heat transfer and gas ionization (splitting apart of gas molecules) caused by the spark discharge initiate a flame kernel. The flame kernel then grows into a flame front that spreads through the combustion chamber. A spark can arc from one plug electrode to the other only if a sufficiently high voltage is applied. In a typical spark discharge, the electrical potential across the electrode gap is increased until breakdown of the intervening mixture occurs. Ionizing streamers then propagate from one electrode to the other. The impedance of the gap decreases drastically when a streamer reaches the opposite electrode and the current through the gap increases rapidly. This stage of the discharge is called the *breakdown phase.* It is followed by the *arc phase,* where the thin cylindrical plasma expands largely due to heat conduction and diffusion and, with inflammable mixtures. The exothermic reactions which lead to a propagating flame develop. This may be followed by a *glow discharge phase* where, depending on the details of the ignition system, the energy storage device (e.g., the ignition coil) will dump its energy into the discharge circuit. Figure

3-17 shows a schematic diagram of the voltage and current of ignition sparks as function of time[112]. The actual values depend on the electrical components of the discharge circuits as indicated. The breakdown phase is characterized by very high peak values of voltage (~-10 kV) and current (=200 A), an extremely short duration (~10ns) and a cold cathode. The breakdown phase starts from the moment the gap is bridged up to the moment where thermal equilibrium between the electron temperature and the gas temperature can be assumed in the plasma channel. Naidis [113] mentioned that once the streamer has closed the gap, there are two mechanisms that have been proposed. Thermal is the first which is responsible for lowering the gas number density because of the spark channel expansion due to heating. Chemical is the other mechanism that involves the accumulation of radicals and excited molecules, which change the balance between the rates of generation and loss of electrons. For streamer-to-spark transition the chemical mechanism is dominant. The electron and gas temperatures could reach 60000 K during the breakdown phase and that the gas is highly ionized [114]. The gas molecules inside the channel are fully dissociated and ionized. The energy supplied is transferred almost without loss to the plasma, where it is stored by dissociation and ionization.

A breakdown phase always precedes arc and glow discharges: it creates the electrically conductive path between the electrodes. The arc phase voltage is low « 100 V), though the current can be as high as the external circuit permits. In contrast to the breakdown phase where the gas in the channel is fully dissociated and ionized, in the arc phase the degree of dissociation may still be high at the center of the discharge, but the degree of ionization is much lower (about 1 percent). Voltage drops at the cathode and anode electrodes are a significant fraction of the arc voltage, and the energy deposited in these electrode sheath regions, which is conducted away by the metal electrodes, is a substantial fraction of the total arc energy in Table 3-3. The arc requires a hot cathode spot, so evaporation of the cathode material occurs. The arc increases in size due primarily to heat conduction and mass diffusion. Due to these energy transfers the gas temperature in the arc is limited to about 6000 K: the temperature and degree of dissociation decrease rapidly with increasing distance from the arc axis. Currents less than 200 mA, a large electrode voltage drop at the cathode (300 to 500 V), a cold cathode, and less than 0.01 percent ionization are typical for the glow discharge. Energy losses are higher than in the arc phase, and peak equilibrium gas temperatures are about 3000 K [114]. About 0.2 mJ of energy is required to ignite a quiescent stoichiometric fuel air mixture at normal engine conditions by means of a spark. For substantially leaner and

richer mixtures, and where the mixture flows past the electrodes, an order of magnitude greater energy (~3 mJ) may be required. Conventional ignition systems deliver 30 to 50 mJ of electrical energy to the spark. Due to the physical characteristics of the discharge modes discussed above, only a fraction of the energy supplied to the spark gap is transmitted to the gas mixture. The energy balance for the breakdown, arc, and glow phases of the discharge is given in Table 3-3. Radiation losses are small throughout. The end of the breakdown phase occurs when a hot cathode spot develops, turning the discharge into an arc; heat losses to the electrodes then become substantial. The breakdown phase reaches the highest power level (~1 MW), but the energy supplied is small (0.3 to 1 mJ). The glow discharge has the lowest power level (~10 W) but the highest energy (30 to 100 mJ), due to its long discharge time.

Table 3-3 Energy distribution for breakdown, arc, and glow discharges [114]

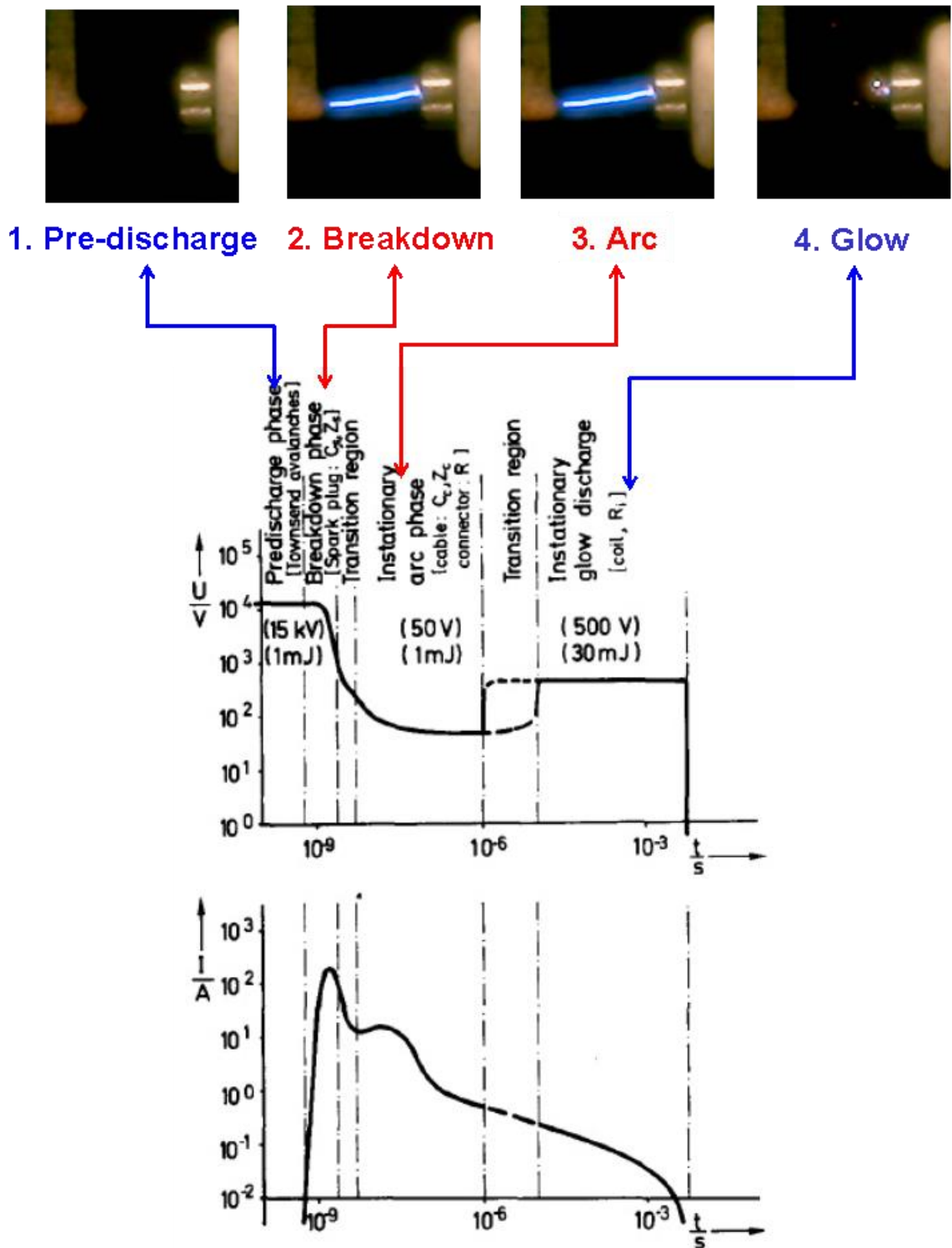|	Breakdown, %	Arc, %	Glow, %
Radiation loss	<1	5	<1
Heat loss to electrode	5	45	70
Total losses	6	50	70
Plasma energy	94	50	30

Figure 3-17 Schematic of voltage and current variation with time for conventional coil spark-ignition system. Typical values for energy and voltage in the three phases-breakdown, arc, and glow discharge [112]

3.8 Data smoothing and filtering

Smoothing and filtering are two most commonly used techniques for removing noise from a contaminated signal to help reveal important signal features and components. Typical experimental data include noise to varying degree. Noise can obscure important features like peaks, valleys, or peak widths. Noise can make it difficult to calculate signal features such as slopes, area, and peak widths. For the case of spectral data, the estimated spectrum of a time series gives the distribution of variance as a function of frequency. Depending on the purpose of analysis, some frequencies may be of greater interest than others, and it may be helpful to reduce the amplitude of variations at other frequencies by statistically filtering them out before viewing and analyzing the series. Smoothing is a form of filtering which produces a time series in which the importance of the spectral components at high frequencies is reduced. Four types of filters are discussed here: 1) moving average, 2) binomial, 3) Gaussian, and 4) windowed (Hamming method). Considerations in choosing a type of low-pass filter are the filter length and desired frequency response of the filter.

3.8.1 Moving average

An example of a symmetrical low-pass filter is the *simple moving average* filter of length N, where N is an odd integer. The individual weights of the moving average are equal to, so that the sum of the weights is $N(1/1) = 1$. The simple moving-average filter is therefore also called the running mean. The running mean has the practical advantage of simplicity over some other types of filter. The frequency response of the running mean of length N is 1.0 at the lowest frequency $= 0$, corresponding to infinite wavelength, and decreases to 0 at f $=$ 1/N , corresponding to a wavelength the same as the filter length.

3.8.2 Binomial filter

For the binomial filter, the weights are set proportional to the binomial coefficients [115]. The binomial filter can be computed by repeated convolution of the sequence of weights [0.5 0.5], corresponding to equal probabilities of success or failure for a binomial distribution. If we let $b_0 = [0.5 \ \ 0.5]$, the three-weight binomial filter is given by the convolution of

$$b_1 = \text{conv}(b_0 \ \ b_0) = [0.25 \ \ 0.50 \ \ 0.25] \tag{7}$$

63

The four-weight binomial filter, say b_2, is formed by convoluting b_1 with b_0. The five weight binomial is formed by convoluting b_2 with b_0, and so forth. The weights of an $N+1$ weight binomial filter can be computed conveniently as follows

$$c_k = \frac{N!}{k!(N-k)!} \qquad k = 0,1,.....,N \tag{8}$$

$$b_k = c_k / \sum_{k=0}^{N} c_k \tag{9}$$

The appropriate value of filter length, $N + 1$, can be computed for any desired period of 50% frequency response. The standard deviation of the binomial distribution is $\sigma_B = \sqrt{N}/2$, and the 50% response period occurs approximately at six standard deviations. Thus, considering an annual time series, if the 50% response period is p, the relationship

$$6\sigma_B = 3\sqrt{N} = p \tag{10}$$

$$N = \left(\frac{p}{3}\right)^2 \tag{11}$$

As N becomes large, the weights for the binomial filter approximate the ordinates of the Gaussian, or normal, distribution. An alternative to the binomial filter is to set the weights proportional to the probability points of a normal distribution.

3.8.3 Gaussian filter

The Gaussian filter is arrived at by setting the weights equal to the ordinates of an appropriate Gaussian, or normal, probability density function. The Gaussian filter is particularly convenient because the standard deviation of the appropriate Gaussian distribution can be specified in terms of the 50% frequency response of the filter. The appropriate Gaussian distribution therefore has standard deviation

$$\sigma_G = \frac{\lambda_{0.5}}{6} \tag{12}$$

where $\lambda_{0.5}$ is the desired wavelength at which the amplitude of frequency response is 0.5. The filter weights are obtained by sampling the pdf of the standard normal distribution at

t - values $0, \pm 1/\sigma_G, \pm 2/\sigma_G, \pm 3/\sigma_G, \ldots.$

These weights are truncated to exclude values less than 5 percent of the maximum weight, and then scaled so that the weights sum to 1.0.

3.8.4 Hamming-window filter

The binomial filter approaches a "bell shape" as filter length, N, increases, and the Gaussian filter is by definition bell shaped. Other 'bell-shaped' filters have the desired trait for low-pass filtering of a frequency response that drops steadily from 1.0 at low frequencies to zero at some frequency and remains at zero at higher frequencies. A different approach to filter design consists of applying a smoothing window, or smoothing filter, to a mathematically derived ideal digital filter. The ideal filter is specified by a cutoff frequency, f_o, defined such that the amplitude of frequency response is 1 for all frequencies less than f_0 and 0 for all frequencies greater than or equal to f_0 . Such a frequency response is called a brick-wall response. Recall that the frequency response of a filter is the Fourier transform of the impulse response of the filter, and that the impulse response of a symmetrical digital filter is proportional to the filter itself. The ideal filter is accordingly computed as the inverse Fourier transform of the brick-wall frequency response. The ideal filter as so defined is not implementable because its impulse response is infinite and non-causal. To create a finite-duration impulse response, the ideal filter is truncated by applying a "window."

A useful window for this purpose is the Hamming window, or raised cosine window [116]. The Hamming window weights are

$$w_i = (0.54 - 0.46 \cos[2\pi i/(N-1)]/\sum_{i=0}^{N-1} w_i \qquad 0 \le i \le (N-1) \qquad (13)$$

where N is the length of the window, or filter. N includes the central weight and the weights on either side of it. For example, a 5-weight Hamming-window filter1, with $N = 5$ and central weight w_2, has weights [0.0357 0.2411 0.4464 0.2411 0.0357]. The Hamming window

applied to the ideal low-pass filter yields an implementable filter that in a sense is ideal given the specified constraint on the filter length.

The filter design problem in the windowed method is reduced to 1) specifying a desired cutoff frequency, and 2) specifying a desired filter length. As the filter length is increased, the algorithm comes closer to the objective of an "ideal" filter in terms of frequency response, but more data is lost off the ends of the series because of the large number of weights. The filter weights sum to 1, but for longer filter lengths some weights can be negative. This is a necessary consequence of the mathematics, but can be disturbing for practical interpretation.

3.9   Injection quantity test

The injection quantity test was performed using constant volume chamber by consider atmosphere pressure and injection pressure as a parameter. Figure 3-18 shows a schematic of the setup used for injection quantity test. The test was conducted in a constant volume vessel. The constant volume vessel has a cylindrical shape and a volume of 675cm3 (diameter: 80mm, Length: 125mm). The injector was installed on the top of the chamber using Mitsubishi swirl injector as mentioned in section 3.2. The injection was achieved with an electromagnetic fuel injector with a swirl nozzle (nozzle hole diameter: 1 mm). The injector had a nominal cone angle of 60° and an orifice diameter of 1.0 mm. The injection signal was controlled by an electric injector driver requiring a high-voltage power source and external trigger input to control the pulse width. Bourdon tube pressure gauge was used to measure the pressure inside the constant volume chamber for each time of hydrogen injection timing. As of next experiment is to measure the hydrogen fuel concentration at different ambient pressure, for injection quantity test, we conduct the experiment in three different ambient pressure which is 0.5 MPa, 1.0 MPa and 1.5 MPa. For injection quantity test for the ambient pressure of 0.5 MPa, nitrogen was transferred in the constant volume chamber until the bourdon tube pressure gauge shows 0.5MPa. The Hydrogen with feed pressure of 5MPa was then injected inside the constant volume chamber. The injection duration of hydrogen jet was set from 2ms to 36ms for each injection time. The injection was set 3 times for each injection condition. The experiment was conducted one at a time to make sure the stable result can be obtained. The same step was repeated for ambient pressure 1.0 MPa and 1.5 MPa. From this experiment, the graph for amount of injection versus hydrogen injection duration can be drawn as shown

in Figure 3-19. From the results of injection amount versus hydrogen injection duration, the relation between equivalence ratio and hydrogen injection duration can be calculated and the graph can be seen at Figure 3-20.

3.9.1 Injection quantity test calculation

The experiments above were conducted by transferring the hydrogen and nitrogen to the constant volume chamber while considering nitrogen gas instead of air: non combustion condition. When calculation the hydrogen injection quantity with the relation of injection amount and equivalence ratio, we consider the oxygen should be include so that the right calculation for the equivalence ratio can be made. The ideal gas law was used to calculate the amount of mass injected into the chamber. The mass injected into the chamber, Δm in a single injection is given by:

$$\Delta m = \frac{(P_2 - P_1)V}{RT} \tag{14}$$

Where P_2 is the pressure after injection and P_1 is the initial pressure. The approximated average mass flow rate is then calculated by dividing the injected mass, Δm, by the injection duration.

Consider the structure of gas used in this experiment as below box.

| H2 | N2 + O2 |

In most application, oxygen comes from surrounding air that contains 20.95% O_2 and 79.05% N_2. Therefore, the volume ratio for N_2 and O_2 is 79.05: 20.95. From the ratio of N_2: O_2, volume of H_2 can be found.

O_2 that need to burn the H_2 is when the equivalence ratio is 1 ($\phi = 1$).

$2H_2 + O_2 \rightarrow 2H_2O$
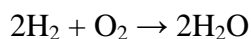
from above chemical reaction equation, two H_2 need to burn one O_2. Therefore, volume for H_2 is 2 times of O_2 which is 41.9. The volume ratio for H_2, N_2 and O_2 can be simplified as below:

$H_2 : N_2 : O_2 = 41.9 : 79.05 : 20.95$

The values are based on the condition of gas at 20°C and atmospheric pressure of 101.325 kPa. When calculate the equivalence ratio based on the ΔP, the atmospheric pressure should be change related to measured ambient pressure.

Example:

Consider the total air inside the constant volume chamber is $N_2 + O_2 = 79.05 + 20.95 = 100$,

Ratio of pressure in the constant volume chamber for H_2 and N_2 is 41.9 kPa : 100 kPa,

In case of the ambient pressure of N_2 in constant volume chamber is 500 kPa, the ambient pressure need to consider when calculating the equivalence ratio is 209.5kPa. The relation between equivalence ratio and hydrogen injection duration can be calculated and the graph can be seen at Figure 3-20.
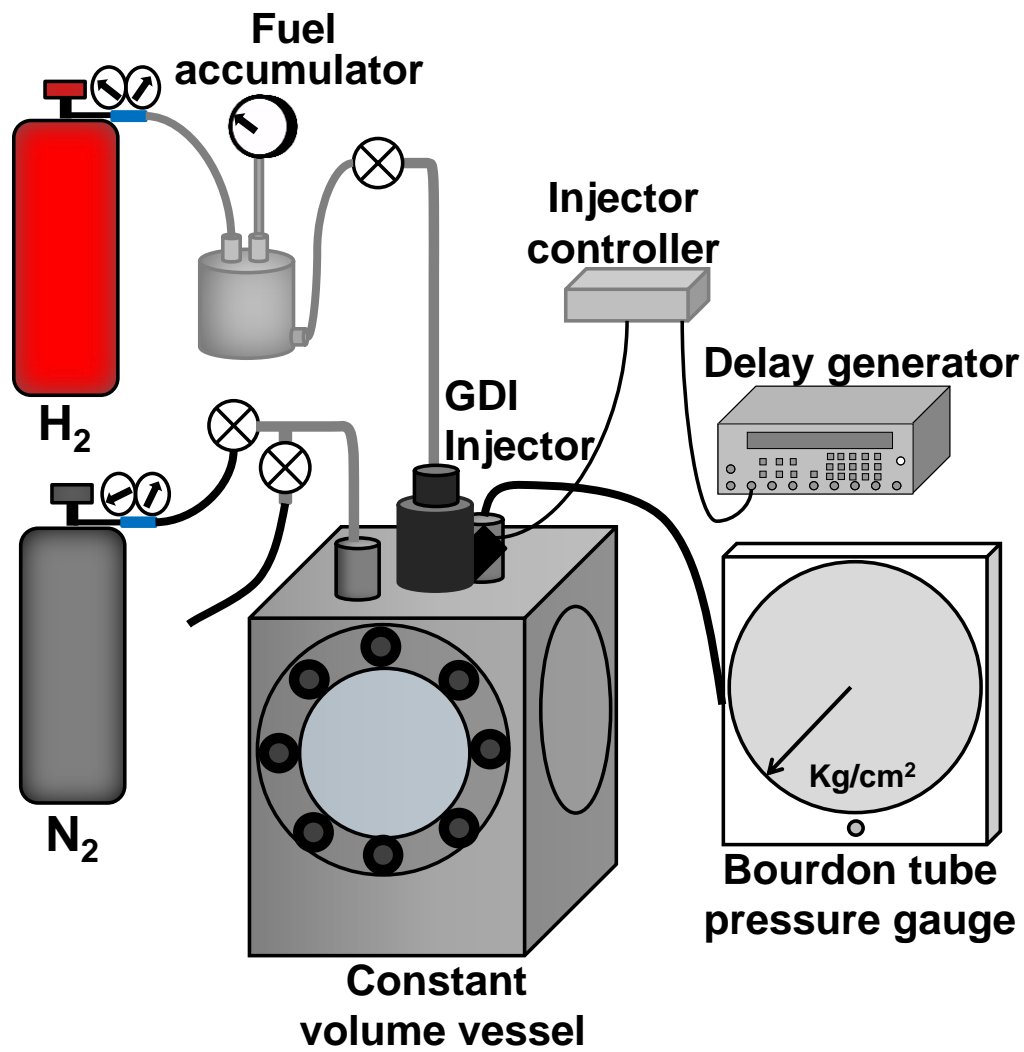
Figure 3-18 Schematic of the experimental apparatus for the hydrogen injection quantity test
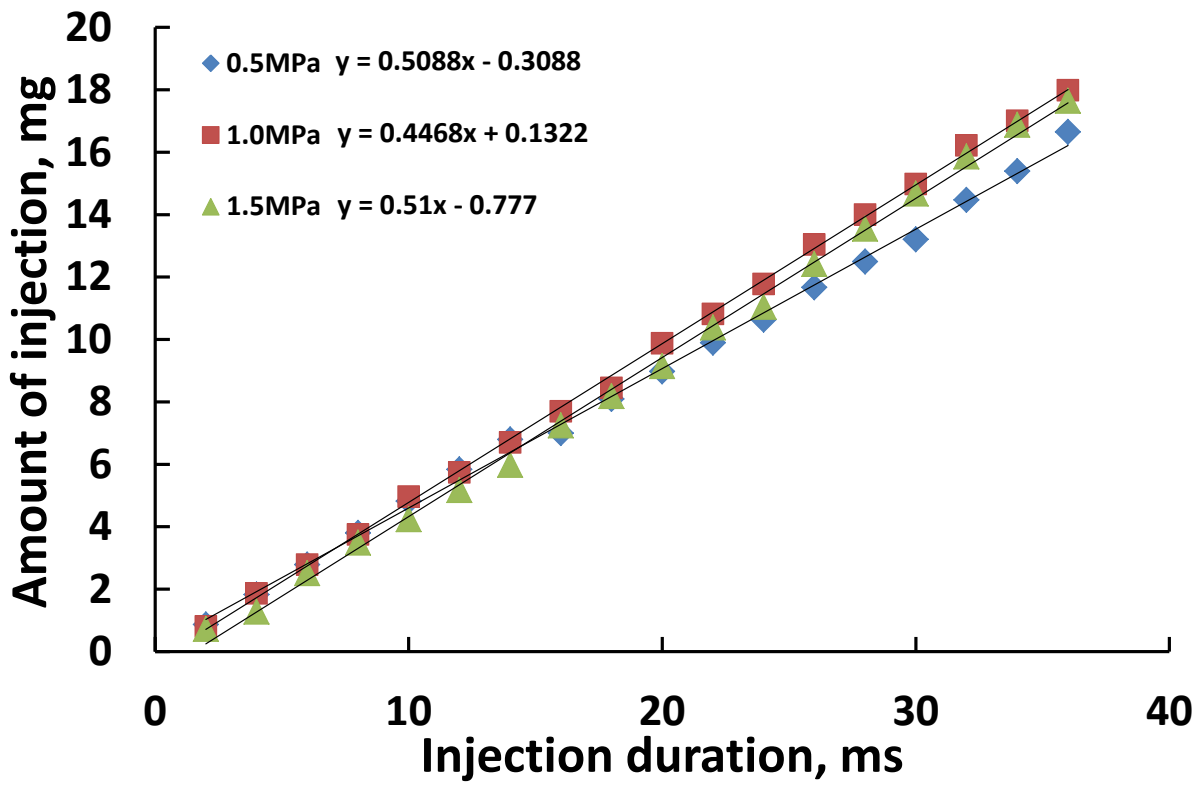
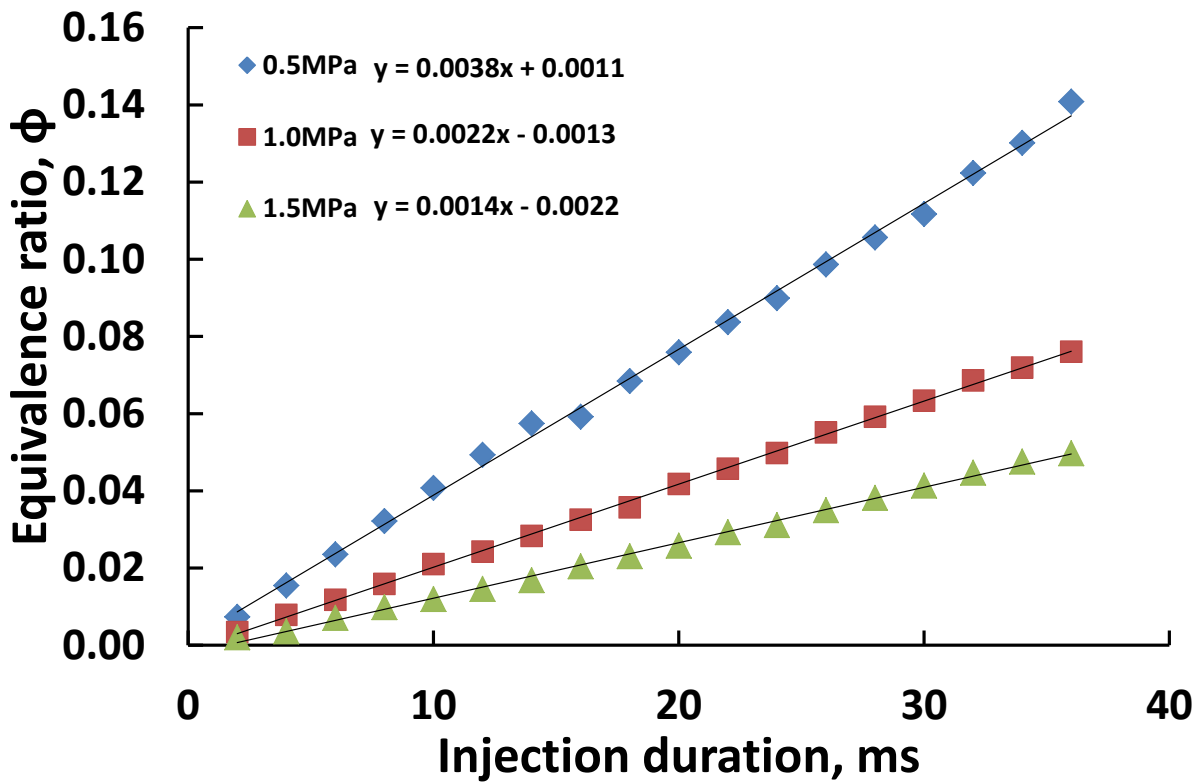Figure 3-19 Relation between injection duration and amount of injection

Figure 3-20 Relation between injection duration and equivalence ratio

3.10 Calibration curve

In analytical chemistry, a calibration curve is a general method for determining the concentration of a substance in an unknown sample by comparing the unknown to a set of standard samples of known concentration. It is a graph generated by experimental means, with the concentration of solution plotted on the x-axis and the observable variable for example, the solution's absorbance plotted on the y-axis. The curve is constructed by measuring the concentration and absorbance of several prepared solutions, called calibration standards. Once the curve has been plotted, the concentration of the unknown solution can be determined by placing it on the curve based on its absorbance or other observable variable.

Chemical solutions absorb different amounts of light based on their concentration. This fact is quantified in an equation known as Beer's law, which shows a linear relation between a solution's light absorbance and its concentration. Researchers can measure the absorbance of a solution using a laboratory instrument called a spectrophotometer whereas in this research the USB2000+ was used. This process as a whole is called spectrophotometry. Spectrophotometry can be useful in determining the concentration of an unknown solution. In this experiment, hydrogen/nitrogen mixture was made in various equivalence ratios and was determined by using a spectrometer to plot a calibration curve.

The experimentally determined absorbance values are plotted on a graph against the known concentration of each calibration standard. A set of points is created, which in the case of absorbance should be roughly linear due to Beer's law. A line is drawn to connect these data points, forming the calibration curve. In almost every case, the data points will not be mathematically exact, so the line should be drawn to intercept the maximum number of points it is a line of best fit. Although the relationship of absorbance to concentration is linear, this is not always true for other experimentally determined variables, and occasionally curves must be employed to describe the relationship. At this stage, the unknown solution can be analyzed. The absorbance of the sample is measured by spectrometer. Since this sample is being measured against several standards that containing the same compound, its absorbance and concentration must fall somewhere along the calibration curve for that compound. This means that once the solution's absorbance is known, its concentration can be deduced mathematically or graphically.

A horizontal line can be drawn from the unknown solution's y-value which is its absorbance, which has just been measured. The point at which the line crosses the calibration curve will indicate the x-value which is the concentration. A vertical line, drawn downwards from this point, gives the concentration of the unknown solution. The equation for the line of the calibration curve can also be used to mathematically determine the solution's concentration.

3.11 Calibration standards preparation

The SIBS method, as any other analytical technique, requires calibration to obtain optimum results in quantitative analysis. Calibration standards with different concentrations should be prepared. Here, the standard concentrations should cover the range of concentrations encountered during the analysis of test samples and be evenly spaced across the range. The plot of the data should be inspected for possible outliers and points of influence. In general, an outlier is a result which is significantly different from the rest of the data set. In the case of calibration, an outlier would appear as a point which is well removed from the other calibrations points. A point of influence is a calibration point which has a disproportionate effect on the position of the regression line. A point of influence may be an outlier, but may also be caused by poor experimental design. Ideally, the calibration range should be established so that the majority of the test sample concentrations fall towards the center of the range. This is the area of the calibration range where the uncertainty associated with predicted concentrations is at its minimum. It is also useful to make at least duplicate measurements at each concentration level, particularly at the method validation stage, as it allows the precision of the calibration process to be evaluated at each concentration level. The replicates should ideally be independent. Making replicate measurements on the same calibration standard gives only partial information about the calibration variability, as it only covers the precision of the instrument used to make the measurements, and does not include the preparation of the standards.

3.12 Fuel-Air Mixture Calculation Method

As with other quantitative analytical techniques, the SIBS technique requires calibration to obtain optimum results. The correlation between the fuel/air mixing (hydrogen/nitrogen) ratio and atomic emission was determined, and the post-processing procedure was calibrated. Nitrogen dilution was utilized to ensure safe use of hydrogen,

which has a higher burning velocity. Hydrogen/nitrogen gas mixtures were made for a range of equivalence ratios (ϕ=0.3 to 5.0) via nitrogen dilution (32% to 89%). The experiments were conducted by transferring the hydrogen/nitrogen mixture to the constant-volume chamber without combustion, with the nitrogen gas serving in place of air. The mixtures were transferred under a pressure of 0.5 MPa at room temperature. The SIBS sensor then initiated the spark, and the local concentration was measured. The experiment was performed 100 times under each set of conditions, and the resulting data were averaged.

In order to calculate the mixture amount of the fuel, oxygen and nitrogen conveniently, the following method is used:

Assuming the formula of the fuel is CmHn and the ratio of nitrogen to oxygen is 79/21. The equivalent ratio Φ of C_mH_n when the mixed and burning with N2/O2 occurred is shown as below equation:

$$\phi \cdot C_mH_n + \left(\frac{n}{4} + m\right)\left(O_2 + \frac{79}{21}N_2\right)$$
$$\rightarrow \phi \cdot mCO_2 + \phi \cdot \frac{n}{2}H_2O + (1 - \phi)\left(\frac{n}{4} + m\right)O_2 + \left(\frac{n}{4} + m\right)\frac{79}{21}N_2 \tag{15}$$

From equation (12), the molar fraction of the fuel and the N_2/O_2 mixture can be shown as follows:

$$[C_mH_n] : [O_2] = \phi : \left(\frac{n}{4} + m\right)$$

$$[C_mH_n] : \left[O_2 + \frac{79}{21}N_2\right] = \phi : \frac{100}{21}\left(\frac{n}{4} + m\right)$$

The total relative pressure of the mixture can be set as P(kgf/cm^2) and the atmospheric pressure can be recorded as *P0*(kPa). Assumed the total pressure is 98.0665*P(kgf/cm2) + P0(kPa)*. Therefore, the partial pressure of the fuel *Pf* and relative pressure *P* is shown as below equation. The temperature change when the gas is filled is not considered.

$$P_f = (98.0665P + P_0) \times \frac{\phi}{\phi + \frac{100}{21}\left(\frac{n}{4} + m\right)}$$

$$= (98.0665P + P_0) \times \frac{4\phi}{4\phi + \frac{100}{21}(n + 4m)} \ [kPa] \tag{16}$$

$$P = \left\{ P_f \frac{4\phi + \frac{100}{21}(n + 4m)}{4\phi} - P_0 \right\} \frac{1}{98.0665} \ [kgf/cm^2] \tag{17}$$

To decrease the effect of temperature change, gradually fill in the gas into mixture cylinder.

3.13 Summary

This chapter discussed about the apparatus and the methodology used in this study to measure the local fuel concentration of the hydrogen jet at different ambient pressures of nitrogen. A constant-volume vessel equipped with a SIBS sensor was used, and a swirl-type direct-injection (DI) injector with a single orifice was installed at the top of the vessel. The local fuel concentration of the hydrogen jet was measured at several locations, using a SIBS sensor. The SIBS sensor, which was developed using a commercially available spark plug with an optical fiber installed at the centre. An Ocean Optics USB2000+ spectrometer was used to analyse the light obtained from the optical fiber. A high-speed camera was used to visualize spark discharge fluctuations, and hydrogen jet concentration measurements were conducted simultaneously. Four types of filters are discussed: 1) moving average, 2) binomial, 3) Gaussian, and 4) windowed (Hamming method). The quantity test experiment was discussed whereas the results of injection amount versus hydrogen injection duration, the relation between equivalence ratio and hydrogen injection duration can be calculated

4 Calibration of Spark Induced Breakdown Spectroscopy (SIBS)
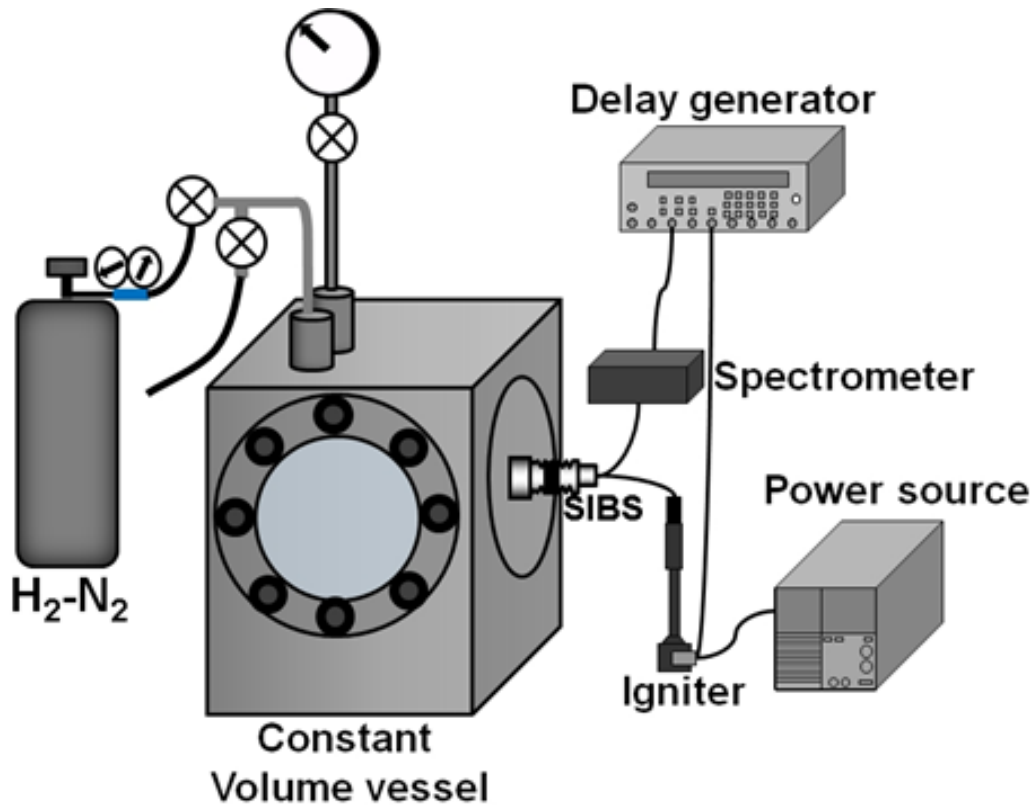
4.1 Experimental setup

Figure 4-1 Schematic of the setup for the calibration experiment with the spark-induced breakdown spectroscopy sensor

Figure 4-1 shows a schematic of the setup used for the calibration experiment with the spark-induced breakdown spectroscopy (SIBS) sensor. The experimental apparatus consisted of three main parts: 1) the spark system with the spark plug and igniter, 2) the acquisition equipment, and 3) the synchronization system. The experimental was conducted using constant volume chamber equipped with SIBS sensor. The constant volume chamber had a volume of 675 cm^3 with rectangular shape. One wall of the chamber was designed to hold the spark plug sensor, and others walls of the chamber were fitted with circular quartz windows to allow optical access. The spark plug sensor developed for this experiment used a commercial spark plug used in mass-produced real-world SI engines. The spark-plug gap was 1.5 mm to increase the stability of spark-discharge initiation, and optical UV-grade quartz fiber with a core diameter of 1000 µm (fiber diameter 1250 µm) was used to increase the light-collecting capability of the device. The optical fiber had a numerical aperture (NA) of 0.20, which

covered the area around the ground electrode. The spark-charging duration was 10 ms. The ground electrode had a small projection pointing toward the centre electrode to allow stable initiation of spark discharge. This small projection was the starting point of the ionic streamer during the breakdown and arc phases.

4.2 Experimental condition and procedure

As with other quantitative analytical techniques, the SIBS technique requires calibration to obtain optimum results. The correlation between the fuel/air mixing (hydrogen/nitrogen) ratio and atomic emission was determined, and the post-processing procedure was calibrated. Nitrogen dilution was utilized to ensure safe use of hydrogen, which has a higher burning velocity. Hydrogen/nitrogen gas mixtures were made for a range of equivalence ratios (ϕ=0.3 to 5.0) via nitrogen dilution (32% to 89%) as shown in Table 4-1. The experiments were conducted by transferring the hydrogen/nitrogen mixture to the constant-volume chamber without combustion, with the nitrogen gas serving in place of air. The mixtures were transferred under a pressure of 0.5 MPa at room temperature. The SIBS sensor then initiated the spark, and the local concentration was measured. The experiment was performed 100 times under each set of conditions, and the resulting data were averaged.

Table 4-1 Calibration standards of hydrogen and nitrogen with equivalence ratio

No.	H2-N2 amount (%)		Equivalence ratio (ϕ)
	H_2	N_2	
1	10.8	89.2000	0.289
2	16.7000	83.3000	0.478
3	23.8000	76.2000	0.745
4	30.1000	69.9000	1.028
5	46.6000	53.4000	2.083
6	55.7000	44.3000	3.001
7	68.1000	31.9000	5.095

4.3 Background correction method

When measuring the emission intensity ratio using the two elements and pure emission in a certain element, it is necessary to accurately determine the peak intensity for each element. In order to calculate the element density of integrated peak intensities, the processing method of the background is important for an accurate quantification quantitative analysis of the measured emission spectra. Pure emission in a certain elements has a spread of specific elements, called distributed spectrum at a particular wavelength. The emission of each overlap near the boundary is clarified the elements together with similar wavelengths, and is detected as a continuous spectrum as shown in Figure 4-2 and the emission is duplicated as shown as Figure 4-3. The background processing means that, when determining the peak intensity at a particular element from the continuous spectrum, it is necessary to consider the effect of overlapping of the emission. It is caused by the emission energy generated in the element during before the escape from the surface and loses energy to receive the inelastic scattering by another atom.
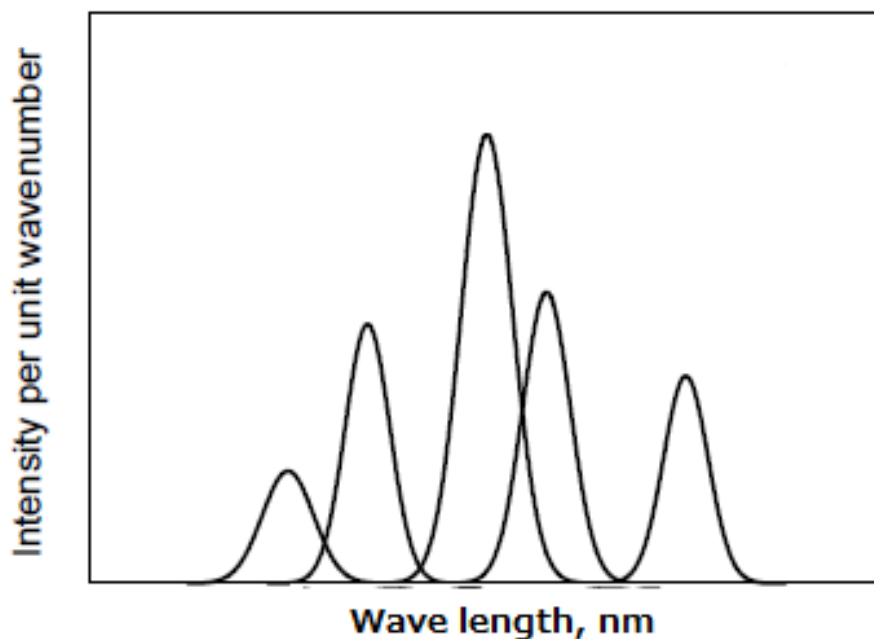

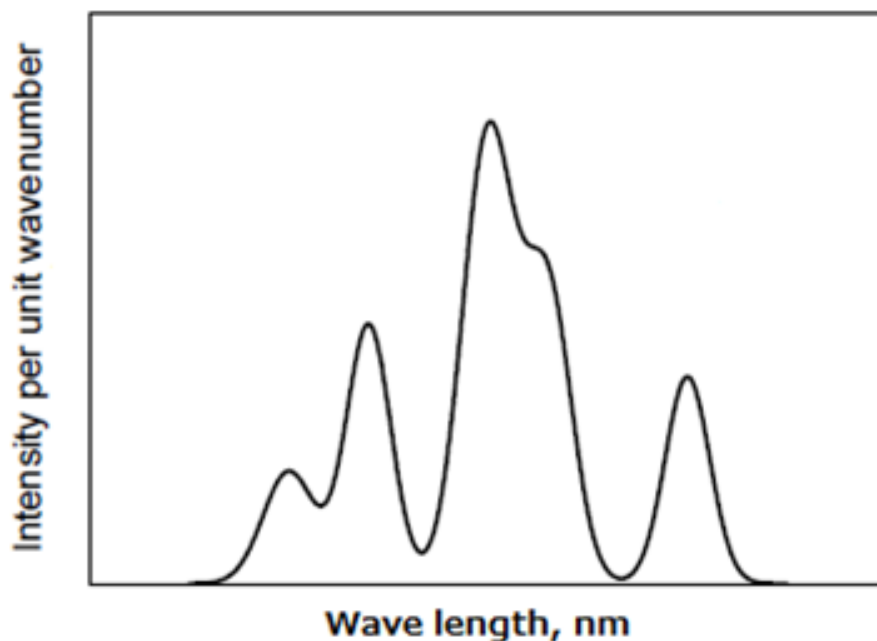Figure 4-2 Overlapping distribution of spectrum in each element

Figure 4-3 Duplicated spectrum

Quantifying the intensity of peaks in emission intensity data requires the proper modeling of the background signal. There are various background types as below list that are employed on a case-by-case basis.

1. linear,
2. Tougaard,
3. Shirley-Sherwood,
4. exponential
5. polynomial,

The traditional (or *static*) peak-fitting methodology has the following distinguishable characteristics:

1. One of the background types is chosen depending on the shape of the spectrum.
2. The background is forced to pass through two user-defined points, one at each side of the peaks.
3. The background is first subtracted from the original data and then the modified background less spectrum is peak-fitted.

In this study, we decided to perform background processing using the improved version Shirley method. The features in the analysis of each method are shown as below.

4.3.1 Linear technique

Figure 4-4 shows the example of analysis by liner method. For analyzing the wavelength, two specific wavelengths was selected by consider the influence of the spectral distribution. Draw a straight line between the emission intensity that was selected and remove background region below the line. Since this method is not necessary to use such formulas, the method is a method which can perform background processing most easily. However, the error is high because it does not consider almost duplication of the emission in the analysis of two elements with similar wavelength.
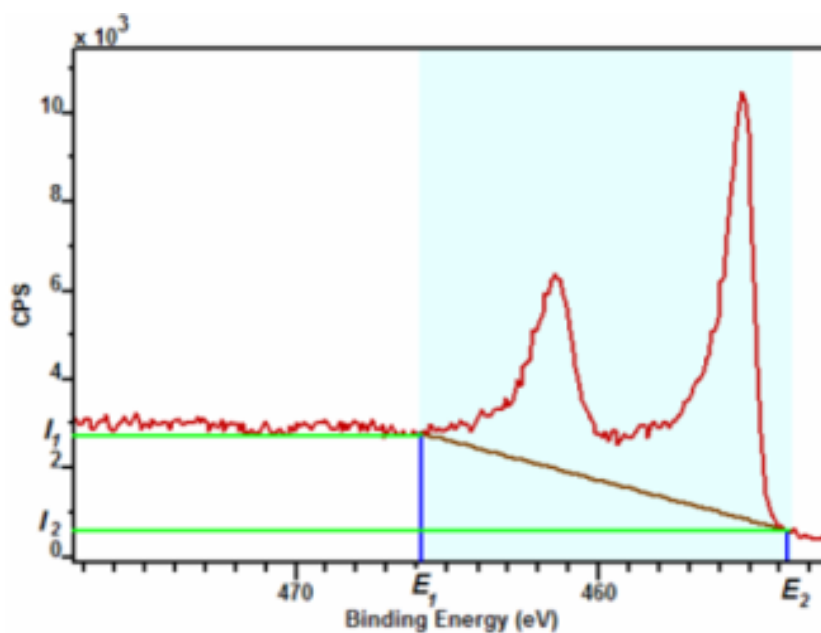

Figure 4-4 Example of the analysis using liner method

4.3.2 Tougaard method

Figure 4-5 shows the example of analysis by Tougaard method. For analyzing the wavelength, two specific wavelengths was selected by consider the influence of the spectral distribution. In this method, the effects of removal the background consider the multiple scattering effects and three-dimensional structural model of the elements. The analysis method is based on the physical basis and has been considered the probability that electrons (spatial distribution of atoms) generated the distribution of light and electron energy loss of the element-specific loses some of the energy. In this method, both ends of the peak values are found natural three-dimensional structure model and energy loss probability of the element. However, obtaining an energy loss probability of all elements of the measurement

79

target is not easy. It is not possible to know in advance the three-dimensional structure element more details.
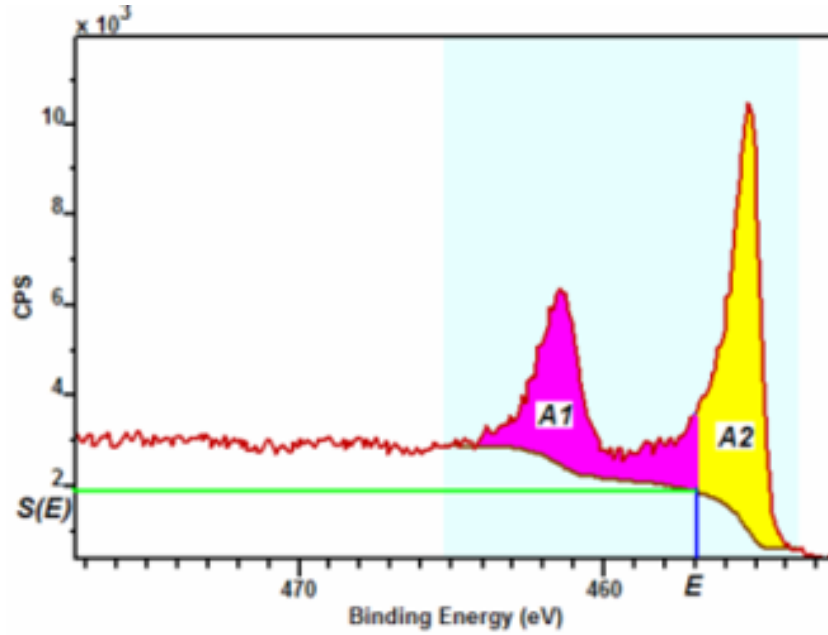

Figure 4-5 Example of the analysis using Tougaard method

4.3.3 Shirley method

Figure 4-6 shows the example of analysis by Shirley method. Similar with another method, for analyzing the wavelength, two specific wavelengths was selected by consider the influence of the spectral distribution. In Shirley method, selected points between emission intensity use below equation

$$B(x) = \frac{(a - b)Q}{(P + Q)} + b \tag{18}$$

The background curve based on the Shirley method is calculated by the following way: For the calculation of the background curve shown in Figure 4-7, we assume that there are n points between the end points of (q_1, B_1) and (q_2, B_2), and let the background and net peak at the i-th point in the j-th approximation be $BG_j(i)$ and $N_j(i)$, respectively. Then

$N_j(i) = y_i - BG_j(i)$. By using the Shirley`s formula,

$$BG_i(i) = \frac{(B_1 - B_2)Q_j(i)}{P_j(i) + Q_j(i)} + B_1 \tag{19}$$

where $P_j(i)$ and $Q_j(i)$ are the left and right side of the net peak areas at *i-th* point in the *j-th*

approximation, and they are expected as follows(assuming the step width being 1):

$$P_j(i) = \sum_{l=1}^{i} N_j(l) - 0.5\big(N_j(1) + N_j(i)\big) \tag{20}$$

and,

$$Q_j(i) = \sum_{l=i}^{n} N_j(l) - 0.5\big(N_j(i) + N_j(n)\big) \tag{21}$$

For the 0-th approximation, the initial background curve BG_0 (*i*) is taken as the straight line connecting the 2 points (q_1, B_1) and (q_2, B_2). This iterative calculation continues until the following convergence condition is satisfied:

$$|S\_j - S\_(j-1)|/S\_j < 0.001 \quad \text{where,} \quad S_j = P_j(i) + Q_j(i) \tag{22}$$
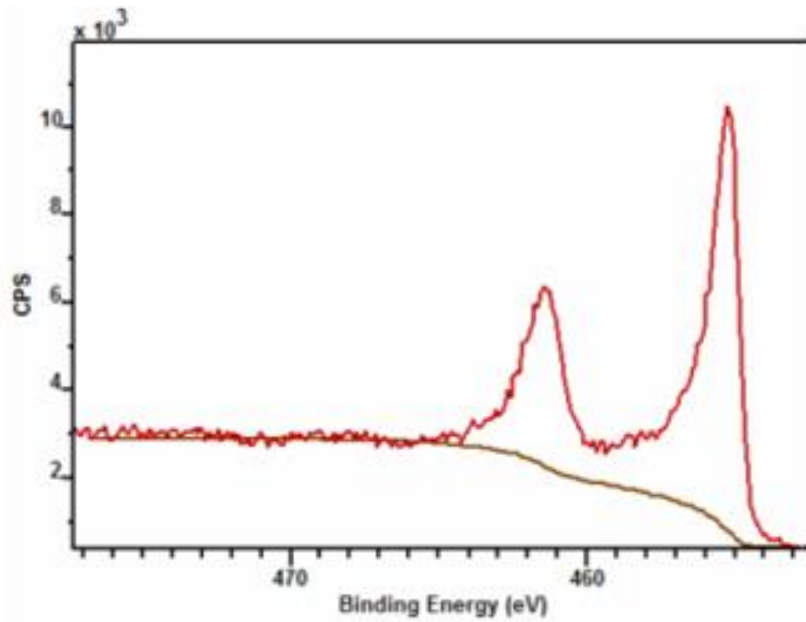

Figure 4-6 Example of the analysis using Shirley method

4.4 Data analysis

As mentioned in chapter 3, when determining the emission intensity ratio between two elements and pure emission of a particular element, it is necessary to find the exact peak intensity for each element. When calculating the element concentrations in integrated peak intensities, the background processing method is very important to ensure accurate quantification of emission spectrum measurements. In this research, the original signal was smoothed using a moving average filter and the background were then subtracted using the background subtraction method. Figure 4-8 illustrates the spectral data smoothing via the moving average filter.

4.4.1 Effect of number for moving average

Depending on the number of points used in the moving average, a moving average filter decreases the amplitude of the random noise, but also reduces the sharpness of the edge, which can affect the emission spectrum peak results. Figure 4-8 shows the nitrogen and hydrogen intensity with various moving average filter. Here, it's clearly shows that when more number of points used in the moving average, the peak of graph decreased.

4.4.2 Moving average filters with two different numbers of points

To preserve the emission spectrum peaks, moving average filters with two different numbers of points were applied to the emission spectral data. Figure 4-9 shows the hydrogen and nitrogen intensity with 3 points moving average filter at inner range (Nitrogen: 497.6 nm to 505.6 nm, Hydrogen: 650 nm to 662 nm) and various points of moving average filter at outer range of wavelength (remaining wave length). This data analysis was done to select the best way of calculation method for the next step of data analysis. As mentioned previously, a moving average filter decreases the amplitude of the random noise, but also reduces the sharpness of the edge, which can affect the emission spectrum peak results. 3 points moving average filter for inner range was selected because the peak height can be maintained. The remaining average filter was selected based on the lowest random noise but not affected the final peak of intensity. Figure 4-10 and Figure 4-11 shows the effected of peak for nitrogen and hydrogen intensity with 3 points moving average filter and various points of moving average filter. In the nitrogen emission spectrum, a 3-point moving average filter was applied from 497.6 nm to 505.6 nm, and a 7-point moving average filter was applied to the remaining

wavelengths. In the hydrogen emission spectrum, a 3-point moving average filter was applied from 650 nm to 662 nm, and a 7-point moving average filter was applied to the remaining wavelengths. The atomic emission spectra were integrated, and the background area was subtracted by putting the background into relation with the measured spectra—a technique that was first suggested by Shirley [117], and later improved by Proctor and Sherwood [118].

4.4.3 Background correction

By referring to Figure 4-7 (a) and (b), background estimation was carried out using the following steps: 1) calculate the smoothing curve of the spectrum; 2) regard the smoothing curve as the background curve in the region outside the peak; 3) select q_1 and q_2 as the start and end points of the background for a peak on the energy axis; and 4) connect points (q_1, B_1) and (q_2, B_2) on the spectrum with a line, using the background correction method. The following formula was used to estimate the background [118]:

$$BG_i(i) = \frac{(B_1 + B_2)Q_j(i)}{P_j(i) + Q_j(i)} + B_1 \qquad\qquad (23)$$

where B_1 is the average starting point and B_2 is the average end point, and $P_j(i)$ and $Q_j(i)$ are the left- and right-hand sides of the net peak area at the *i-th* point in the *j-th* approximation. Employing the trapezoidal rule, the 0-th approximation of the initial background curve BG_0 (*i*) is taken to be the straight line connecting the two points (q_1, B_1) and (q_2, B_2), and the calculations are iterated until $P_j(i) + Q_j(i)$ remains essentially unchanged.
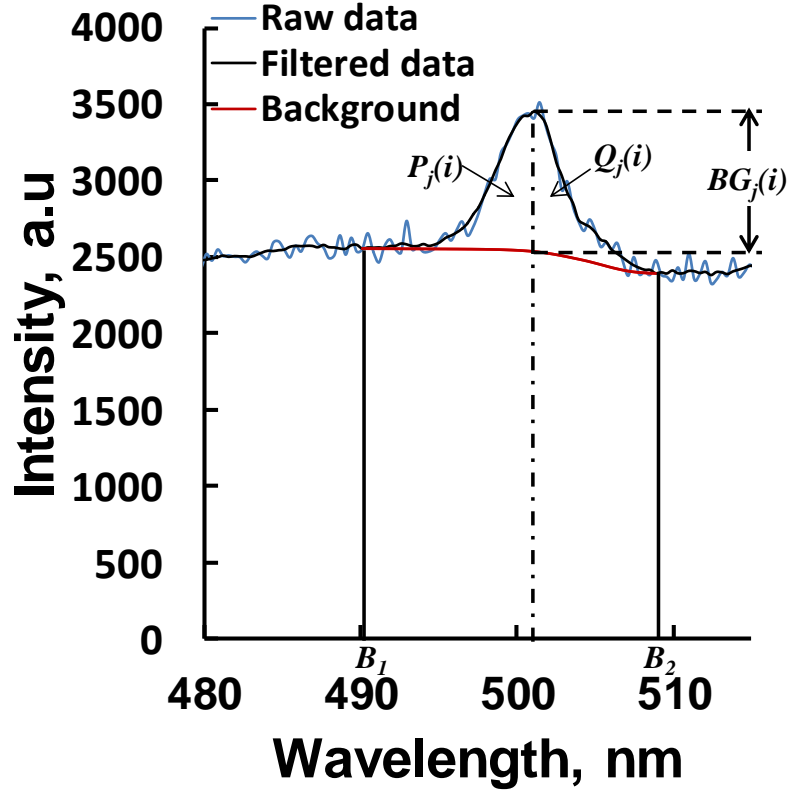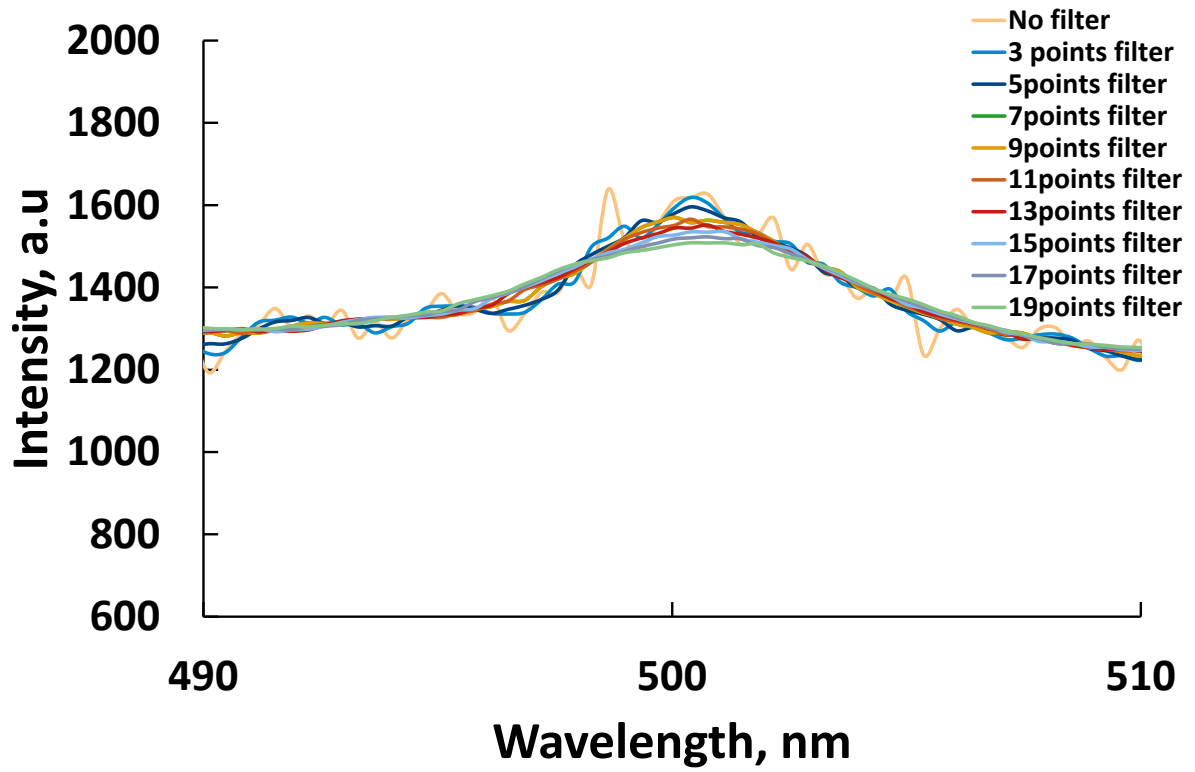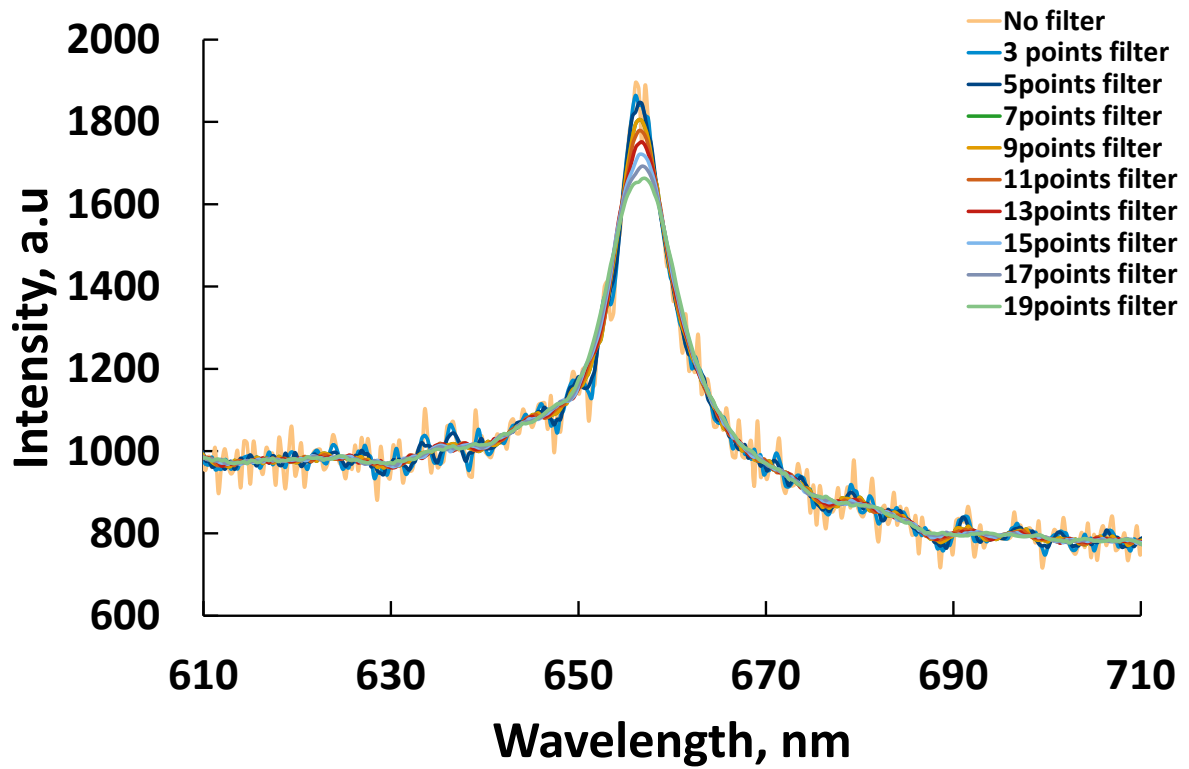
(a) NI
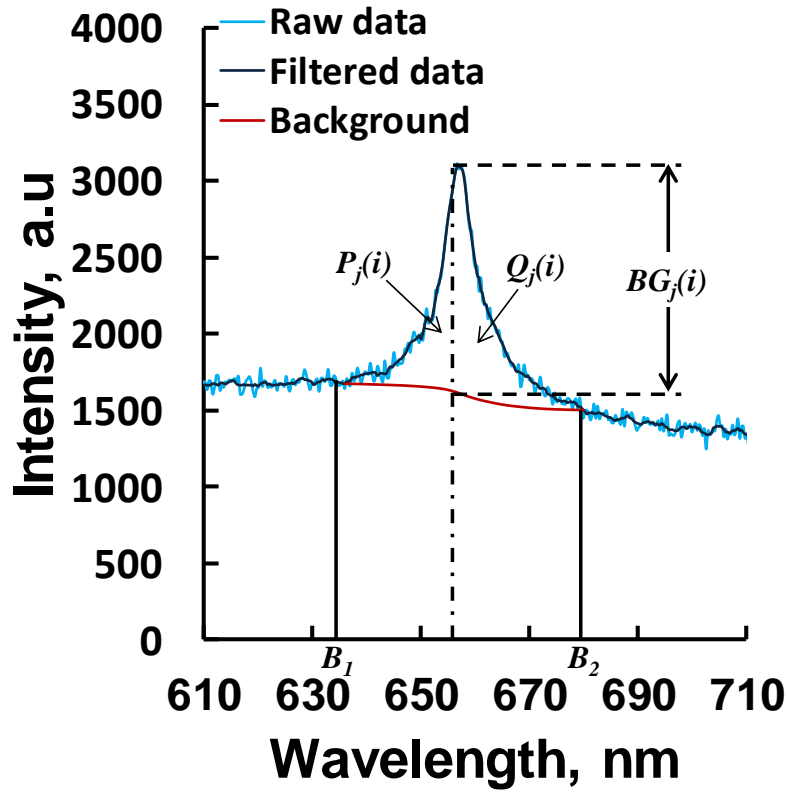
(b) H$_\alpha$

Figure 4-7 Moving average filter and diagram of the background subtraction (ϕ=0.7, P$_{amb}$=0.5MPa)

(a) NI

(b) H$_\alpha$

Figure 4-8 Nitrogen and Hydrogen intensity with various moving average filter (ϕ=0.7, P$_{amb}$=0.5MPa)
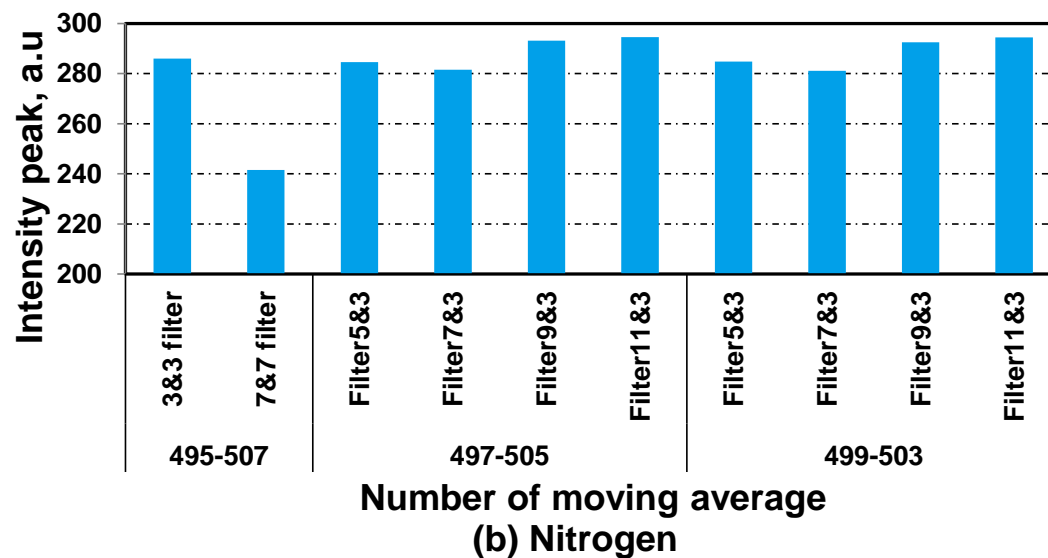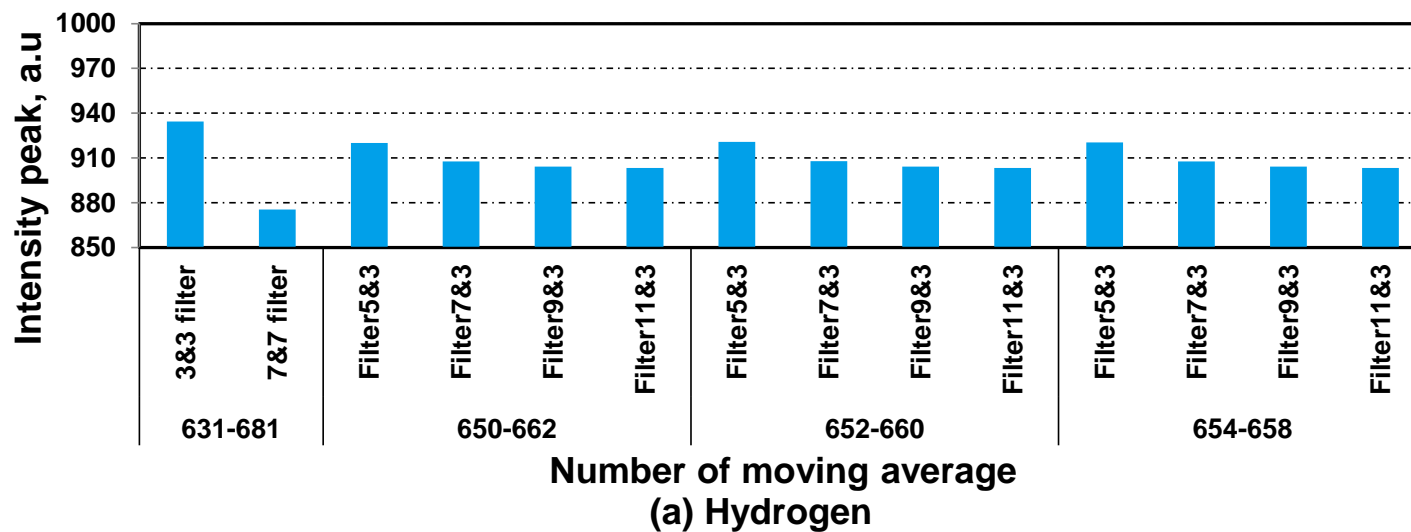
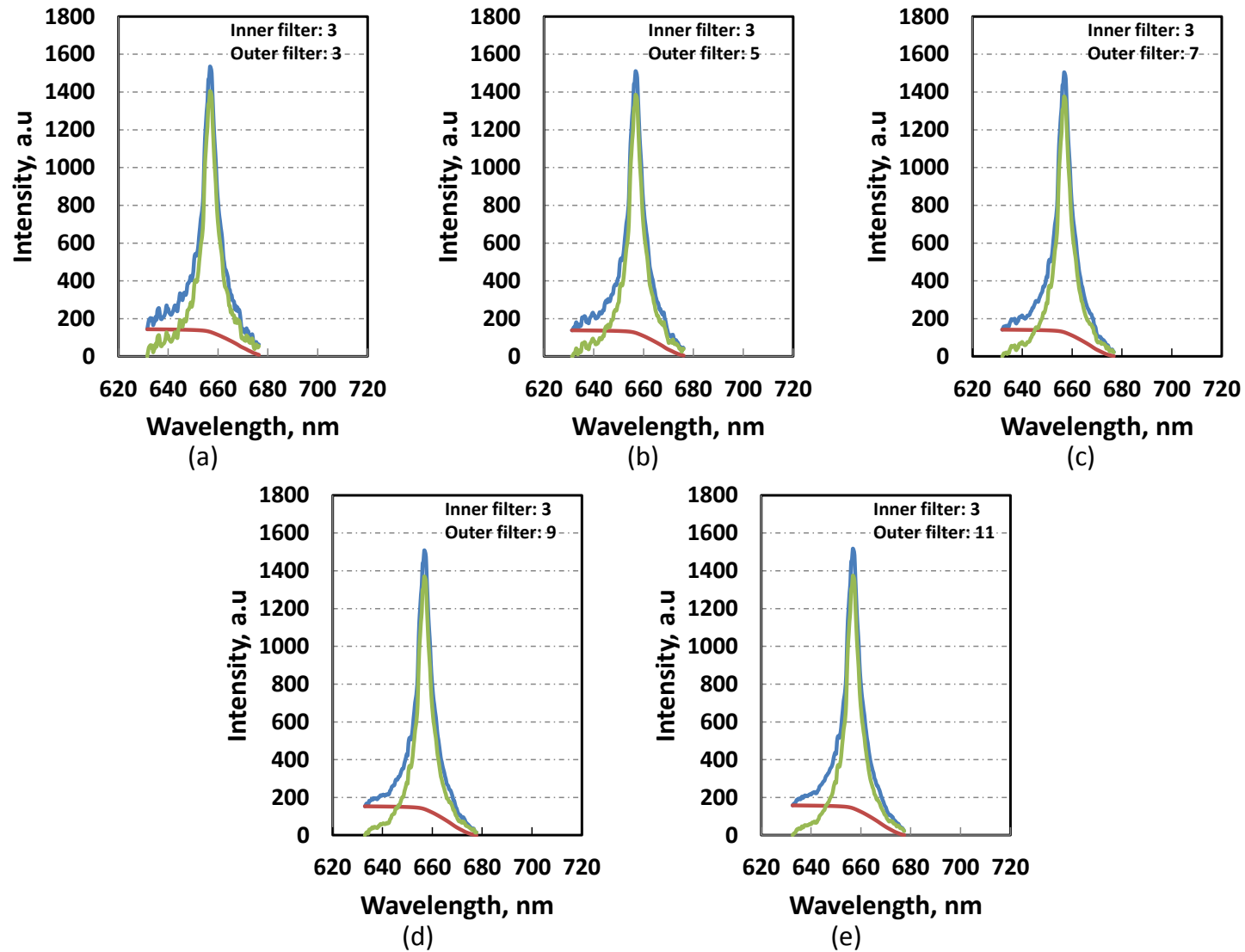Figure 4-9 Intensity peak of hydrogen and nitrogen at different number of moving average filter

Figure 4-10 Hydrogen intensity with 3 points moving average filter and various points of moving average filter
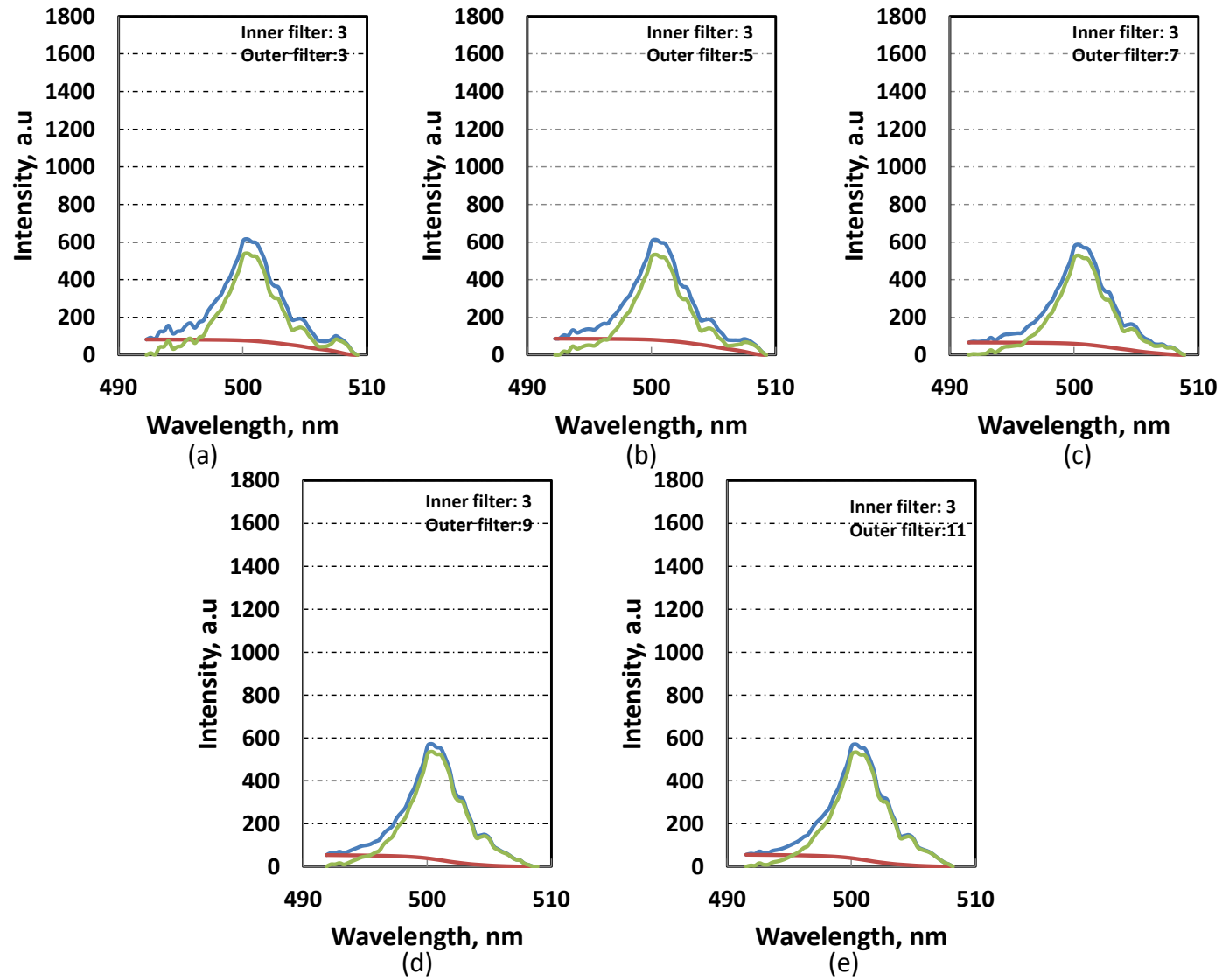
Figure 4-11 Nitrogen intensity with 3 points moving average filter and various points of moving average filter

4.5　Spectral and calibration results

Figure 4-12 shows the emission spectrum of nitrogen, measured by the SIBS sensor. The purpose of the test was to make a confirmation on the capability of spark plug sensor to detect an element inside the constant volume chamber. Pure nitrogen was transferred into the constant-volume chamber at 0.5 MPa. A spark was initiated by the SIBS sensor, and the emission spectrum was detected by the spectrometer. An emission peak from N(I) was observed, but almost no emission peak from Hα was detected.

Figure 4-13 shows the emission spectra of hydrogen/nitrogen mixture measured with SIBS sensor at three ambient pressure of 0.5 MPa, 1.0 MPa and 1.5 MPa. The results were averaged from 100 times data from each set of condition. The spectrum was before implement the background correction method. This spectrum was obtained from 1.0ms integration timing of spectrometer and 10ms duration timing of spark. Two strong atomic emission peaks was observed in spectra wavelength range from 450nm to 700nm. The peak at 656nm is from H_α while 501nm is from N(I). The intensity peaks of atomic emissions from H_α and N(I) gives the global hydrogen concentration in the measured volume. The spectrums were determined for a range of the equivalence ratio from 0.3 to 5.0. Figure 4-14 shows the intensity peak of hydrogen and nitrogen for (b) and (c) are getting higher compared with (a) due to the higher ambient pressure. The intensity peak of hydrogen shows increasing trend as the ambient pressure are increased. The hydrogen molecule is easy to be excited when the ambient pressure increase as the concentration increases. The pressure of ambient gas is directly related to the plasma density so that the absorption coefficients increase with an increase in ambient pressure. The results also show the variation of spectra in background and intensity peak for each equivalence ratio. These variation implies that there is existed a larger plasma variation during the spark discharge. The presence of the hydrogen/nitrogen in the spark region and the spark channel behavior between the electrodes gap during spark discharge might be affecting the plasma generated.
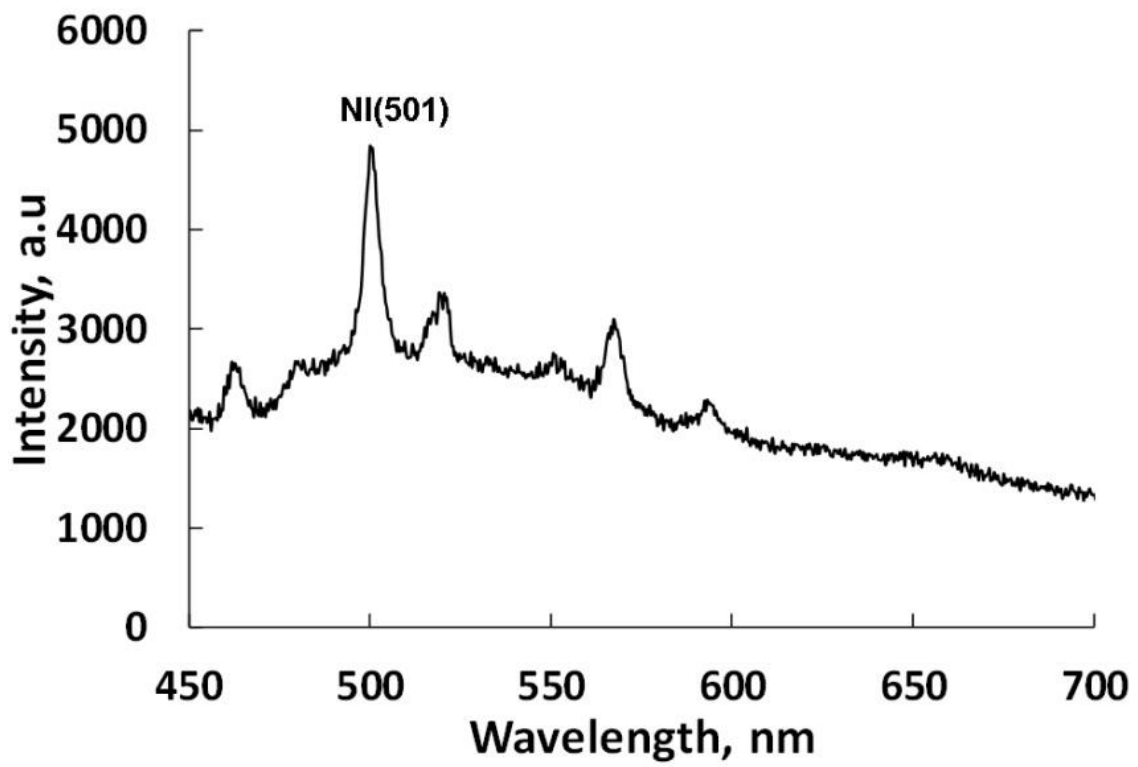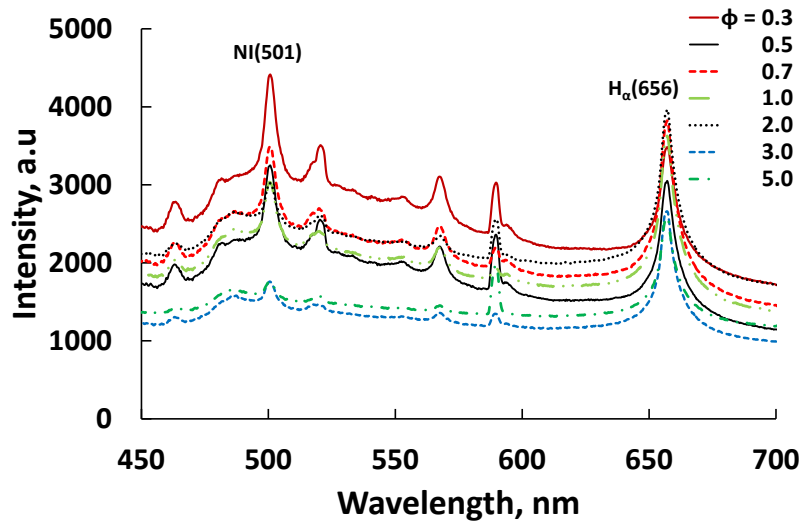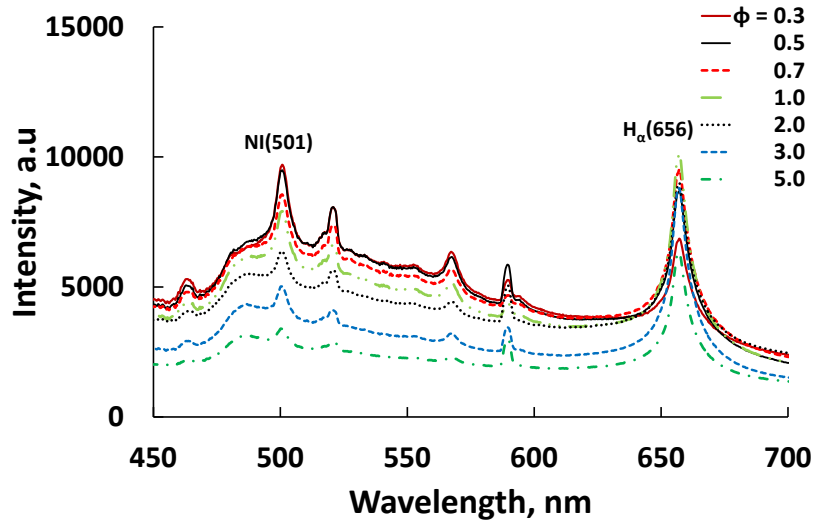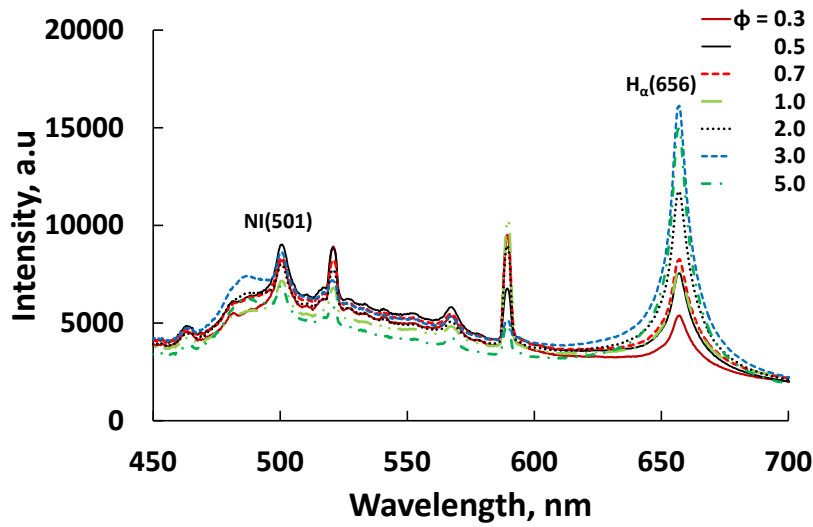
Figure 4-12 Emission spectrum of nitrogen using the SIBS sensor

(a) Pa$_{mb}$ = 0.5MPa

(b) Pa$_{mb}$ = 1.0MPa

(c) Pa$_{mb}$ = 1.5MPa

Figure 4-13 Spark emission spectra of hydrogen/nitrogen mixture using SIBS sensor

Figure 4-14 shows the relation between the equivalence ratio and the atomic emission intensity ratio of hydrogen and nitrogen obtained at three different pressures. Each curve shows an increasing trend in the slope of I_H/I_N intensity ratio according to the equivalence ratio. In the other word, the spectral intensity ratio of Hα/N(I) is proportional to the ambient pressure from 0.5 to 1.5 MPa as shown in Figure 4-15.
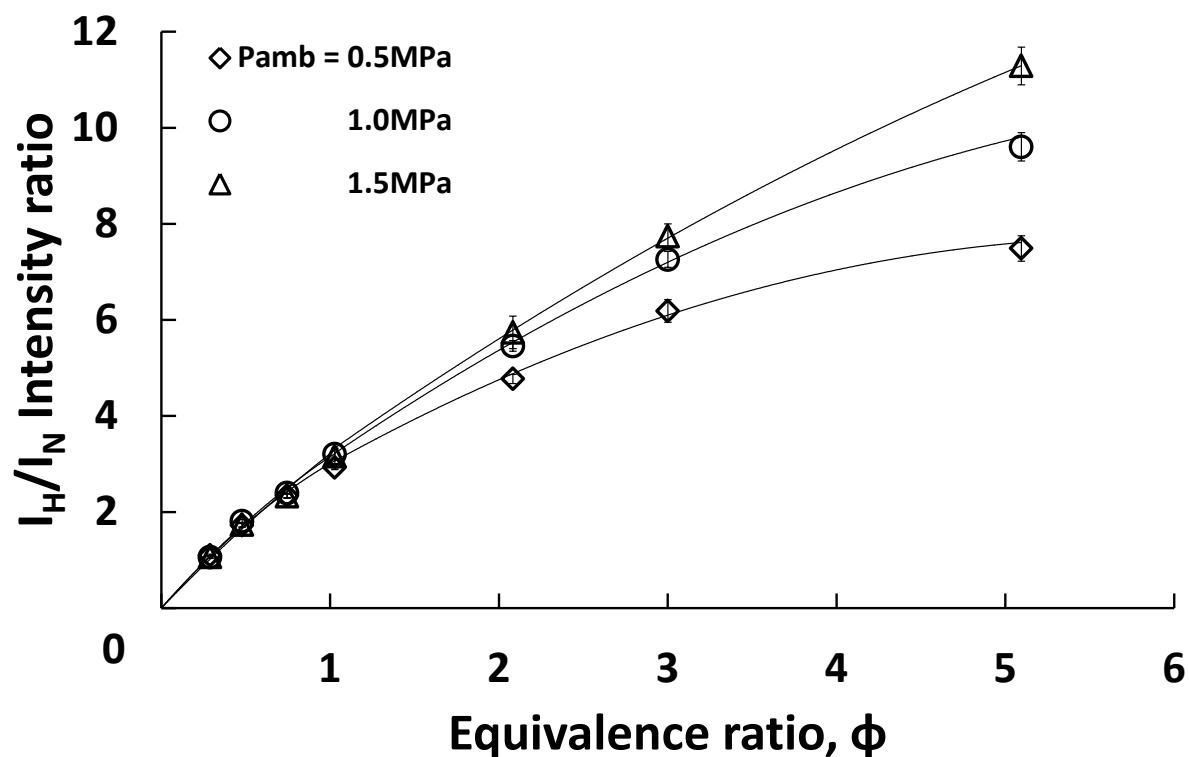

Figure 4-14 Correlation of the atomic line intensity ratio of I_H/I_N with the equivalence ratio
(room temperature)
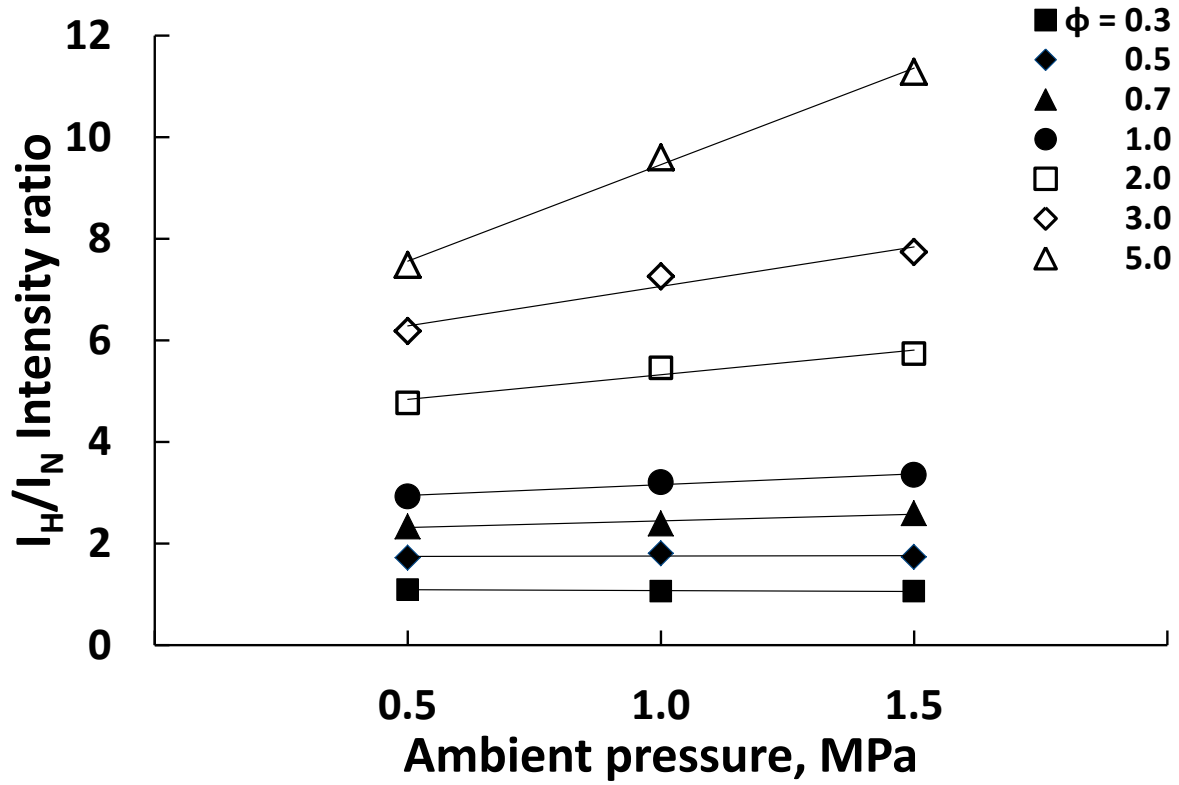
Figure 4-15 Correlation of the atomic line intensity ratio of I_H/I_N with the ambient pressure (room temperature)

An equation of I_H/I_N intensity ratio with equivalence ratio derived from the calibration curve shown in Figure 4-5 was used for the estimation of local equivalence ratio in hydrogen jet concentration measurement. These data were fitted using a second-order polynomial; i.e.,

$$I_H/I_N = c_1 \phi^2 + c_2 \phi + c_3 \qquad (24)$$

Where, I_H/I_N is intensity ratio of hydrogen and nitrogen, ϕ is equivalence ratio and c_n show the coefficients, which demonstrates the effect of ambient pressure. The coefficients of c_n can be defined with Equation (25) and Table 4-2 Coefficients according to equivalence ratio conditions, in which, P_{amb} is the ambient pressure of hydrogen/nitrogen mixture in constant-volume chamber.

$$c_n = c_{n1}P_{amb}^2 + c_{n2}P_{amb} + c_{n3} \quad (n = 1, 2, 3) \qquad (25)$$

Table 4-2 Coefficients according to equivalence ratio conditions

	$c_{11} = 0.4874$	$c_{12} = -0.4603$	$c_{13} = -0.8451$
$\phi \leq 1$	$c_{21} = -0.6374$	$c_{22} = 0.9651$	$c_{23} = 3.6407$
	$c_{31} = 0$	$c_{32} = 0$	$c_{33} = 0$
	$c_{11} = 0.111$	$c_{12} = -0.1441$	$c_{13} = -0.1566$
$\phi > 1$	$c_{21} = -1.0036$	$c_{22} = 2.368$	$c_{23} = 1.4161$
	$c_{31} = 0.8082$	$c_{32} = -1.7981$	$c_{33} = 1.5567$

4.6 Summary

The correlation between the hydrogen/nitrogen mixing ratio and atomic emission, and the post-processing procedure was discussed. Spectral calibration was carried out with a hydrogen/nitrogen mixture at pressures of 0.5, 1.0 and 1.5 MPa and at room temperature. Two clear emission peaks were observed in the wavelength range 450–700 nm; the peak at 656 nm corresponds to H_α while that at 501 nm to N(I). The intensities of these peaks are related to the global hydrogen concentration in the measured volume. The spectra were determined for a range of the equivalence ratios from 0.3 to 5.0, and the intensity of the H_α peak increases as a function of the ambient pressure, P_{amb}. Moving average filters with two different numbers of points were applied to the emission spectral data. The background correction method was used to eliminate the effects of elastic scattering. The atomic spectral lines were integrated and the background area was subtracted using the method originally reported by Shirley and later improved by Proctor and Sherwood. The results show an increase in the background radiation, as well as of the peaks corresponding to hydrogen and nitrogen atomic emission lines, as the ambient pressure increased. From the results, it is able to obtain an empirical formula for deriving the equivalence ratio for ambient pressure using the SIBS sensor.

5 Hydrogen jet concentration measurement

5.1 Experimental setup

Figure 5-1 shows the experimental apparatus used for hydrogen jet concentration measurement. The experimental apparatus consisted of three main parts: 1) the spark system with the spark plug and igniter, 2) the acquisition equipment, and 3) the synchronization system. The local fuel concentrations of the hydrogen jet were measured using the SIBS sensor in a constant-volume vessel. The gap between the ground electrode and the centre electrode was perpendicular to the injector hole. The experimental was conducted using constant volume chamber equipped with SIBS sensor. The constant volume chamber had a volume of 675 cm^3 with rectangular shape. One wall of the chamber was designed to hold the spark plug sensor, and others walls of the chamber were fitted with circular quartz windows to allow optical access. The spark plug sensor developed for this experiment used a commercial spark plug used in mass-produced real-world SI engines. The spark-plug gap was 1.5 mm to increase the stability of spark-discharge initiation, and optical UV-grade quartz fiber with a core diameter of 1000 μm (fiber diameter 1250 μm) was used to increase the light-collecting capability of the device. The optical fiber had a numerical aperture (NA) of 0.20, which covered the area around the ground electrode. The spark-charging duration was 10 ms. The ground electrode had a small projection pointing toward the centre electrode to allow stable initiation of spark discharge. This small projection was the starting point of the ionic streamer during the breakdown and arc phases. The injector was installed on the top of the chamber, so that the jet was directed perpendicularly downward into the cylinder. The hydrogen was injected using an electromagnetic fuel injector with a swirl nozzle (nozzle hole diameter: 1 mm). The jet was directed toward the spark plug to achieve stratified combustion. A high-speed CMOS (complimentary metal-oxide semiconductor) video camera (NAC Image Technology, GX8) was used to visualize the spark discharge in the constant-volume vessel. The frame resolution was set to 208×156 pixels, and the frame rate was 60,000 frames per second. The injection signal was controlled by an electric injector driver, which required a high-voltage power source and an external triggering input to control the pulse width. The onset of high-speed camera recording was synchronized with the spark system.
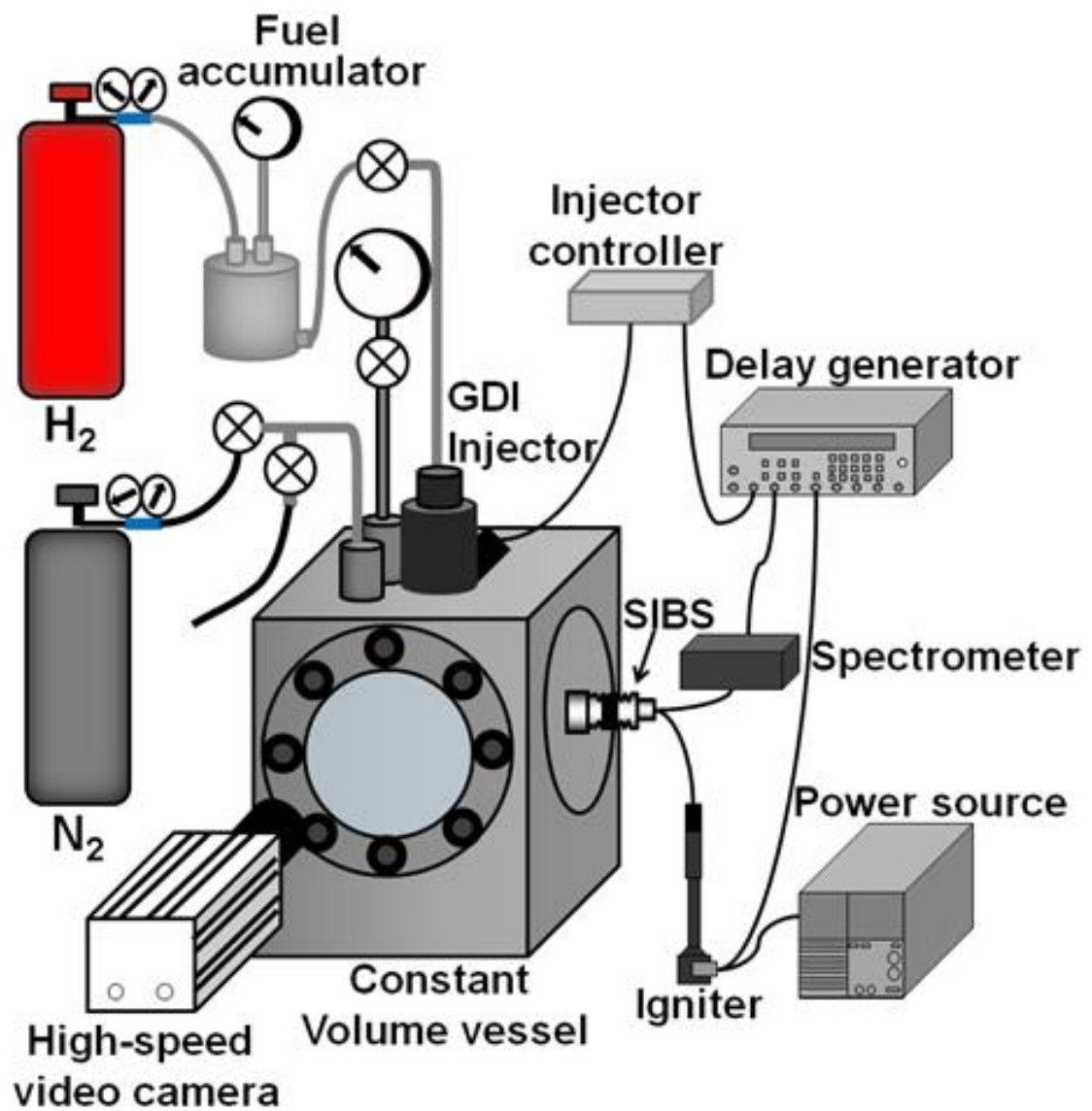
Figure 5-1 Schematic of the experimental apparatus for the hydrogen jet concentration measurements

5.2   Experimental condition and procedure

Table 5-1 summarizes the characteristics and operating conditions of the constant-volume chamber and the injector used in the hydrogen jet injection experiment. Hydrogen was supplied from a cylinder. A fuel accumulator was used to maintain a constant fuel-feed pressure to the injector. The discharge voltage and current were supplied to the SIBS sensor through a spark igniter connected to a power source. The experiment was conducted by directly injecting hydrogen at 5 MPa toward the SIBS sensor installed inside the constant-volume chamber, which was filled with nitrogen gas at a pressure of 0.5 MPa at room temperature. Local concentrations were measured at five spark locations, the coordinates of which are listed in Table 5-1. Figure 5-2 shows a schematic diagram showing the location of the electrodes and the measurement locations. The SIBS sensor emitted a spark at a specific time during the injection period, and the local concentrations of hydrogen were measured using the atomic emissions. Spark discharge fluctuations were visualized using a high-speed camera, and hydrogen jet concentration measurements were conducted simultaneously. The tests were performed for a single spark discharge to avoid perturbations produced by previous spark events. The experiment was performed 10 times for each spark mode, and the resulting data were averaged. The emission spectra of the spark obtained from the UV-grade optical fiber were detected using a spectrometer (Ocean Optics Spectrometer, USB2000+). The delay between the spark, data acquisition, and visualization was controlled by a digital delay/pulse generator (Stanford Research System DG 645).

Table 5-1 Operating conditions for the constant-volume vessel experiments

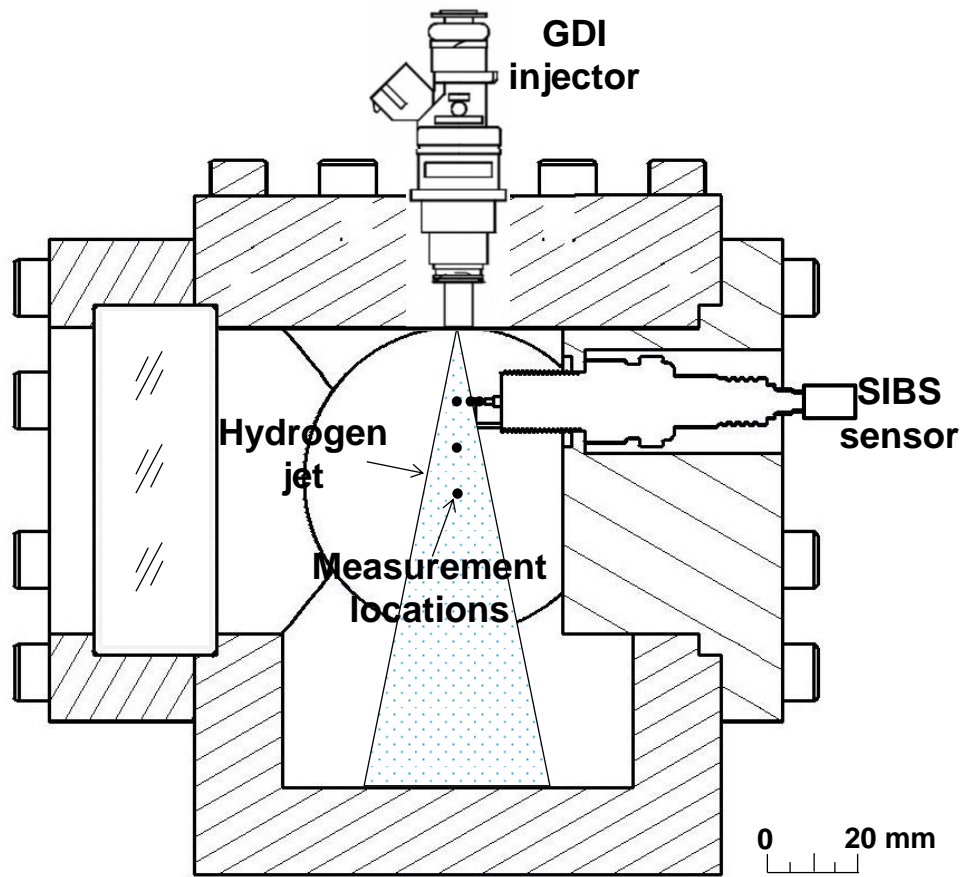|	
Fuel	Hydrogen
Ambient gas	Nitrogen
Injection pressure, MPa	5.0
Injection period, ms	33.6
Ambient pressure, MPa	0.5, 1.0, 1.5
Spark location (x, y), mm	(0, 16.5), (3, 16.5), (5, 16.5), (0, 26.5), (0, 36.5)
Spark timing	HI, CI, TI, 0.4, 0.8, 1.4ms after TI
Chamber volume, cm^3	675

Figure 5-2 A schematic diagram showing the location of the electrodes and the measurement locations

5.3　Operating conditions

Six spark modes initiated by the spark were used and the local concentration was measured. Experiments were conducted in a single-cylinder SI engine. The fuel injector was a GDI swirl injector and the injection pressure was maintained at 5 MPa. Nitrogen was introduced into the constant volume chamber initial pressure of 0.5 MPa, 1.0 MPa and 1.5 MPa. The operating condition was set based on the setting condition for the experiments in a single-cylinder SI engine (single-cylinder compression-expansion engine). The fuel-air mixture was ignited at TDC by the centrally-offset spark electrode. The four ignition modes at an overall equivalence ratio of 0.22 were categorized as shown in Figure 5-3 and can be summarized as follows:

1. Tail Ignition (TI): Hydrogen is injected during the compression stroke and ignites at the end of the injection (EOI) period. Start of injection (SOI) is at a 332° CA (variable) and the EOI is at TDC.

2. After Tail Ignition (ATI): Hydrogen is injected during the compression stroke, and the EOI is at a 5° CA before TDC. Ignition occurs at TDC. The SOI is at a 327° CA (variable) and the EOI is at a 355° CA.

3. Centre Ignition (CI): Hydrogen is injected during the latter portion of the compression stroke and ignites at TDC so that combustion occurs between the SOI and EOI. The SOI is at a 343° CA (variable) and the EOI is at a 382.5° CA.

4. Head Ignition (HI): Hydrogen is injected during the latter part of the compression stroke and ignites at TDC, close to the start of injection. The SOI is at a 355° CA and the EOI is at a 394.5° CA.

Figure 5-4 shows the temporal relation of the hydrogen injection to the spark timing conducted in current experiment. Experiments were conducted with hydrogen injection at the injection pressure of 5 MPa into the constant-volume vessel filled with nitrogen gas at the pressures of 0.5, 1.0 and 1.5 MPa. Local concentration was measured with six spark modes initiated by the spark in order to understand the effect of spark timing. The definition of the spark modes is summarized as follows:

1. Head spark (HI): spark occurs 1.4ms after the start of the hydrogen injection period.

2. Center spark (CI): spark occurs between the start of injection (SOI) and the end of injection (EOI).

3. Tail spark (TI): spark occurs at the end of the injection period (EOI).

4. 0.4ms after TI: spark occurs 0.4ms after the end of the injection period (EOI).

5. 0.8ms after TI: spark occurs 0.8ms after the end of the injection period (EOI).

6. 1.4ms after TI: spark occurs 1.4ms after the end of the injection period (EOI).
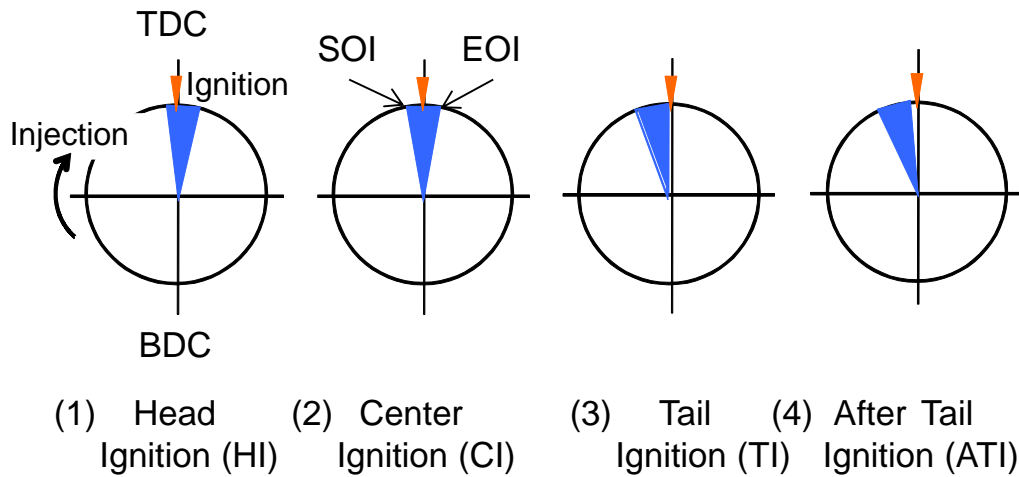
Figure 5-3 Fuel-injection timing relative to the ignition timing for the experiments conducted in a single-cylinder SI engine (single-cylinder compression-expansion engine).
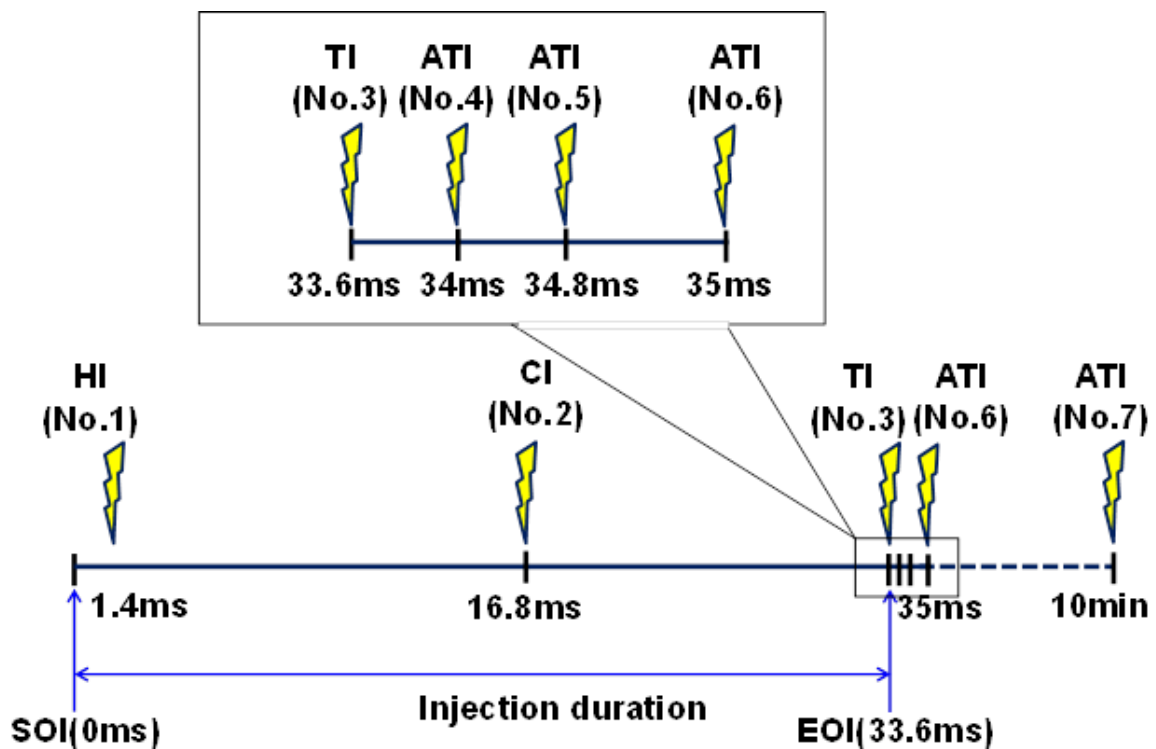

Figure 5-4 Fuel injection duration relative to the spark timing

100

5.4 Hydrogen jet evolution

Figure 5-5 shows the development of 5MPa injection pressure of hydrogen jet into 0.5 MPa, 1.0MPa and 1.5MPa ambient pressure of nitrogen[17]. The injection was achieved with an electromagnetic fuel injector with a swirl nozzle. The hydrogen jet injection distribution was visualized with a high-speed video camera (NAC Image Technology, GX-1) at 25000 frames per second. The visualization region was set approximately 20×20 mm^2 near the nozzle tip. An Argon-ion laser beam (Spectra-physics, Stabilite 2017) with an output power of 6W was used as a light source. The thickness of the laser light sheet was approximately 2 mm. A fine particle of spherical porous silica (God Ball B-6C, Suzuki Yushi Co. Ltd.) with a nominal diameter of 2.5μm was laid on the surface of injector hole so that the particle could be mixed and flowing down together with hydrogen when injection jet occurred. Choosing the appropriate size of the flow field visualization tracer was very important to accurately track the airflow. 33.6 ms injection duration of hydrogen with a feed pressure of 5MPa was directly injected into the chamber filled with 0.5 MPa, 1.0 MPa and 1.5 MPa of nitrogen. The ambient density was varied from 5.76 kg/m^3 to 17.322 kg/m^3. The images show that the hydrogen jet expands rapidly downstream from the injector hole. Based on the visualization images, the hydrogen jet was conically spread slightly more in low density compared with in high density. The direct visualization of the hydrogen jet provides useful information, because the jet pushes the quiescent nitrogen away, so that a vortex structure is formed by the interaction between the jet and the nitrogen. Although the individual images of the jet penetration appear similar, the patterns and local concentrations varied significantly. The injection of hydrogen with different ambient pressures may affect the momentum injected into the cylinder, the turbulence of the mixture, and the amount of fuel–air mixture. Compared with shadowgraph or Schlieren imaging techniques, direct visualization using tracer particles and a laser sheet beam provides a more detailed description of the cross-section of the hydrogen jet. This method was used to select the appropriate measurement points for the hydrogen concentration, based on an analysis of the optimal locations to carry out SIBS measurements.
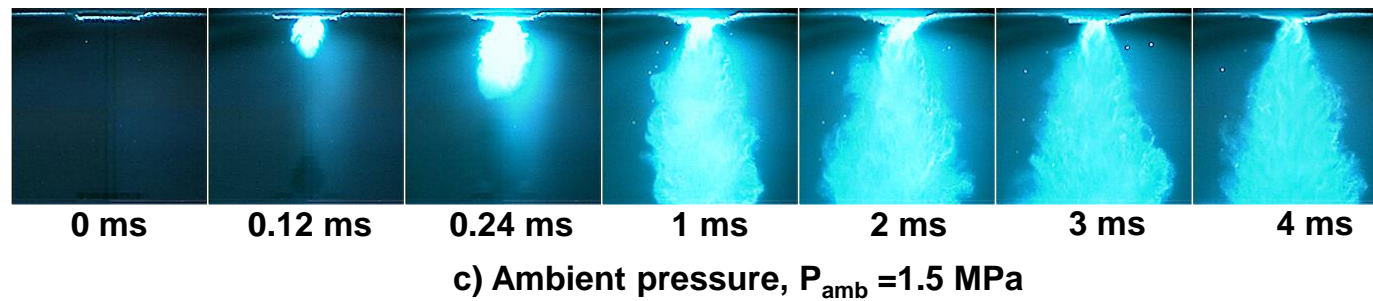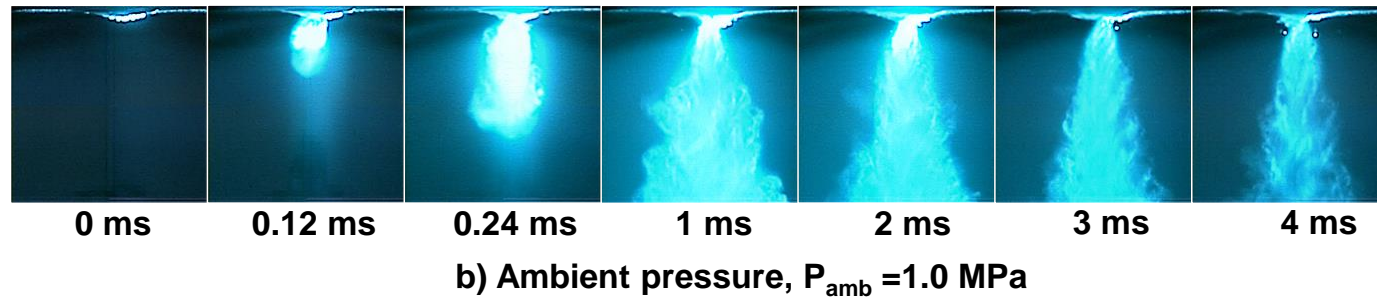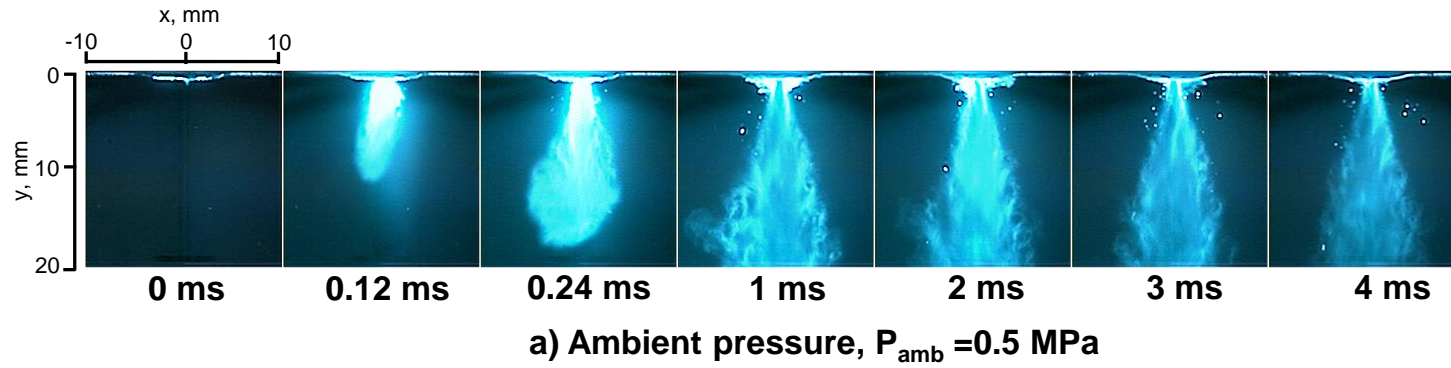
Figure 5-5 High-speed direct images of a 5MPa injection pressure hydrogen jet into nitrogen filled chamber[17]

5.5 Results and discussion

5.5.1 Spark discharge characteristics

Figure 5-6 shows an evolving time series of high-speed direct images of a spark discharge at an ambient pressure of 0.5 MPa at the location (0 mm, 16.5 mm) for each spark mode. This spark location was selected from the hydrogen jet images shown in Figure 5-5 based on the probability of where spark ignition could be obtained. A spark location near the jet is preferable for application in an actual engine. The images show that the spark discharge began as an arc discharge, followed by glow discharge. Arc and glow discharge must always be preceded by a breakdown phase, which could not be captured by the high-speed camera in this case. The breakdown phase provides a conductive path between the electrodes to start the discharge. Here, it was important that the spark-plug sensor was capable of collecting the emission spectra between the central and ground electrodes. In this experiment, the hydrogen jet was injected toward the open space between the centre and ground electrodes of the spark plug. Because of the direction of the hydrogen jet, the glow discharge channel for the HI, CI and TI modes tended to form downward toward the ground electrode of the spark plug. The first frame (at 0.017 ms) shows an arc discharge between the central and ground electrodes. Evidently, most of the glow discharge occurred outside the spark-plug gap, and most of the accumulated spectrum appeared during arc discharge. Spark discharge characteristics play an important role in producing the plasma, so the excitation of emissions varies according to these characteristics. Spark discharge behaviour might affect the generated plasma, due to the presence of hydrogen in the electrode gap and variation of the spark channel itself. The images reveal an increasing trend in the brightness of the arc discharge (first frame of each series) from HI to 1.4 ms after TI. This finding indicates that the proportion of spark is high at 1.4 ms after TI, as a result of the mixing rate of hydrogen and nitrogen.

Figure 5-7 shows the time-series evolution of high-speed direct images of spark discharge at TI spark modes during break down phase for different pressures. This experiment concerns about the spark discharge characteristic during injection of 5MPa of Hydrogen at various ambient pressures of Nitrogen and spark modes. The ambient pressure was varied from 0.2MPa to 1.5MPa, changing the ambient density from 2.24 to 16.83 kg/m3. The experiment was conducted by directly injected the hydrogen jet towards the spark plug installed inside the chamber filled with nitrogen gas. The figures show the maximum

expansion of the plasma channel increases as the gas pressure increases. The spark seems to be stable as the ambient pressure is increasing. For the ambient pressure over 1.0 and 1.5MPa, the formation time was shorter than at the ambient pressure 0.2 and 0.5MPa. At ambient pressure below than 0.5MPa, the channel of spark discharge separated in several paths. This phenomenon was almost not being observed for high pressure higher than 1.0MPa.
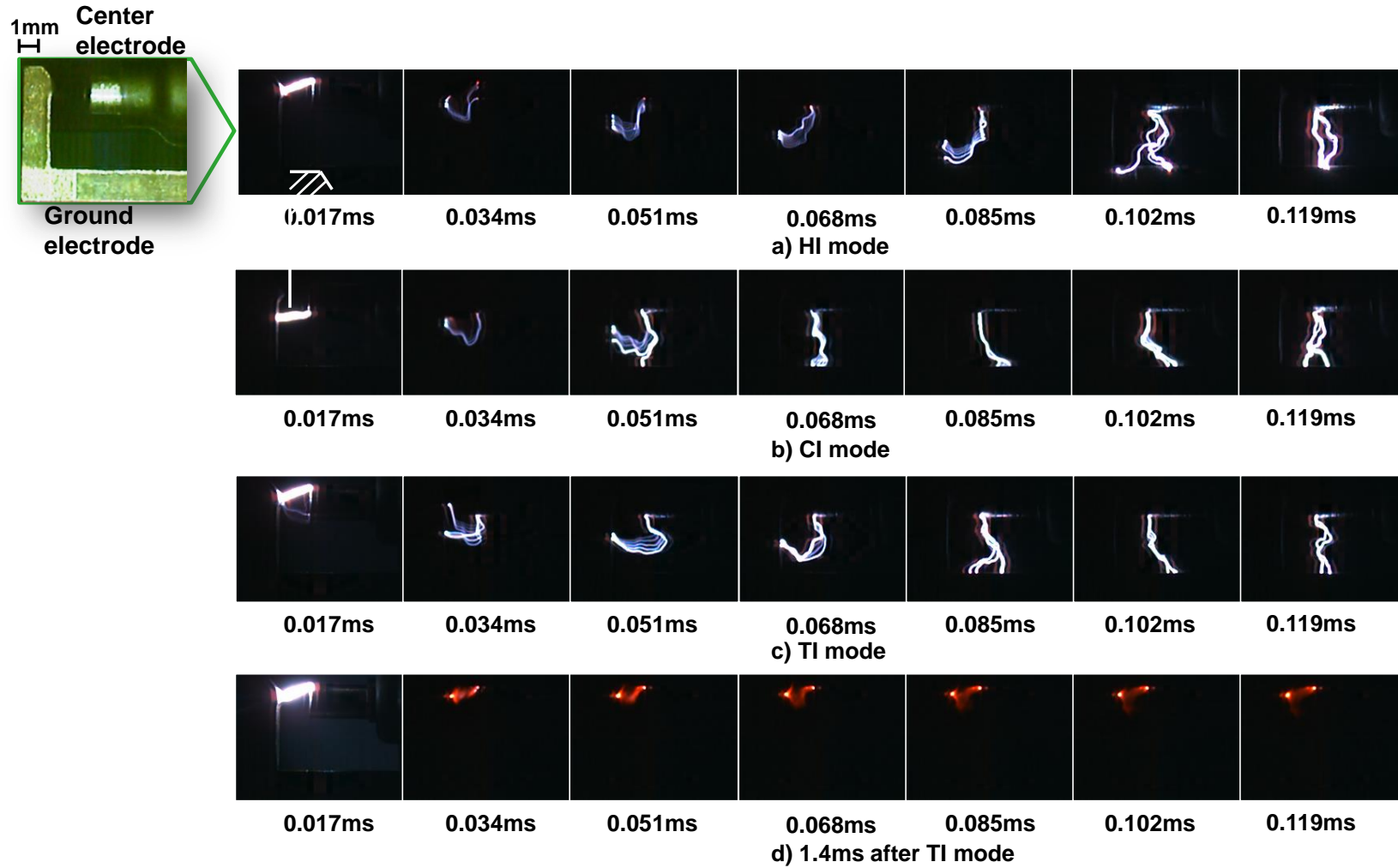
Figure 5-6 High-speed direct images of a spark discharge at location (0, 16.5) for the HI, CI, TI and 1.4 ms after TI modes
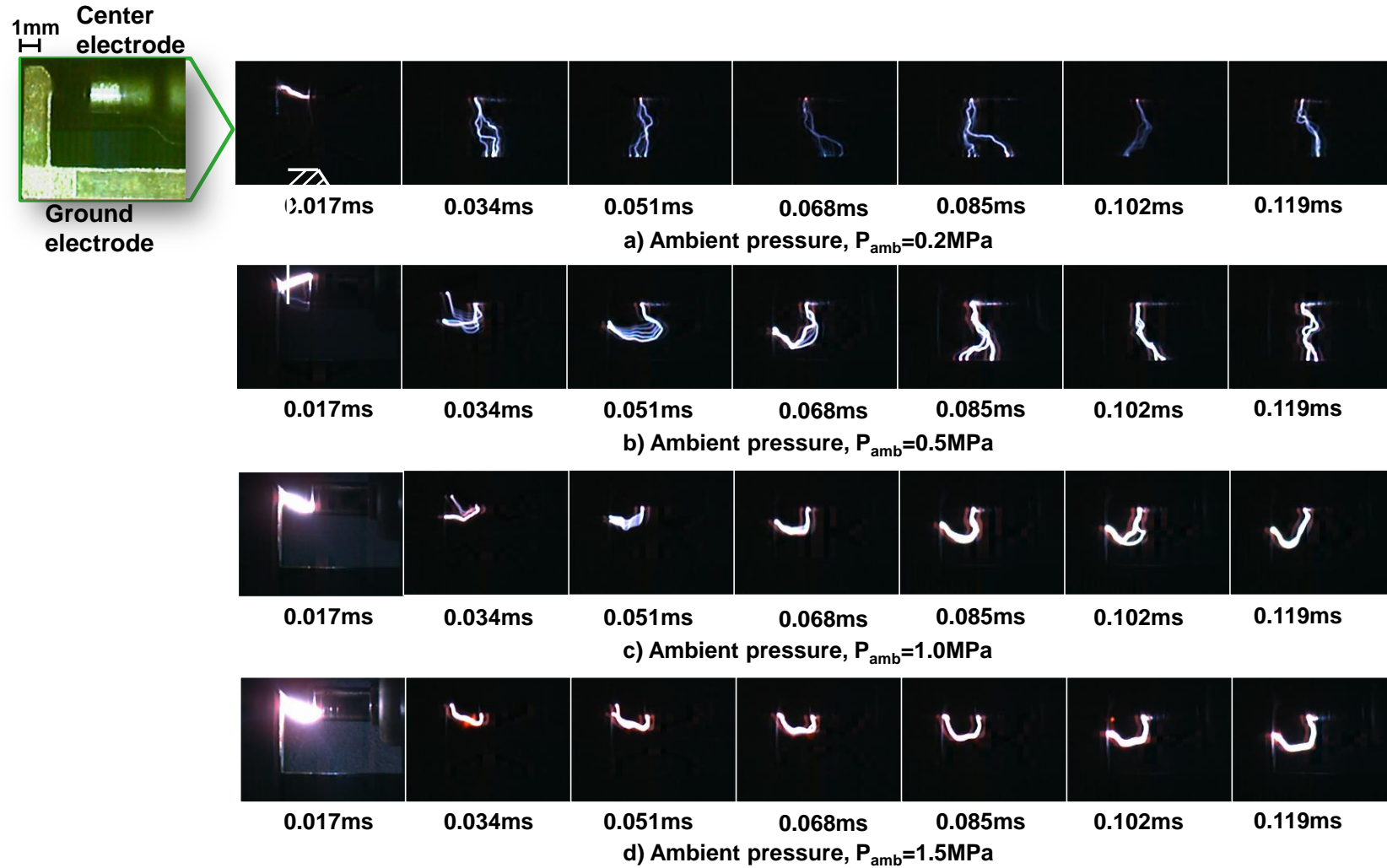
Figure 5-7 High-speed direct images of a spark discharge at location (0, 16.5) for the ambient pressure of 0.2 MPa, 0.5 MPa, 1.0 MPa, and 1.5 MPa at TI mode

106

5.5.2 Local equivalence ratio in hydrogen jet

Figure 5-8, Figure 5-9, Figure 5-10, Figure 5-11, and Figure 5-12 shows the emission spectra from SIBS sensor for the 450–700nm regions for all spark modes at all measurement locations. The experiment was conducted by feeding 5 MPa of hydrogen jet at 33.6ms injection duration into 0.5, 1.0 and 1.5 MPa ambient pressure of nitrogen. Different pressure of ambient nitrogen gives a different density of nitrogen for each condition. Substantially similar to Figure 4-13, two strong atomic emission peaks from $H\alpha$ at 656nm and N(I) at 501nm were observed. The spectrometer integration time was used of 1ms. The spectrometer was gated shortly after spark breakdown. Each spectrum corresponded to the average of 10 times of data. The spectra results showed an increasing trend in background when the ambient pressure increased as shown at all the figures. The background trend was also varied at all ambient pressure. The spectra variation in background implies that the variation of plasma atomic emission during spark discharge due to the flow of hydrogen between the electrode gap and the variation of spark discharge channel behaviour. The spectra results also show the decreasing trend in intensity and background when the distance of measurement locations increased.
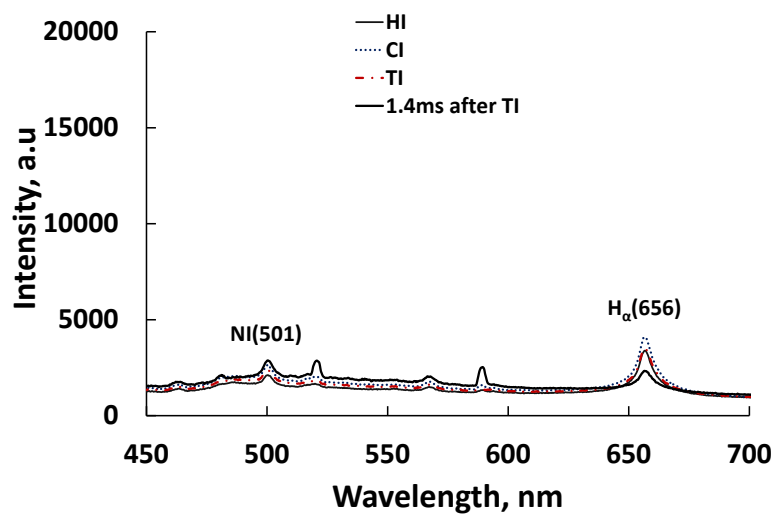
(a) $P_{amb} = 0.5MPa$
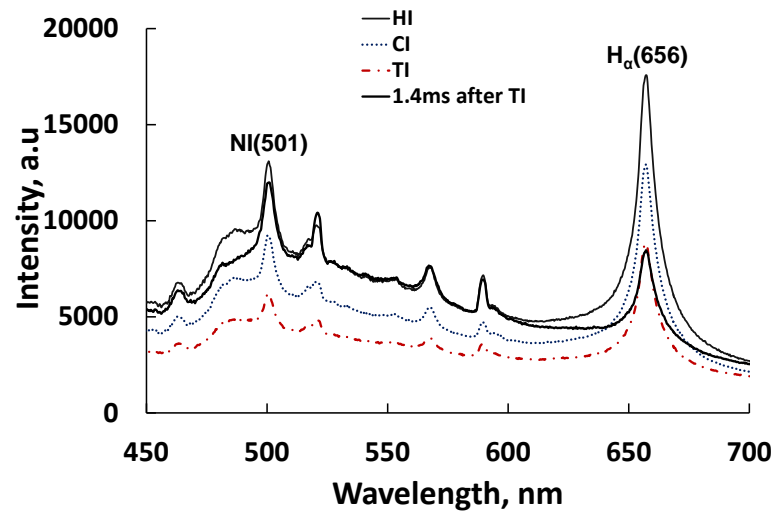
(b) $P_{amb} = 1.0MPa$
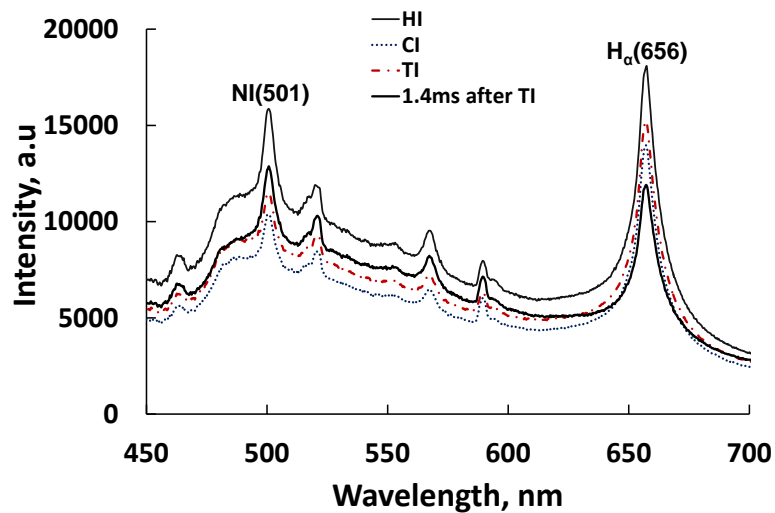
(c) $P_{amb} = 1.5MPa$

Figure 5-8 Emission spectra of spark using SIBS sensor at different spark modes at location

(0, 16.5)
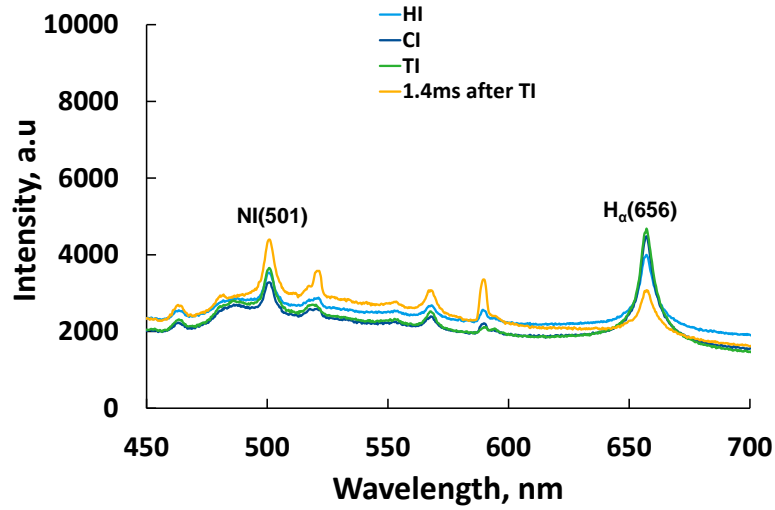
(a) $P_{amb} = 0.5MPa$

(b) $P_{amb} = 1.0MPa$

(c) $P_{amb} = 1.5MPa$

Figure 5-9 Emission spectra of spark using SIBS sensor at different spark modes at location

(3, 16.5)

(a)   Pamb = 0.5MPa

(b)   Pamb = 1.0MPa

(c)   Pamb = 1.5MPa

Figure 5-10 Emission spectra of spark using SIBS sensor at different spark modes at

location (5, 16.5)

(a)　　Pamb = 0.5MPa

(b)　　Pamb = 1.0MPa

(c)　　Pamb = 1.5MPa

Figure 5-11 Emission spectra of spark using SIBS sensor at different spark modes at location

(0, 26.5)

(a)   Pamb = 0.5MPa
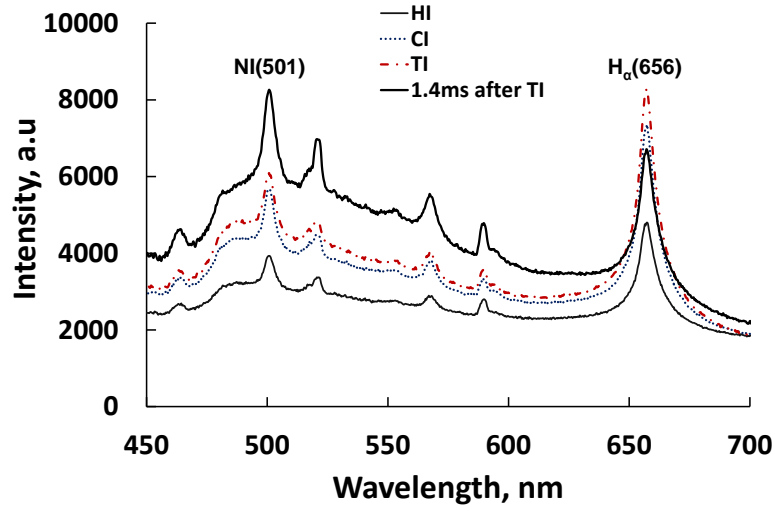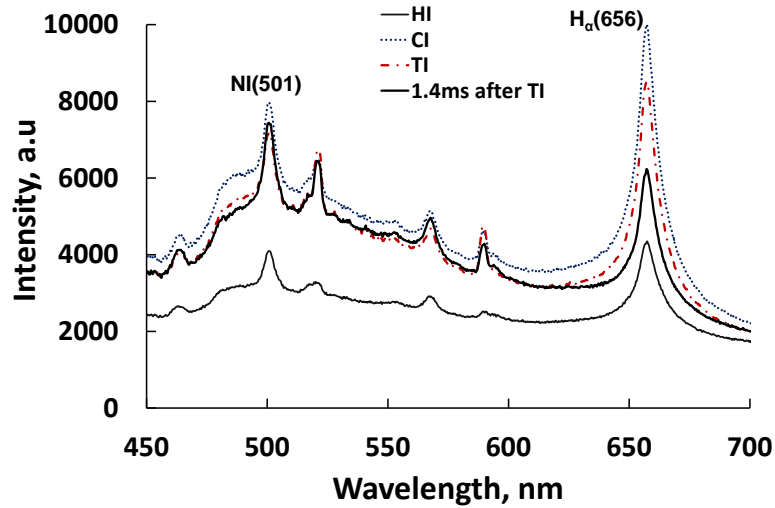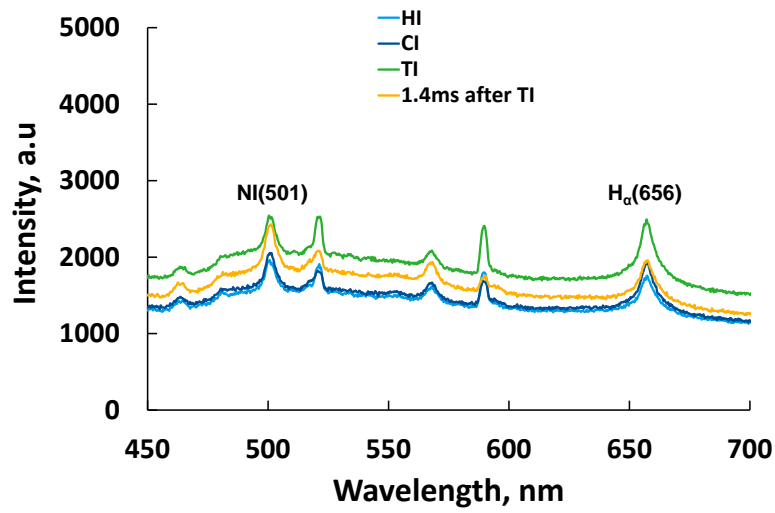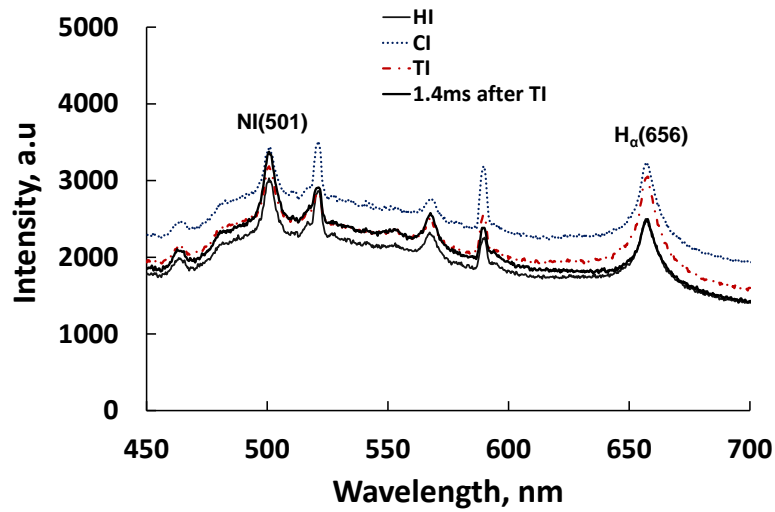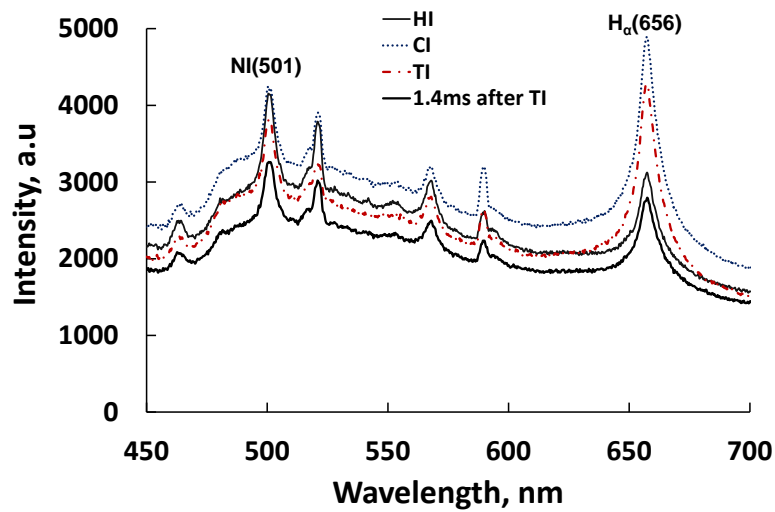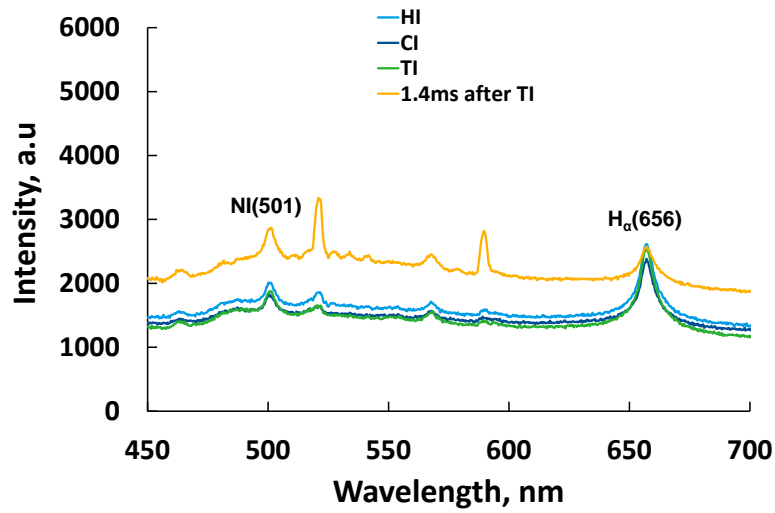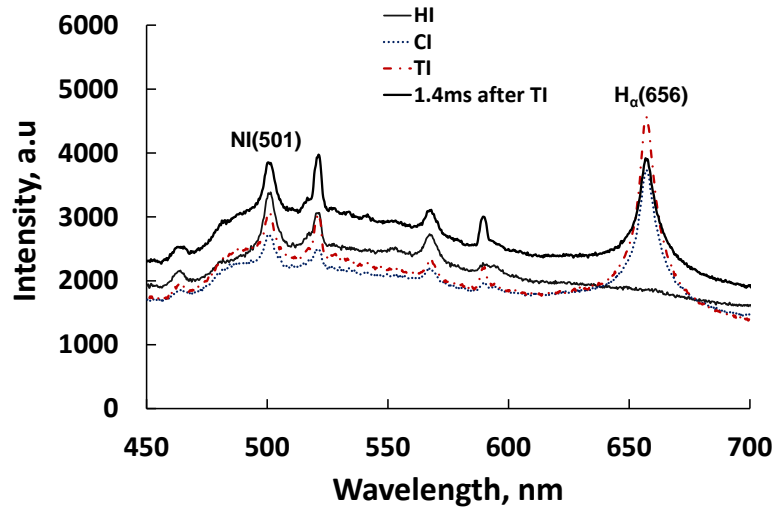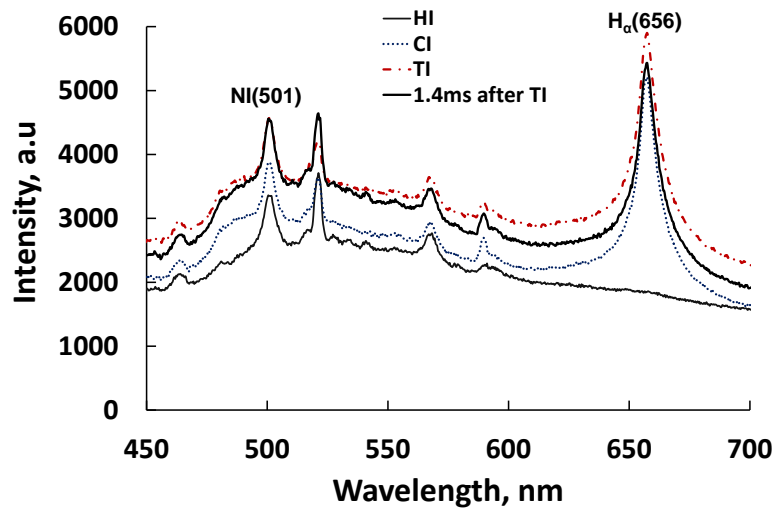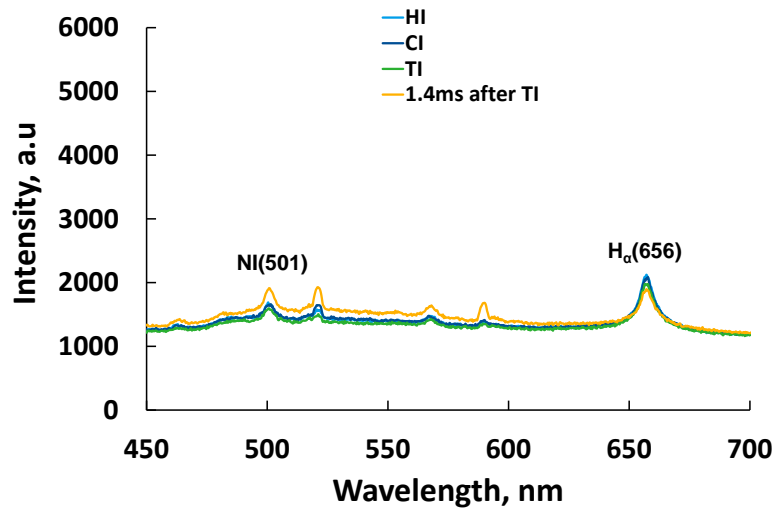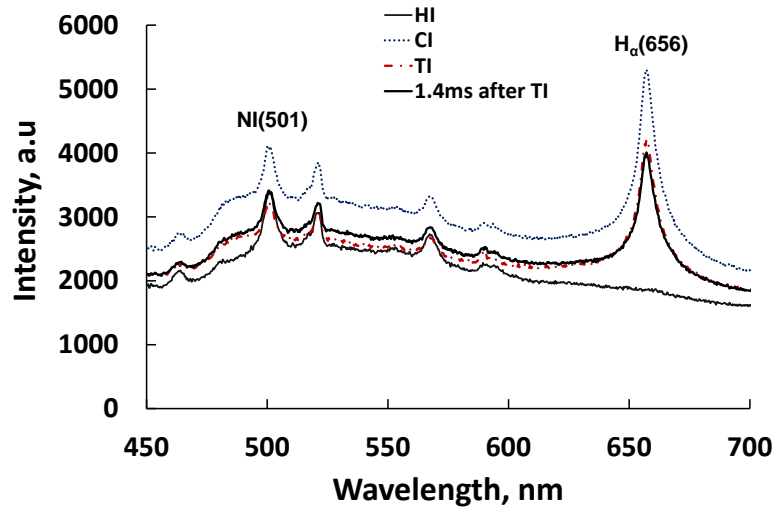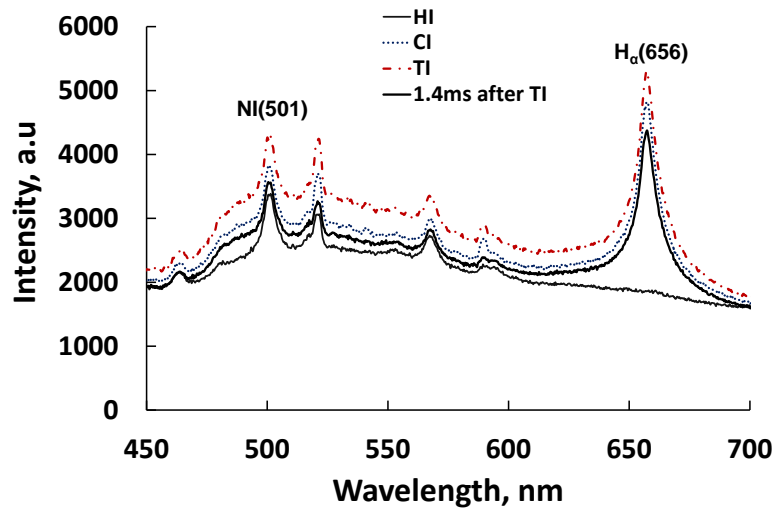

(b)   Pamb = 1.0MPa

(c)   Pamb = 1.5MPa

Figure 5-12 Emission spectra of spark using SIBS sensor at different spark modes at location
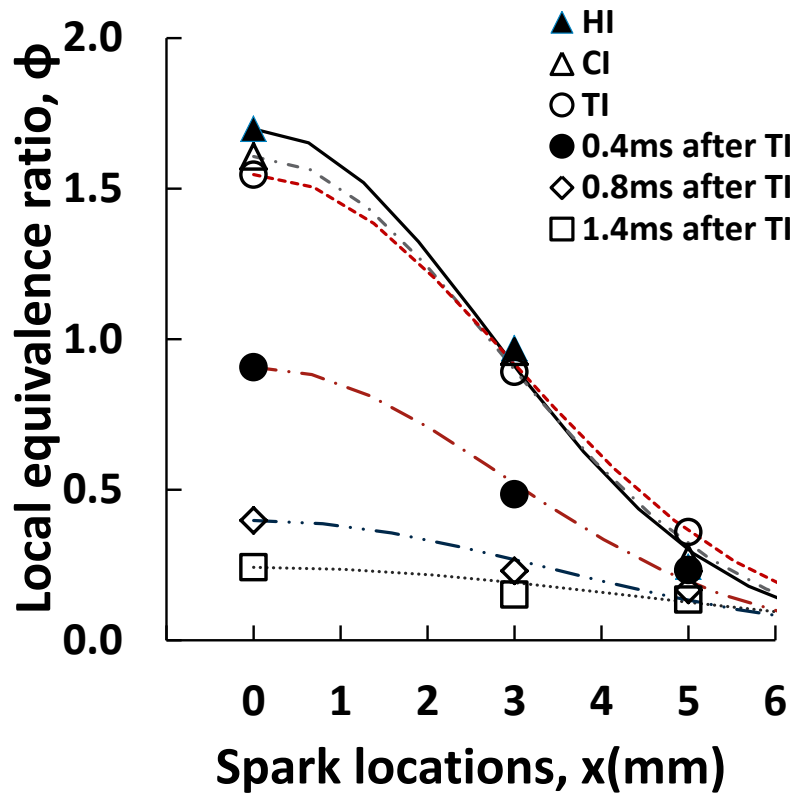
(0, 36.5)

Figure 5-13, Figure 5-14, and Figure 5-15 shows the measured equivalence ratio at $x =$ 0, 3 and 5 mm, and $y = 16.5$ mm, as well as at $x = 0$ and $y = 16.5$, 26.5 and 36.5 mm, with various spark timings and ambient pressures. The equivalence ratios for the different spark timings were obtained using the calibration data shown in Figure 4-13. The error bars show the standard deviation of the local equivalence ratios. When a hydrogen jet penetrated into the quiescent nitrogen environment, the jet expanded. As the pressure increased (and so also the density), the penetration of hydrogen jet reduced. The mixing of hydrogen and nitrogen depends on the velocity of the hydrogen jet; higher densities slowed the jet and hence altered the mixing of the two gases. The structure of the hydrogen jet resulted in different hydrogen/nitrogen mixing characteristics at the different measurement locations at the times corresponding to the spark discharge.

Figure 5-13 (a) shows the equivalence ratios at an ambient pressure of 0.5 MPa at $x =$ 0, 3 and 5 mm, and $y = 16.5$ mm. The equivalence ratios for the spark timing HI, CI and TI were a maximum at the center of the jet, and decreased with increasing radial distance from the center of the jet. For spark timings in the range 0.4–1.4 ms after TI, the spatial variation of the jet was weaker, because the jet had already passed through the measurement location. A similar trend was observed for the pressures of 1.0 and 1.5 MPa, as shown in Figure 5-14 (a) and Figure 5-15(a). The equivalence ratios with the HI spark timing at pressures of 1.0 and 1.5 MPa were lower than for 0.5 MPa, because the higher density slowed the penetration of the jet. With higher pressures, the behavior of the mixture of gases with the HI spark timing was not quasi-steady state, but rather exhibited initial unsteady behavior.

Figure 5-13 (b) shows that, with HI, CI and TI spark timings, the equivalence ratio decreased along the axis of the jet at a pressure of 0.5 MPa. The concentration of hydrogen concentration was higher with earlier spark timings because the hydrogen jet passed through the gap between the electrodes earlier. However, this sequential trend was not detected when hydrogen was injected with higher ambient pressures, shown in Figure 5-14 (b) and Figure 5-15(b), and the equivalence ratios for HI were lower at a spark location of $x = 0$ mm and $y =$ 16.5 mm compared with an ambient pressure of 0.5 MPa. Furthermore, no hydrogen was detected at the points $x = 0$ mm and $y = 26.5$ mm or $y = 36.5$ mm, because the hydrogen jet did not completely arrive at the location of the spark due to the increased density of nitrogen at higher pressures. During injection period, as the ambient pressure increased, the local

equivalence ratio generally decreased, especially for CI and TI, which follow a quasi-steady state description.

With spark timings of 0.4 and 0.8 ms after TI and a pressure of 0.5 MPa, the equivalence ratio increased with increasing measurement distance, as shown in Figure 5-13 (b); however, with ambient pressures of 1.0 and 1.5 MPa, the equivalence ratio decreased, as shown in Figure 5-14 (b) and Figure 5-15 (b). With an ambient pressure of 0.5 MPa, the rich region of the hydrogen jet was at the location $y = 16.5$ mm and moving toward the measurement locations at $y = 26.5$ mm and $y = 36.5$ mm. However, with pressures of 1.0 and 1.5 MPa, the equivalence ratio was slightly lower at $y = 36.5$mm due to the slower motion of the hydrogen jet, and the corresponding slower mixing of hydrogen and nitrogen. For a spark timing of 1.4 ms after TI, at a pressure of 0.5 MPa, the equivalence ratio of the mixture for hydrogen and nitrogen was almost homogeneous along the jet axis. However, for the higher ambient pressures, the equivalence ratio of the mixture for hydrogen and nitrogen varied due to the slower motion of the hydrogen jet and the corresponding slower mixing.

(a) Local equivalence ratio at spark location (0, 16.5), (3, 16.5), (5, 16.5)
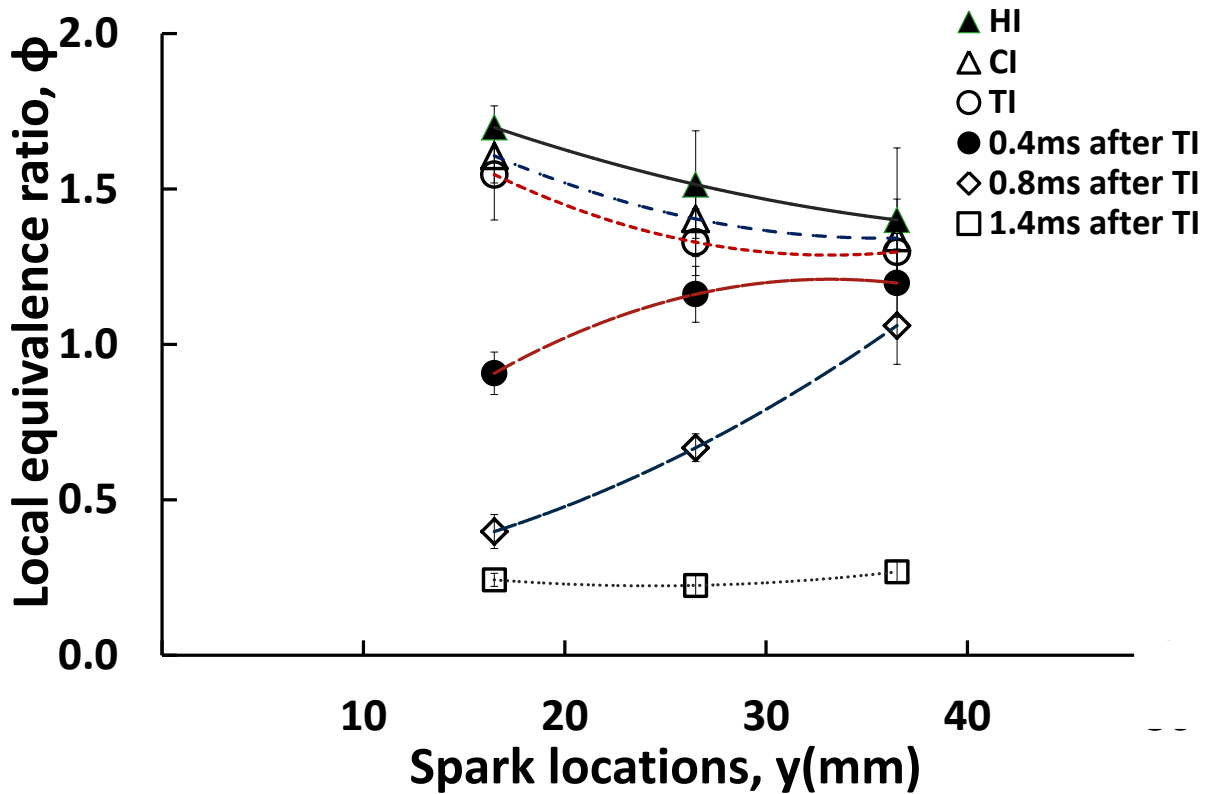
(b) Local equivalence ratio at spark location (0, 16.5), (0, 26.5), (0, 36.5)

Figure 5-13 Local equivalence ratio at different spark modes and ambient pressures of 0.5
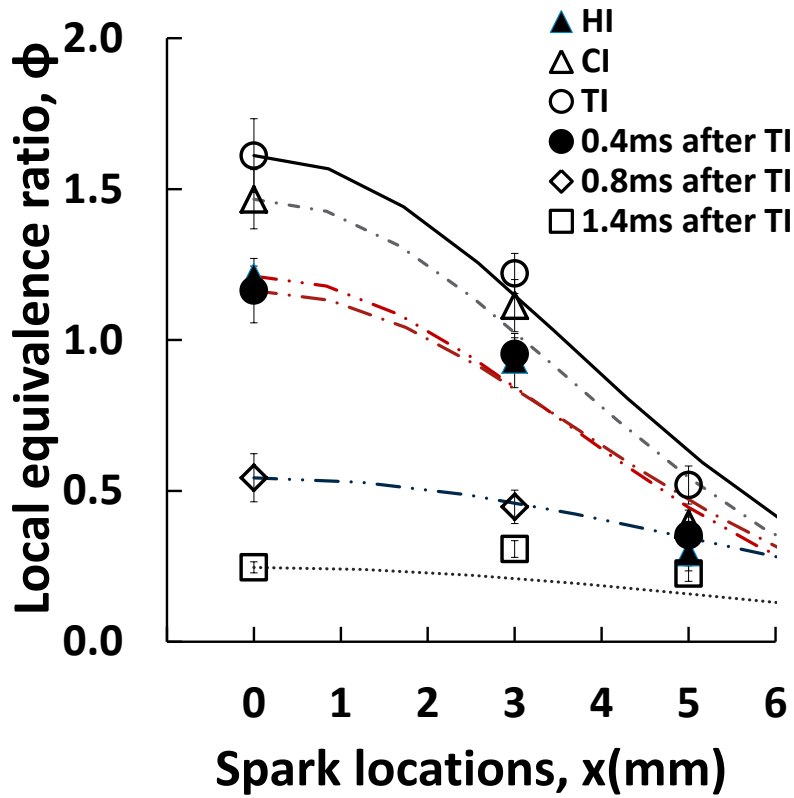
MPa

(a) Local equivalence ratio at spark location (0, 16.5), (3, 16.5), (5, 16.5)
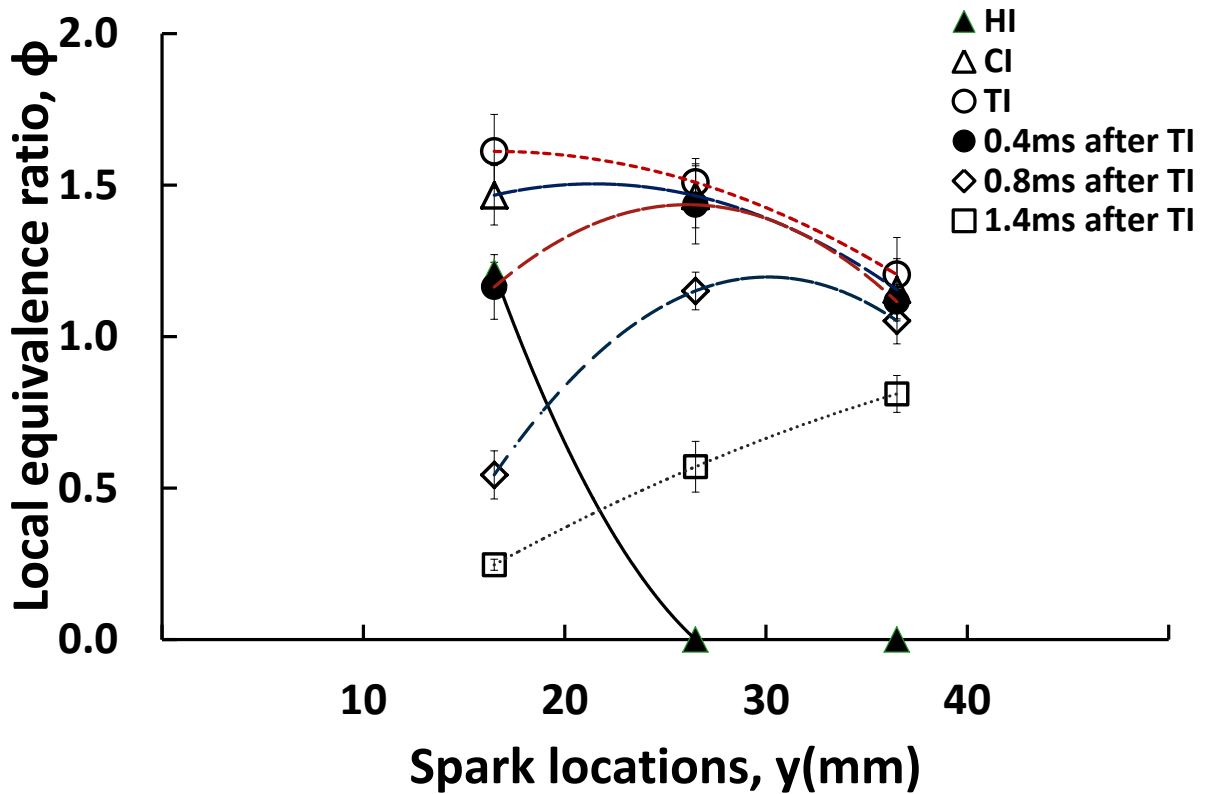
(b) Local equivalence ratio at spark location (0, 16.5), (0, 26.5), (0, 36.5)

Figure 5-14 Local equivalence ratio at different spark modes and ambient pressures of 1.0 MPa
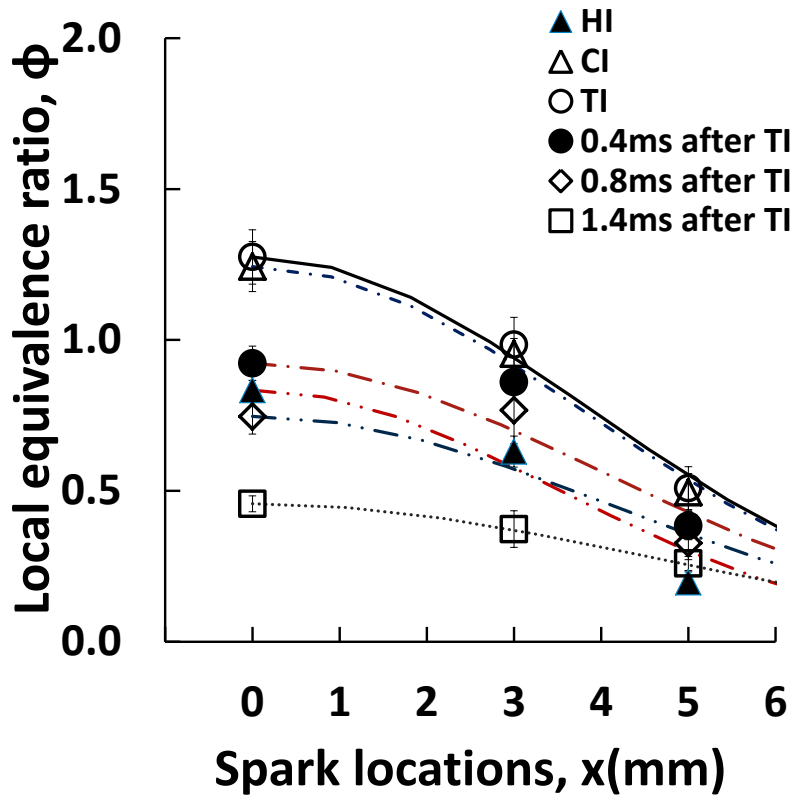
(a) Local equivalence ratio at spark location (0, 16.5), (3, 16.5), (5, 16.5)
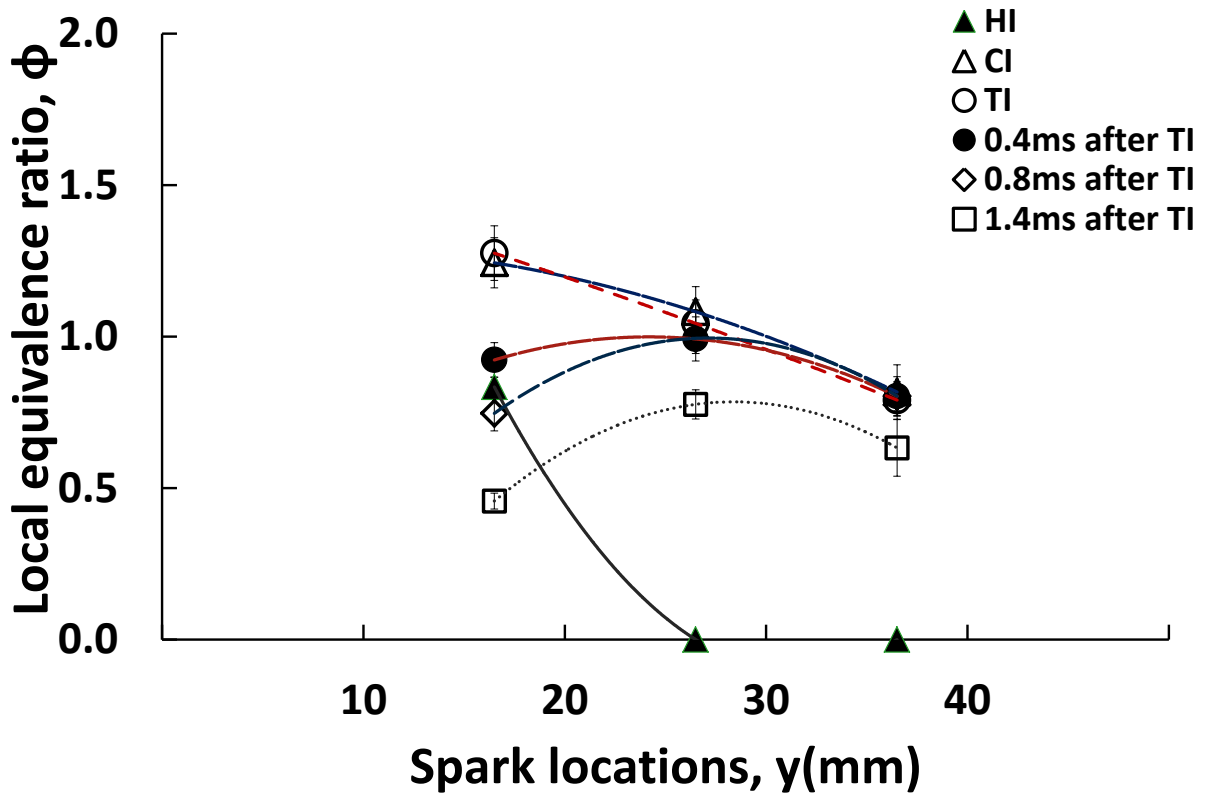
(b) Local equivalence ratio at spark location (0, 16.5), (0, 26.5), (0, 36.5)

Figure 5-15 Local equivalence ratio at different spark modes and ambient pressures of 1.5 MPa

Based on the results, the observed mixing processes could be classified into three states, (i) an initial unsteady state (HI with P_{amb} = 1.0 and 1.5 MPa), (ii) a quasi-steady state (HI with P_{amb} = 0.5 MPa, and CI and TI with P_{amb}= 0.5, 1.0 and 1.5 MPa) and (iii) an after-injection unsteady state (after EOI with all conditions). The quasi-steady state occurred during the injection of hydrogen into the nitrogen ambient. Following hydrogen injection, an unsteady state occurred and the hydrogen/nitrogen mixing process was active, leading to a homogeneous mixture. Figure 5-16 shows the dimensionless radial distribution of the local equivalence ratio for HI, CI and TI conditions (except for 0.4, 0.8 and 1.4 ms after TI); after injection an unsteady state occurred. The equivalence ratio may be calculated as follows [119]:

$$\phi/\phi_M \ = \ C/C_M \ = \ \exp\{-0.693\,(x/x_M\,)^2\} \qquad\qquad (26)$$

where, ϕ_M and C_M are the maxima of the local equivalence ratio and the fuel concentration, respectively, and x_M is the radial distance from axis of the jet, as shown by the solid line in the Figure 5-16. Note that the instantaneous local equivalence ratio ϕ was half of the maximum concentration at the jet axis. This graph was obtained using the data plotted in Figure 5-13 (a), Figure 5-14 (a) and Figure 5-15 (a). Although with HI and P_{amb}= 1.0 and 1.5 MPa, an initial unsteady state was observed, with HI, CI and TI, the behavior was consistent with a quasi-steady state.
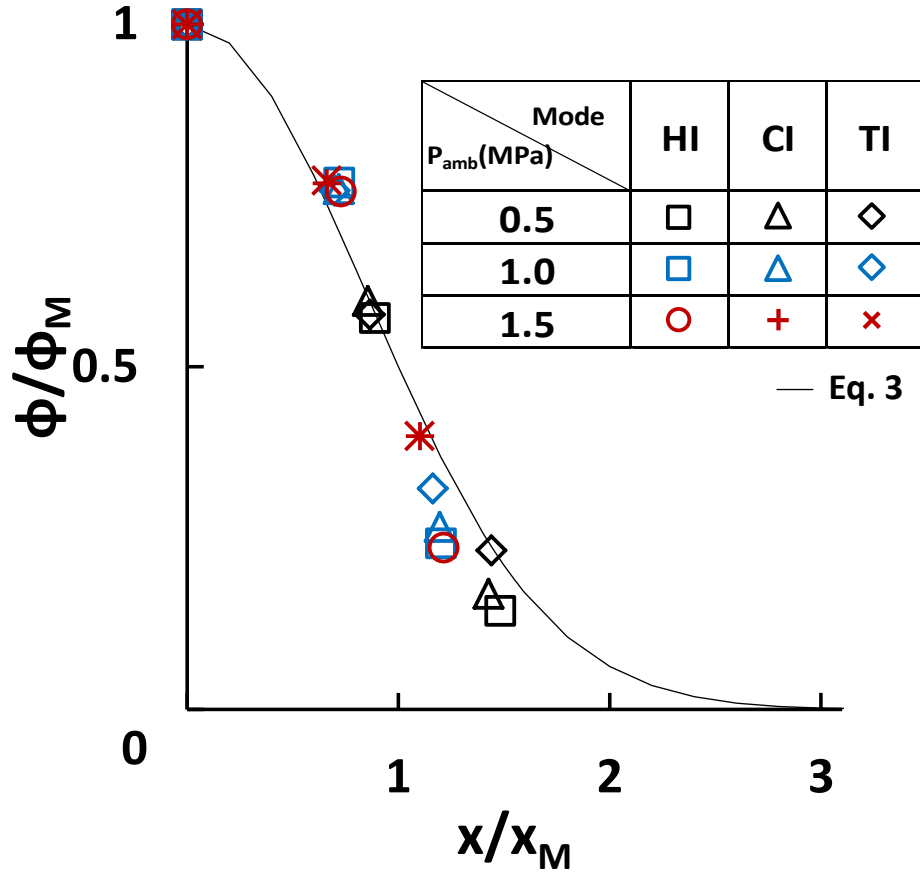
Figure 5-16 Dimensionless radial distribution of local equivalence ratio

5.6 Summary

The injection of hydrogen with different ambient pressures visualized with a high-speed video camera was conducted to study the distribution pattern of hydrogen jet and to select the appropriate measurement points for the hydrogen concentration for optimal locations to carry out SIBS measurements. A high-speed camera was used to visualize spark discharge fluctuations, and hydrogen jet concentration measurements were conducted simultaneously. Direct visualization of the spark discharge provided useful information about the influence of spark discharge characteristics related to the spark timing. The images show that the spark discharge began as an arc discharge, followed by glow discharge. Arc and glow discharge must always be preceded by a breakdown phase. The spark-plug sensor was capable of collecting the emission spectra between the central and ground electrodes. Based on the visualization images, the maximum expansion of the plasma channel increases as the gas

pressure increases. The spark seems to be stable as the ambient pressure is increasing. For the ambient pressure over 1.0 and 1.5MPa, the formation time was shorter than at the ambient pressure 0.2 and 0.5MPa. At ambient pressure below than 0.5MPa, the channel of spark discharge separated in several paths. This phenomenon was almost not being observed for high pressure higher than 1.0MPa. Spectrally resolved atomic emissions from the plasma generated by the spark plug were examined to determine the local equivalence ratio. Using the developed SIBS sensor, atomic emission spectra were obtained from hydrogen H_α at 656 nm and nitrogen N (I) at 501 nm. Comparison of the intensity peaks of atomic emissions from hydrogen and nitrogen allows the local hydrogen concentration in a measured volume to be determined, and hence also the local equivalence ratio. The measurement results demonstrate the local variation in the equivalence ratio throughout the jet and along its axis. Based on the study, the mixing process can be classified into three states, (i) initial unsteady state (HI at P_{amb}=1.0 and 1.5 MPa), (ii) quasi-steady state (HI at P_{amb}=0.5 MPa, CI and TI at P_{amb}= 0.5, 1.0, 1.5 MPa) and (iii) after-injection unsteady state (ATI in all conditions). From the results, the spatial structure of the hydrogen jet affects the hydrogen/nitrogen mixing and could be clarified with SIBS technique when the spark is discharged.

6 Conclusions

The objective of this research was to determine the concentration of a direct-injection hydrogen jet in a constant-volume vessel to investigate the mixing process. To this end, the atomic spark light emissions were observed. Direct visualization of the spark discharge provided useful information about the influence of spark discharge characteristics relative to the spark timing. Based on the results, the following conclusions can be drawn:

1. The correlation between the hydrogen/nitrogen ratio and atomic emission was determined, and the post-processing procedure was calibrated. Two clear emission peaks were observed in the wavelength range 450–700 nm; the peak at 656 nm corresponds to H_α while that at 501 nm to N(I). The intensities of these peaks are related to the global hydrogen concentration in the measured volume. The spectra were determined for a range of the equivalence ratios from 0.3 to 5.0. The relation between the equivalence ratio and the atomic emission intensity ratio of hydrogen and nitrogen was obtained at three different pressures of 0.5 MPa, 1.0 MPa and 1.5 MPa at room temperature. Each curve of graph shows an increasing trend in the slope of I_H/I_N intensity ratio according to the equivalence ratio. In the other word, the spectral intensity ratio of Hα/N(I) is proportional to the ambient pressure from 0.5 to 1.5 MPa. From the results, it is able to obtain an empirical formula for deriving the equivalence ratio for ambient pressure using the SIBS sensor.

2. The background processing method was used for the calculation of element concentrations in integrated peak. The method is very important to ensure accurate quantification of emission spectrum measurements. In this research, the original signal was smoothed using a moving average filter and the background were then subtracted using the background subtraction method. A moving average filter decreases the amplitude of the random noise, but also reduces the sharpness of the edge, which can affect the emission spectrum peak results. To preserve the emission spectrum peaks, moving average filters with two different numbers of points were applied to the emission spectral data. In the nitrogen emission spectrum, a 3-point moving average filter was applied from 497.6 nm to 505.6 nm, and a 7-point moving average filter was applied to the remaining wavelengths. In the hydrogen emission spectrum, a 3-point

moving average filter was applied from 650 nm to 662 nm, and a 7-point moving average filter was applied to the remaining wavelengths.

3. A high-speed camera was used to visualize spark discharge fluctuations. Direct visualization of the spark discharge provided useful information about the influence of spark discharge characteristics related to the spark timing during the injection of hydrogen jet. The images show that the spark discharge began as an arc discharge, followed by glow discharge. Arc and glow discharge must always be preceded by a breakdown phase. The spark discharge visualization revealed that arc discharge occurs between the central and ground electrodes, whereas most of the glow discharge occurs outside the spark plug gap. It also revealed that most of the accumulated spectrum appears during arc discharge. Additionally, the spark gap plays an important role in terms of the ability to collect emission spectra between the central and ground electrodes. Based on the visualization images at different pressures, the maximum expansion of the plasma channel increases as the gas pressure increases. The spark seems to be stable as the ambient pressure is increasing. The SIBS sensor was capable of collecting the emission spectra between the central and ground electrodes.

4. Spectrally resolved atomic emissions from the plasma generated by the spark plug were examined to determine the local equivalence ratio. Measurements were taken at different locations in a direct-injection hydrogen jet to investigate the mixing process. Instantaneous local equivalence ratios were obtained from the atomic emission intensity ratios of nitrogen at 501 nm and hydrogen at 656 nm. Using the developed SIBS sensor, the spatial distribution of a hydrogen jet in a direct-injection environment can be measured via spark-induced breakdown spectroscopy. The spatial structure of the hydrogen jet and its arrival time in the spark plug gap both affect the hydrogen/nitrogen mixing when the spark is discharged. The measurement results demonstrate the local variation in the equivalence ratio throughout the jet and along its axis.

5. Experimental study using SIBS with different ambient pressure at 0.5 MPa, 1.0 MPa and 1.5 MPa was conducted to investigate the influence of the ambient pressure. The spatial distribution of hydrogen jet in the different pressure of ambient pressure environment can be measured using the spark induced breakdown spectroscopy. The spectra results showed an increasing trend in background as well as intensity peak when

the ambient pressure increased. As the ambient pressure increased, the ambient nitrogen densities inside the chamber increased thus it influenced the spatial structure of the hydrogen jet and slowed down the spray penetration. This resulted the local variation of equivalence ratio throughout the jet and along its axis. Based on the study, the mixing process can be classified into three states, (i) initial unsteady state (HI at P_{amb}=1.0 and 1.5 MPa), (ii) quasi-steady state (HI at P_{amb}=0.5 MPa, CI and TI at P_{amb}= 0.5, 1.0, 1.5 MPa) and (iii) after-injection unsteady state (ATI in all conditions). From the results, the spatial structure of the hydrogen jet affects the hydrogen/nitrogen mixing and could be clarified with SIBS technique when the spark is discharged.

6. It can be concluded that SIBS technique could be a useful tool to determine the local equivalence ratio with a range of ambient conditions.

7 References

[1] Das L. Hydrogen engines: A View of the Past and a Look into the Future. International Journal of Hydrogen Energy 1990;15:425–43.

[2] Wang Z, Naterer GF. Integrated Fossil Fuel and Solar Thermal Systems for Hydrogen Production and CO2 Mitigation. International Journal of Hydrogen Energy 2014;39:14227–33.

[3] Boudries R. Hydrogen as a Fuel in The Transport Sector in Algeria. International Journal of Hydrogen Energy 2014;39:15215–23.

[4] Wallace J, Ward C. Hydrogen as a fuel. International Journal of Hydrogen Energy 1983;8:255–68.

[5] Karim G. Hydrogen as a Spark Ignition Engine Fuel. International Journal of Hydrogen Energy 2003;28:569–77.

[6] Verhelst S. Recent Progress in the Use of Hydrogen as a Fuel for Internal Combustion Engines. International Journal of Hydrogen Energy 2014;39:1071–85.

[7] Frolov SM, Medvedev SN, Basevich VY, Frolov FS. Self-Ignition of Hydrocarbon–Hydrogen–Air Mixtures. International Journal of Hydrogen Energy 2013;38:4177–84.

[8] White C, Steeper R, Lutz A. The Hydrogen-Fueled Internal Combustion Engine: a Technical Review. International Journal of Hydrogen Energy 2006;31:1292–305.

[9] Mohammadi A, Shioji M, Nakai Y, Ishikura W, Tabo E. Performance and Combustion Characteristics of a Direct Injection SI Hydrogen Engine. International Journal of Hydrogen Energy 2007;32:296–304.

[10] Das LM. Hydrogen-Oxygen Reaction Mechanism and its Implication to Hydrogen Engine Combustion. International Journal of Hydrogen Energy 1996;21:703–15.

[11] Duan J, Liu F, Sun B. Backfire Control and Power Enhancement of a Hydrogen Internal Combustion Engine. International Journal of Hydrogen Energy 2014;39:4581–9.

[12] Kim YY, Lee JT, Choi GH. An Investigation on the Causes of Cycle Variation in Direct Injection Hydrogen Fueled Engines. International Journal of Hydrogen Energy 2005;30:69–76.

[13] Wallner T, Scarcelli R, Nande AM, Naber JD. Assessment of Multiple Injection Strategies in a Direct-Injection Hydrogen Research Engine. SAE International Journal of Engines 2009;2:1701–9.

[14] Scarcelli R, Wallner T, Matthias N, Salazar V, Kaiser S. Numerical and Optical Evolution of Gaseous Jets in Direct Injection Hydrogen Engines. SAE Technical Paper 2011:SAE paper No. 2011–01 − 0675.

[15]   Koyanagi K, Hiruma M, Yamane K, Furuhama S. Effect of Hydrogen Jet on Mixture Formation in a High-Pressure Injection Hydrogen Fueled Engine with Spark Ignition. SAE Technical Paper 1993:SAE paper No. 931811.

[16]   Oikawa M, Ogasawara Y, Kondo Y, Sekine K, Naganuma K, Takagi Y, et al. Optimization of Hydrogen Jet Configuration by Single Hole Nozzle and High Speed Laser Shadowgraphy in High Pressure Direct Injection Hydrogen Engines. SAE Technical Paper 2011:SAE paper No. 2011–01 – 2002.

[17]   Roy MK, Kawahara N, Tomita E, Fujitani T. High-Pressure Hydrogen Jet and Combustion Characteristics in a Direct-Injection Hydrogen Engine. SAE International Journal of Fuels and Lubricants 2011;5:1414–25.

[18]   Hall MJ, Koenig M. A Fiber-Optic Probe to Measure Precombustion In-Cylinder Fuel-Air Ratio Fluctuations in Production Engines. 26th Symposium (International) on Combustion 1996;26:2613–8.

[19]   Tomita E, Kawahara N, Masahiro S, Sadami Y, Yashisuke H, Akihiro K, et al. An Optical Sensor Instrumented in Spark Plug for In-Situ Fuel Concentration Measurement in an Engine Cylinder by 3.39 μm Infrared Absorption Method. 11th International Symposium on Application of Laser Diagnostics to Fluid Mechanics 2002:1–12.

[20]   Kawahara N, Tomita E, Kadowaki T, Honda T, Katashiba H. In Situ Fuel Concentration Measurement Near a Spark Plug in a Spray-Guided Direct-Injection Spark-Ignition Engine Using Infrared Absorption Method. Experiments in Fluids 2010;49:925–36.

[21]   Tomita E, Hamamoto Y, Yoshiyama S, Toda H. Measurement of Fuel Concentration Distribution of Transient Hydrogen Jet and its Flame Using Planar Laser Induced Fluorescence Method. JSAE Review 1998;19:329–35.

[22]   Blotevogel T, Hartmann M, Rottengruber H, Leipertz A. Tracer-Based Laser-Induced Fluorescence Measurement Technique for Quantitative Fuel/Air-Ratio Measurements in a Hydrogen Internal Combustion Engine. Applied Optics 2008;47:6488–96.

[23]   Kaiser S, White CM. PIV and PLIF to Evaluate Mixture Formation in a Direct-Injection Hydrogen-Fuelled Engine. SAE International Journal of Engines 2009;1:657–68.

[24]   Miles PC, Hinze PC. Characterization of the Mixing of Fresh Charge with Combustion Residuals Using Laser Raman Scattering with Broadband Detection. SAE Technical Paper 1998:SAE paper No. 981428.

[25]   Egermann J, Koebcke W, Ipp W, Leipertz A. Investigation of the Mixture Formation Inside a Gasoline Direct Injection Engine by Means of Linear Raman Spectroscopy. Proceedings of the Combustion Institute 2000;28:1145–52.

[26]   Phuoc TX, White FP. Laser-Induced Spark for Measurements of the Fuel-to-Air Ratio of a Combustible Mixture. Fuel 2002;81:1761–5.

[27] Phuoc TX. Laser-Induced Spark for Simultaneous Ignition and Fuel-to-Air Ratio Measurements. Optics and Lasers in Engineering 2006;44:520–34.

[28] Shudo T, Oba S. Mixture Distribution Measurement Using Laser Induced Breakdown Spectroscopy in Hydrogen Direct Injection Stratified Charge. International Journal of Hydrogen Energy 2009;34:2488–93.

[29] Böker D, Brüggemann D. Advancing Lean Combustion of Hydrogen–Air Mixtures by Laser-Induced Spark Ignition. International Journal of Hydrogen Energy 2011;36:14759–67.

[30] Hunter AJR, Wainner RT, Piper LG, Davis SJ. Rapid Field Screening of Soils for Heavy Metals with Spark-Induced Breakdown Spectroscopy. Applied Optics 2003;42:2102–9.

[31] Hunter AJR, Morency JR, Senior CL, Davis SJ, Fraser ME. Continuous Emissions Monitoring Using Spark-Induced Breakdown Spectroscopy. Journal of the Air & Waste Management Association 2000;50:111–7.

[32] Srungaram PK, Ayyalasomayajula KK, Yu-Yueh F, Singh JP. Comparison of Laser Induced Breakdown Spectroscopy and Spark Induced Breakdown Spectroscopy for Determination of Mercury in Soils. Spectrochimica Acta Part B: Atomic Spectroscopy 2013;87:108–13.

[33] Fansler TD, Stojkovic B, Drake MC, Rosalik ME. Local Fuel Concentration Measurements in Internal Combustion Engines Using Spark-Emission Spectroscopy. Applied Physics B: Lasers and Optics 2002;75:577–90.

[34] Kawahara N, Tomita E, Takemoto S, Ikeda Y. Fuel Concentration Measurement of Premixed Mixture Using Spark-Induced Breakdown Spectroscopy. Spectrochimica Acta Part B: Atomic Spectroscopy 2009;64:1085–92.

[35] Roy MK, Kawahara N, Tomita E, Fujitani T. Jet-Guided Combustion Characteristics and Local Fuel Concentration Measurements in a hydrogen Direct-Injection Spark-Ignition Engine. Proceedings of the Combustion Institute 2013;34:2977–84.

[36] Abdul Rahman MT, Kawahara N, Tomita E. Mixing Process of Direct Injection Hydrogen Jet in a Constant Volume Vessel by Using Spark-Induced Breakdown Spectroscopy. SAE Technical Paper 2013:SAE paper No. 2013–01 – 2526.

[37] Abdul Rahman MT, Kawahara N, Tsuboi K, Tomita E. Visualization and Concentration Measurement of a Direct-Injection Hydrogen Jet in a Constant-Volume Vessel Using Spark-Induced Breakdown Spectroscopy. International Journal of Hydrogen Energy 2014;39:17896–905.

[38] Norbeck J, Heffel J, Durbin T. Hydrogen Fuel for Surface Transportation. Society of Automotive Engineers Inc; 1996.

[39] Tang X, Heffel J, Kabat K. Ford P2000 Hydrogen Engine Dynamometer Development. SAE Technical Paper 2002:SAE paper No. 2002–01 – 0242.

[40] Maccarley C, Vanvorst W. Electronic Fuel Injection Techniques for Hydrogen Powered I.C. Engines. International Journal of Hydrogen Energy 1980;5:179–203.

[41] Mathur H, Das L. Performance Characteristics of a Hydrogen Fuelled SI Engine Using Timed Manifold Injection. International Journal of Hydrogen Energy 1991;16:115–27.

[42] Deluchi M. Hydrogen Vehicles: an Evaluation of Fuel Storage, Performance, Safety, Environmental Impacts, and Cost. International Journal of Hydrogen Energy 1989;14:81–130.

[43] Furuhama S. Hydrogen Engine Systems for Land Vehicles. International Journal of Hydrogen Energy 1989;14:907–13.

[44] Chuang S-H, Hong Z-C, Wang J-H. The Application of Turbulent Kinetic Theory to a Reacting Flow of Turbulent Plane Jet. International Journal of Numerical Methods for Heat & Fluid Flow 1998;8:153–68.

[45] Kuo T, Bracco F. On the Scaling of Transient Laminar, Turbulent, and Spray Jets. SAE Technical Paper 1982:SAE paper No. 820038.

[46] Sukumaran S, Kong S-C. Numerical Study on Mixture Formation Characteristics in a Direct-Injection Hydrogen Engine. International Journal of Hydrogen Energy 2010;35:7991–8007.

[47] Abramovich G. The Theory of Turbulent Jets. The MIT Press; 1984.

[48] Ricou FP, Spalding DB. Measurements of Entrainment by Axisymmetrical Turbulent Jets. Journal of Fluid Mechanics 2006;11:21–32.

[49] Rajaratnam N. Turbulent jets. Journal of Fluid Mechanics 1976;82:605–8.

[50] Cumber P. Predictions of The Structure of Turbulent, Highly Underexpanded Jets. Journal of Fluids Engineering 1995;117:599–604.

[51] Hatanaka K, Saito T. Influence of Nozzle Geometry on Underexpanded Axisymmetric Free Jet Characteristics. Shock Waves 2012;22:427–34.

[52] Berckmuller M, Rottengneber H, Eder A. Potentials of a Charged SI-Hydrogen Engine. SAE Technical Paper 2003:SAE paper No. 2003–01 − 3210.

[53] Shioji M, Kitazaki M, Mohammadi A, Kawasaki K, Eguchi S. Knock Characteristics and Performance in an SI Engine with Hydrogen and Natural-Gas Blended Fuels. SAE Technical Paper 2004:SAE paper No. 2004–01 − 1929.

[54] Tang X, Kabat DM, Natkin RJ, Stockhausen WF, Co FM. Ford P2000 Hydrogen Engine Dynamometer Development Reprinted From∶ SI Combustion and Flow Diagnostics. SAE Technical Paper 2002:SAE paper No. 2002–01 − 0242.

[55]   Natkin RJ, Tang X, Boyer B, Oltmans B, Denlinger A, Heffel JW. Hydrogen IC Engine Boosting Performance and NOx Study Reprinted From : SI Combustion. SAE Technical Paper 2003:SAE paper No. 2003–01 – 0631.

[56]   Zervas E. Correlations Between Cycle-to-Cycle Variations and Combustion Parameters of a Spark Ignition Engine. Applied Thermal Engineering 2004;24:2073–81.

[57]   Fischer J, Velji A, Spicher U. Investigation of Cycle-to-Cycle Variations of In-Cylinder Processes in Gasoline Direct Injection Engines Operating With Variable Tumble Systems. SAE Technical Paper 2004:SAE paper No. 2004–01 – 0044.

[58]   Cheng TS, Wu CY, Chen CP, Li YH, Chao YC, Yuan T, et al. Detailed Measurement and Assessment of Laminar Hydrogen Jet Diffusion Flames. Combustion and Flame 2006;146:268–82.

[59]   Tsujimura T, Mikami S, Achiha N. A Study of Direct Injection Diesel Engine Fueled with Hydrogen. SAE Technical Paper 2003:SAE paper No. 2003–01 – 0761.

[60]   Houf WG, Evans GH, Schefer RW. Analysis of jet flames and unignited jets from unintended releases of hydrogen. International Journal of Hydrogen Energy 2009;34:5961–9.

[61]   Hourri a., Gomez F, Angers B, Bénard P. Computational Study of Horizontal Subsonic Free Jets of Hydrogen: Validation and Classical Similarity Analysis. International Journal of Hydrogen Energy 2011;36:15913–8.

[62]   Imamura T, Hamada S, Mogi T, Wada Y, Horiguchi S, Miyake A, et al. Experimental Investigation on the Thermal Properties of Hydrogen Jet Flame and Hot Currents in the Downstream Region. International Journal of Hydrogen Energy 2008;33:3426–35.

[63]   Grune J, Sempert K, Kuznetsov M, Breitung W. Experimental Study of Ignited Unsteady Hydrogen Jets into Air. International Journal of Hydrogen Energy 2011;36:2497–504.

[64]   Ruggles a. J, Ekoto IW. Ignitability and Mixing of Underexpanded Hydrogen Jets. International Journal of Hydrogen Energy 2012;37:17549–60.

[65]   Rottengruber H, Berckmüller M, Elsässer G, Brehm N, Schwarz C. Direct-Injection Hydrogen SI-Engine - Operation Strategy and Power Density Potentials. SAE Technical Paper 2004:SAE paper No. 2004–01 – 2927.

[66]   Zheng J, Bie H, Xu P, Liu P, Zhao Y, Chen H, et al. Numerical Simulation of High-Pressure Hydrogen Jet Flames During Bonfire Test. International Journal of Hydrogen Energy 2012;37:783–90.

[67]   Mohammadi A, Shioji M, Matsui Y, Kajiwara R. Spark-Ignition and Combustion Characteristics of High-Pressure Hydrogen and Natural-Gas Intermittent Jets. Journal of Engineering for Gas Turbines and Power 2008;130:062801.

[68] Sánchez–Sanz M, Rosales M, Sánchez AL. The Hydrogen Laminar Jet. International Journal of Hydrogen Energy 2010;35:3919–27.

[69] Péneau F, Pedro G, Oshkai P, Bénard P, Djilali N. Transient Supersonic Release of Hydrogen from a High Pressure Vessel: A Computational Analysis. International Journal of Hydrogen Energy 2009;34:5817–27.

[70] Veser a., Kuznetsov M, Fast G, Friedrich A, Kotchourko N, Stern G, et al. The Structure and Flame Propagation Regimes in Turbulent Hydrogen Jets. International Journal of Hydrogen Energy 2011;36:2351–9.

[71] Wallner T, Matthias NS, Scarcelli R. Influence of Iinjection Strategy in a High-Efficiency Hydrogen Direct Injection Engine. SAE International Journal of Fuels and Lubricants 2011;5:1–12.

[72] Scarcelli R, Wallner T, Matthias N, Salazar V, Kaiser S. Mixture Formation in Direct Injection Hydrogen Engines: CFD and Optical Analysis of Single- and Multi-Hole Nozzles. SAE International Journal of Engines 2011;4:2361–75.

[73] Stan C. Direct Injection Systems for Spark-Ignition and Compression-Ignition Engines. Society of Automotive Engineers Book; 1999.

[74] T. Kume, Y. Iwamoto, K. Iida, M. Murakami, K. Akishino HA. Combustion Control Technologies for Direct Injection SI Engine. SAE Technical Paper 1996:SAE paper No. 960600.

[75] Preussner C, Doring C, Fehler S, Kampmann S. GDI: Interaction Between Mixture Preparation, Combustion System and Injector Performance. SAE Technical Paper 1998:SAE paper No. 980498.

[76] Smith JD, Sick V. Quantitative, Dynamic Fuel Distribution Measurements in Combustion-Related Devices Using Laser-Induced Fluorescence Imaging of Biacetyl in Iso-Octane. Proceedings of the Combustion Institute 2007;31:747–55.

[77] J.B.Heywood. Internal Combustion Engine Fundamentals, McGraw-Hill Books, 1988.

[78] Yamin JAA, Gupta HN, Bansal BB, Srivastava ON. Effect of Combustion Duration on the Performance and Emission Characteristics of a Spark Ignition Engine Using Hydrogen as a Fuel. International Journal of Hydrogen Energy 2000;25:581–9.

[79] Kahraman E, Cihangir Ozcanlı S, Ozerdem B. An Experimental Study on Performance and Emission Characteristics of a Hydrogen Fuelled Spark Ignition Engine. International Journal of Hydrogen Energy 2007;32:2066–72.

[80] Sadiq Al-Baghdadi M a. R. Effect of Compression Ratio, Equivalence Ratio and Engine Speed on the Performance and Emission Characteristics of a Spark Ignition Engine Using Hydrogen as a Fuel. Renewable Energy 2004;29:2245–60.

[81]   Grunefeld G, Knapp M, Beushausen V. In-Cylinder Measurements and Analysis on Fundamental Cold Start and Warm-up Phenomena of SI Engines. SAE Technical Paper 1995:SAE paper No. 952394.

[82]   Rabenstein F, Egermann J. Vapor-Phase Structures of Diesel-Type Fuel Sprays: An Experimental Analysis. SAE Technical Paper 1998:SAE paper No. 982543.

[83]   Wickstrom N, Byttner S, Holmberg U. Robust Tuning of Individual Cylinders AFR in SI Engines with the Ion Current. SAE Technical Paper 2005:SAE paper No. 2005–01 – 0020.

[84]   Balles EN, Vandyne EA, Wahl AM. In-Cylinder Air/Fuel Ratio Approximation Using Spark Gap Ionization Sensing. SAE Technical Paper 1998:SAE paper No. 980166.

[85]   Panousakis D, Gazis A, Patterson J, Chen R. Analysis of SI Combustion Diagnostics Methods Using Ion-Current Sensing Techniques. SAE Technical Paper 2006:SAE paper No. 2006–01 – 1345.

[86]   Kawahara N, Tomita E, Hayashi K, Tabata M, Iwai K, Kagawa R. Cycle-Resolved Measurements of the Fuel Concentration Near a Spark Plug in a Rotary Engine Using an in Situ Laser Absorption Method. Proceedings of the Combustion Institute 2007;31:3033–40.

[87]   Nishiyama A, Kawahara N, Tomita E. In-Situ Fuel Concentration Measurement Near Spark Plug by 3.392 μm Infrared Absorption Method-Application to Spark Ignition Engine. SAE Technical Paper 2003:SAE paper No. 2003–01 – 1109.

[88]   Kawahara N, Tomita E, Hayashi K, Tabata M, Iwai K, Kagawa R. In-Situ Fuel Concentration Measurement Using an IR Spark Plug Sensor by Laser Infrared Absorption Method - Application to a Rotary Engine. 13th Int Symp on Applications of Laser Techniques to Fluid Mechanics 2006:1–11.

[89]   Tomita E, Kawahara N, Yoshiyama S, Kakuho A, Itoh T, Hamamoto Y. In Situ Fuel Concentration Measurement Near Spark Plug in Spark-Ignition Engines by 3.39 μm Infrared Laser Absorpsion Method. Proceeding of the Combustion Institute 2002;29:735–41.

[90]   Lee JG, Kim K, Santavicca DA. Measurement of Equivalence Ratio Fluctuation and its Effect on Heat Release During Unstable Combustion. Proceeding of the Combustion Institute 2000;28:415–21.

[91]   Nishiyama A, Kawahara N, Tomita E. In-Situ Fuel Concentration Measurement Near Spark Plug by 3.392 μm Infrared Absorption Method-Application to a Port Injected Lean-Burn Engine. SAE Technical Paper 2004:SAE paper No. 2004–01 – 1353.

[92]   S. Yoshiyama, Y. Hamamoto, E. Tomita KM. Measurement of Hydrocarbon Fuel Concentration by Means of Infrared Absorption Technique with 3.39 μm He-Ne Laser. JSAE Review 1996;17:339–45.

[93] Han D, Steeper RR. An LIF Equivalence Ratio Imaging Technique for Multicomponent Fuels in an IC Engine. Proceedings of the Combustion Institute 2002;29:727–34.

[94] Schulz C, Sick V. Tracer-LIF Diagnostics: Quantitative Measurement of Fuel Concentration, Temperature and Fuel/Air Ratio in Practical Combustion Systems. Progress in Energy and Combustion Science 2005;31:75–121.

[95] Liebeskind JG, Hanson RK, Cappelli M a. Laser-Induced Fluorescence Diagnostic for Temperature and Velocity Measurements in a Hydrogen Arcjet Plume. Applied Optics 1993;32:6117–27.

[96] Cruyningen I Van, Lozano A, Hanson RK. Quantitative Imaging of Concentration by Planar Laser-Induced Fluorescence. Experiments in Fluids 1990;10:41–9.

[97] Kaiser S a., Long MB. Quantitative Planar Laser-Induced Fluorescence of Naphthalenes as Fuel Tracers. Proceedings of the Combustion Institute 2005;30:1555–63.

[98] Engel SR, Koch P, Braeuer A, Leipertz A. Simultaneous Laser-Induced Fluorescence and Raman Imaging Inside a Hydrogen Engine. Applied Optics 2009;48:6643–50.

[99] Salazar V, Kaiser S, Halter F. Optimizing Precision and Accuracy of Quantitative PLIF of Acetone as a Tracer for Hydrogen Fuel. SAE International Journal of Fuels and Lubricants 2009;2:737–61.

[100] Radziemski L. From LASER to LIBS, the Path of Technology Development. Spectrochimica Acta Part B: Atomic Spectroscopy 2002;57:1109–13.

[101] Letty C, Pastore A, Mastorakos E, Balachandran R, Couris S. Comparison of Electrical and Laser Spark Emission Spectroscopy for Fuel Concentration Measurements. Experimental Thermal and Fluid Science 2010;34:338–45.

[102] Yaroshchyk P, Morrison RJS, Body D, Chadwick BL. Quantitative Determination of Wear Metals in Engine Oils Using Laser-Induced Breakdown Spectroscopy: A Comparison Between Liquid Jets and Static Liquids. Spectrochimica Acta Part B: Atomic Spectroscopy 2005;60:986–92.

[103] Ferioli F, Buckley S. Measurements of Hydrocarbons Using Laser-Induced Breakdown Spectroscopy. Combustion and Flame 2006;144:435–47.

[104] Stavropoulos P, Michalakou A, Skevis G, Couris S. Quantitative Local Equivalence Ratio Determination in Laminar Premixed Methane–Air Flames by Laser Induced Breakdown Spectroscopy (LIBS). Chemical Physics Letters 2005;404:309–14.

[105] Sturm V, Noll R. Laser-Induced Breakdown Spectroscopy of Gas Mixtures of Air, CO2, N2, and C3H8 for Simultaneous C, H, O, and N Measurement. Applied Optics 2003;42:6221–5.

[106] Ferioli F, Puzinauskas P V, Buckley SG. Laser-Induced Breakdown Spectroscopy for On-Line Engine Equivalence Ratio Measurements. Applied Spectroscopy 2003;57:1183–9.

[107] Lackner M, Winter F. Laser Ignition in Internal Combustion Engines - A Contribution to a Sustainable Environment. 14th IFRF Members Conference 2004:1–18.

[108] Mansour MS, Imam H, Elsayed K a., Abbass W. Local Equivalence Ratio Measurements in Turbulent Partially Premixed Flames Using Laser-Induced Breakdown Spectroscopy. Spectrochimica Acta Part B: Atomic Spectroscopy 2009;64:1079–84.

[109] Kawahara N, Beduneau JL, Nakayama T, Tomita E, Ikeda Y. Spatially, Temporally, and Spectrally Resolved Measurement of Laser-Induced Plasma in Air. Applied Physics B 2006;86:605–14.

[110] Windom BC, Diwakar PK, Hahn DW. Dual-pulse Laser Induced Breakdown Spectroscopy for analysis of gaseous and aerosol systems: Plasma-analyte interactions. Spectrochimica Acta Part B: Atomic Spectroscopy 2006;61:788–96.

[111] Merer RM, Wallace JS. Spark Spectroscopy for Spark Ignition Engine Diagnostics. SAE Technical Paper 1995:SAE paper No. 950164.

[112] Kaiser EW, Lorusso J a., Lavoie G a., Adamczyk a. a. The Effect of Oil Layers on the Hydrocarbon Emissions from Spark-Ignited Engines. Combustion Science and Technology 1982;28:69–73.

[113] Naidis G V. Simulation of Streamer-to-Spark Transition in Short Non-Uniform Air Gaps. Journal of Physics D: Applied Physics 1999;32:2649–54.

[114] Maly R. Fuel Economy. Boston, MA: Springer US; 1984.

[115] Panofsky H, Brier G. Some Applications of Statistics to Meteorology. Mineral Industries Extension Services, College of Mineral Industries, Pennsylvania State University; 1958.

[116] Karl J. An Introduction to Digital Signal Processing. San Diego, California: Academic Press; 1989.

[117] Shirley D. High-Resolution X-Ray Photoemission Spectrum of the Valence Bands of Gold. Physical Review 1972;5:4709–14.

[118] Proctor A, Sherwood PMA. Data Analysis Techniques in X-Ray Photoelectron Spectroscopy. Analytical Chemistry 1982;54:13–9.

[119] Tanabe H, Suzuki N, Sorihashi T, Fujimoto H, Sato G. Experimental Study on Transient Gas Jet. Proc XIX FISITA 1982:No. 82026.